# 博士論文

論文題目　THz Vector Beams : Generation and Applications

(テラヘルツベクトルビームの発生と応用)

氏名　郑 渚

*This thesis is dedicated to my parents for their endless love, support, and encouragement.*

# Abstract

It has been proved in recent years, besides phase and amplitude features, polarization offers another dimension to manipulate electromagnetic field. Because of the great application potential in imaging, information processing, bio-sensing, security, and etc., on the topic of light modulation, polarization features attract a growing attention. Particularly, a new class of inhomogeneously polarized optical beams, so-called "vector beams", were theoretically proposed and experimentally realized, and proved to be pivotal in many applications.

Vector beams exhibit affluent characteristics, these features are tightly related to a variety of fundamental physical phenomena, including sharp focusing, strong longitudinal electric and magnetic field in the foci, new class of optical angular momentum, and etc.. These specialties will deepen the understanding of light, and pave a new way on controlling light.

Although vector beams are important, in so-called "terahertz (THz) gap", the researches related to vector beams are very limited. Transplanting the concept of "vector beams" to "THz gap" is beneficial for exploring the new potential applications of THz waves.

For the THz wave applications, we need to treat relatively broad bandwidth, thus the generation of THz vector beams is till now a challenging topic. The present methods to generate THz vector beams suffer from complicated structures, narrow bandwidth, mode imperfections, and difficult to switch between two fundamental modes of vector beams-radially, and azimuthally polarized beams.

The first aim of present thesis is to develop a convenient and stable method to generate broadband and high-quality THz vector beams. To achieve this goal, three-fold rotational symmetrical optical nonlinear crystals are

selected to be the THz emission medium. By designing and making a segmented half wave-plate mode converter, or an axis-spatial-variant segmented nonlinear crystal, THz radially and azimuthally polarized beams are realized experimentally. In this method, the related optical elements are simple and stable. Moreover, by only rotating one element in the setup, both radially and azimuthally polarized THz beams can be obtained. Due to the THz emission is from nonlinear crystals, the spectrum of generated THz vector beams is much larger than the reported results based on photoconductive antennas, or narrow bandwidth elements.

To evaluate the generated THz vector beams, three experimental setups were employed. At first, intensity distributions of the THz vector beams were recorded with THz cameras, donut intensity profiles of THz vector beams were observed, and with inserting and rotating a wire grid polarizer (WGP), two lobes related to the orientation of the WGP were confirmed. These features testify the THz vector modes are successfully generated. Sequently, 2D photoconductive (PC) antenna and free space electro-optics (EO) THz time domain spectroscopy (TDS) systems were built to register full information of the THz vector beams, including amplitude, phase and polarization features. The longitudinal electric or magnetic field in the focal volume of the THz vector beams were also experimentally proved. From the results, main characteristics of THz vector beams are clearly confirmed.

Furthermore, the THz radial beams were introduced to efficiently couple to bare metal wires to realize sufficient THz wave-guiding. In comparison with reported results, the spectrum of guided THz wave in our experiments is as large as 1.5 THz, this number is about 3 times broader; the dispersion and attenuation coefficient are proved to maintain a very low level in this much larger spectrum. Moreover, the energy coupling efficiency is experimentally evaluated for the first time. At 0.3 THz, the efficiency is as large as 66%, which is about two orders improved in comparison with the reported scattering in-couple method.

Based on these results, prospective applications of THz vector beams are discussed.

# Acknowledgements

Working on my PhD. course in Gonokami Group in the University of Tokyo has been a wonderful and unforgettable experience in my life.It is not only about studying on my research topic but also about living in a foreign country, working in a group including members from various backgrounds. To take this opportunity, I am indebted to many people for making the time in Tokyo a memorable and precious experience.

At the top of the list, I would like to express my deepest gratitude to my advisor, Prof. Makoto Kuwata-Gonokami. Studying under the guidance of Prof. Gonokami has been a real pleasure to me, with fun and excitement, his outstandingly broad viewpoint, his professional ability, his high scientific standards have left me with an indelible impression, his advices led me to present many of the ideas proposed in this thesis, and under the high-skillful management of Prof. Gonokami, the Gonokami Group have been keeping a academically, physically and financially enriched and comfortable research environment. The gentlemanly manner and academic style of Prof. Gonokami are always the goals in my life.

I greatly appreciate Dr. Kuniaki Konishi, an Assistant Professor in the Photon Science Center, in the past three years, Dr. Konishi taught me from the usage of the equipments, to valuable experience in research, his advices covered all aspects in my research life, from daily discussions to paper peer review, from basic experimental skill sharing to experimental materials preparation. Without the help of Dr. Konishi, I can not finish my work smoothly. Dr. Konishi's altruistic help will continually affect me on my research road. I would like to express thanks to Dr. Kosuke Yoshioka, the Assistant Professor of the lab, his hard working and high-level experimental

abilities impress me a lot, also his teaching about fiber in-coupling and dispersion compensation solved my problems in the experiments.

Specially, I express my sincere thanks to Dr. Natsuki Kanda, he is my collaborator and an upperclassmen who helped me a lot in the experiments, his insightful suggestions and fruitful discussions boosted my research, and he also maintains several key instruments in my experiments, his kindly help ensure the timely completion of my experiments. I am thankful to the members in Gonokami Group, Dr. Jia Li, Dr. Junko Omachi, Dr. Daisuke Hirano, Dr. Takuya Higuchi, Mr. Naotomo Takemura, Mr. Yuki Nagakubo, Mr. Kohei Togashi, Mr. Ryo Imai, Mr. Kenta Fukuoka, Mr. Natsuki Nemoto, Mr. Yusuke Morita, we share information and experience with each others. Especially Dr. Jia Li, Dr. Takuya Higuchi, Mr. Ryo Imai and Mr. Natsuki Nemoto, I learnt a lot when working together with them, I enjoy the time in Tokyo with all of them, and hope them all be successful in their lives.

I would thank stuffs in the Photon Science Center, lecturer Dr. Hiroharu Tamaru, Dr. Masahiro Daimon, they helps a lot in discussions and daily driving of the lab. I am grateful to many people out the lab, for example, a guest professor, Prof. Stepan Lucyszyn, his critical comments opened new angles and helped me a lot. Comments from Prof. Masato Koashi, Dr. Munekazu Horikoshi had helped me to polish my research.

Secretariats in Gonokami Lab, Ms. Akane Oshima , Ms. Masako Shirahama, and Ms. Kimiko Kitakoji supported me a lot on submitting of documents, claiming of travel fee, and registering of conferences. Thank them very much for their kindly help in these years.

I acknowledge critical comments based on the vast backgrounds of the examining committee, Prof. Tsutomu Shimura, Prof. Shin Inouye, Prof. Yohei Kobayashi, and Prof. Ryo Shimano.

Last, but not least, I would like to express my sincere gratitude to my family and friends for their kindness and courtesy. Especially, I want to give my deepest gratitude and love to my parents, they encourage me and support me to go forward.

# Contents

# Glossary

**m-, $\mu$-, n-, p-, f-** mili-, micro-, nano-, pico- ,femto-

**k-, M-, G-, T-** kilo-, Mega-, Giga-, Tera-

**THz** Terahertz

**NIR** Near-Infrared

**THz-TDS** Terahertz Time Domain Spectroscopy

**PC antenna** Photoconductive Antenna

**EO sampling** Electro-optic Sampling

**SoP** States of Polarization

**CV beams** Cylinderical Vector Beams

**HWP,QWP** Half Wave-Plate, Quarter Wave-Plate

**LT-GaAs** Low-temperature Grown Gallium Arsenide

**FWHM** Full Width at Half Maximum

**SHG** Second Harmonic Generation

**CW lasers** Continuous Wave Lasers

**DPSS** Diode-Pumped Solid State

**OPA** Optical Parameter Amplification

**GVD** Group Velocity Dispersion

**SN ratio** Signal-Noise Ratio

**FFT** Fast Fourier Transform

**NA** Numerical Aperture

**SLM** Spatial Light Modulator

**PTFE** Polytetrafluoroethylene

**WGP** Wire Grid Polarizer

Chapter 1

# Introduction

As one of the most fundamental information carriers, photon plays a pivotal role in not only scientific and technological researches, but also security, industrial and medical applications. The discoveries of new phenomena, novel effects and potential applications in optics have imposed great impacts on science and technology. To fully exert the advantages of photons as information carriers, the key is to manipulate optical field. In classical electromagnetic theory, the parameters which can sufficiently describe optical field include amplitude, phase and polarization, but in traditional optical technologies, manipulation of electromagnetic field involves only phase and amplitude features, the modulation of phase and amplitude has been efficiently explored and widely utilized in information processing, the achievements have greatly pushed the development of science and technology.

The concept of "vector beams" has attracted increasing interest in recent years. The key of this concept is spatially manipulating polarization features of optical beams. Vector beams reveal a new dimension to control light, by introducing these inhomogeneously polarized beams, the understanding of spatial-temporal nature of light is deepened, new phenomena involving interactions between light and matter are discussed, and novel effects are discovered, e.g. the sharper focal spot of radially polarized beams and the strong longitudinally polarized electric field in the foci [1], an additional freedom in photon entanglement [2, 3], and etc.. These special effects make vector beams to be a good candidate in many applications including bio-photonics, quantum information, near field optics, optical manipulation, single molecule imaging, super-resolution microscopy, laser acceleration and micro fabrication, and etc..[4]

Terahertz (THz) wave is electromagnetic wave whose frequency lies between the microwave and infrared ranges of the spectrum. Albeit the space of our everyday life is crowed by naturally occurring THz radiation, this band remains the least explored part in the electromagnetic spectrum , because the generation and detection of electromagnetic fields in this spectral range is difficult. Neither optical nor microwave technologies can not be directly transplanted to the THz range. The lack of according technologies induced the THz band always being called the "THz gap". With the increasing research interest in the THz gap, this gap has been rapidly vanishing in the last 20 years, optical technologies have made immense advances from the high frequency side, while microwave technologies go up from the low frequency side. The development of ultra-fast optical techniques, the manufacturing of semiconductors with very short lifetimes and of band-engineered hetero-structures, as well as the micro-machining techniques and nanotechnologies have pushed the THz fields to be a new area of quantum electronic researches with many important applications. [5]

In this chapter, a brief introduction to THz radiation and vector beams will be given to establish a basic background of this thesis. Moreover, the panorama of the whole thesis will be shown, the structure of subsequent chapters will be built hereon.

## 1.1 Terahertz Band

"Terahertz (THz) band" is a generic term for the frequency band from 0.1-10 THz, similiar to microwaves, infrared radiation, and x-rays. The typical units for 1 THz is:

Frequency: $\nu = 1$ THz = 1000 GHz

Period: $\tau = 1/\nu = 1$ ps

Wavelength: $\lambda = c/\nu = 0.3$ mm = 300 $\mu$m ($c$ is the speed of light in vacuum)

Wavenumber: $\bar{k} = k/2\pi = 1/\lambda = 33.3$ cm$^{-1}$

Photon energy: $h\nu = 4.14$ meV

The THz region is crowded with innumerable spectral features associated with fundamental physical processes such as rotational transitions of molecules, large-amplitude vibrational motions of organic compounds, lattice vibrations in solids, intraband transitions in semiconductors, and energy gaps in superconductors. The interest in the THz frequency range is boosted by the fact that this frequency band is the spectrum where unique physical phenomena with characteristic features are produced. THz applications exploit these unique features of material responses to THz wave. [5–8]

The unique features of THz frequency covers multidisciplinary regions and its potential lays in a very broad area. For example, the spectral energy distribution in observable galaxies shows that 50% of the total luminosity and 98% of photons emitted since Big-Bang are located in the THz frequency range [9]. Moreover, THz fields strongly interact with polar substances but penetrate those non-polar, thus, the absorption spectra of many polar molecules lays in the THz band, this unique feature of such molecules is important in the surrounding medium monitoring, air pollution detecting, and gas sensing. Another feature of the THz band is, biological tissues or other biological constituents have distinct signatures in the THz range, for example, DNA signature, DNA manipulation, gene diagnostics were demonstrated experimentally using THz techniques [10]. Because in THz-TDS measurements, amplitude and phase information can be obtained simultaneously, while the THz range is strongly related to fundamental biological phenomena such as rotational transitions of molecules, large-amplitude vibrational motions of organic compounds. Moreover, the THz radiation is almost harmless to living cells or organic, so the THz spectroscopy will show a variety of bio-features without killing the living samples.

In communication and information processing systems, it is natural, and had been reported that THz signals are the information carriers in the 1-10 Tb/s optical communications systems, which will have great application potential in the future [11, 12]. Because of the relative wavelength of the THz band is smaller than the microwave spectrum, very small antenna arrays can be used in the THz range, these micro arrays can be used to develop imaging devices such as THz cameras [13, 14]. Moreover, although the size of THz devices are small, they can send or receive a huge quantity of information. It has been proved, THz modulators are able to modulate ultra-fast laser diodes with a cutoff frequency beyond 10 THz, and the 1 ps switching performance of the THz transistor is studied now by leading companies using the latest discoveries in nanotechnology [15].

Before the invention of THz time domain spectroscopy (TDS) systems, because of the THz band lays in the gap between the radio and optical frequency, it is difficult to generate and detect THz radiation coherently with sophistically developed radio technologies and optical methods, then the researches on THz band and its applications had been in a tardy progress. In 1984, D.H.Auston and his collaborates firstly proved a THz-TDS setup, this achievement opens a new door to THz researches [16]. In their original experiment, photoconductive (PC) antennas illuminated by picosecond (ps) optical pulses served as the THz (100 GHz) emitter and detector, and a THz pulse in the scale of several picosecond was successfully recorded with the TDS setup. Later, they also succeeded to generate THz pulses with optical rectification effects in electro-optic (EO) crystals. [17]

The main advantage of THz-TDS systems is that, in the measurements, both amplitude and phase information can be recorded at the same time, this character is pivotal for determining complex permittivity of materials in THz band. Thus, in THz experiments, THz-TDS systems are keeping a vital place.

In THz-TDS systems, the generation and detection of THz pulses are reciprocal in principle, it means the detection parts act as the counterparts of the generation setups.

One way to generate THz pulses is to employ nonlinear materials in which incident laser pulses undergo seconde order nonlinear frequency down conversion. Optical rectification and difference frequency generation are the physical processes to generate THz photons. Femtosecond laser pulses with a broad spectrum passing through these

nonlinear materials induce broadband THz pulse emission, the shape of these THz pulses resembles the optical pulse envelope, via optical rectification.

At the same time, the free-space electro-optic (EO) sampling records the electric field of broadband THz pulses in the time domain by making use of the Pockels effect, which is principally reverse to optical rectification. In the Pockels effect, the birefringence induced by THz electric field, in a nonlinear detection crystal, is proportional to the electric field amplitude. Utilizing a relative setup to vary the time delay between the THz and optical pulses, the time domain waveform can be mapped out by a weak optical probe measuring the THz field induced birefringence.

Another popular method is, it is well know, accelerating charges radiate electromagnetic waves, so from a biased photoconductive antenna excited by fs laser pulses, THz wave can be emitted. A PC antenna typically consists of two metal electrodes deposited on a semiconductor substrate. An fs optical beam, illuminates the gap between the electrodes and inspires photo-carriers, simultaneously a static bias field applied between the gap accelerates these free carriers. This photocurrent varies in time corresponding to the incident laser beam intensity. Consequently, fs laser pulses produce broadband THz pulses.

Referring the same principle PC antennas can also serve as THz detectors, in the absence of a bias electric voltage, a THz field accelerates photocarriers injected by fs laser pulses, to generate a current in the photoconductive gap. The induced photocurrent is proportional to the THz electric field amplitude. The THz waveforms can be registered in the time domain by measuring the photocurrent while controlling a time delay between the THz pulse and the optical pulses.

The details of principles and experimental setups for THz generation and detection will be discussed in Chapter 2 and Chapter 3.

## 1.2 Vector Beams

Polarization is among the most important properties of light, it represents the vector nature of light. When light interacts with matter, polarization features make many optical devices and systems to be possible. Before the 2000s, most optical researches only dealt with spatially homogeneous states of polarization (SoPs), i.e. linear, elliptical, and circular polarizations. In such cases, SoP does not depend on the spatial location in the beam cross section. In the past decade, there has been a rise of research interest on light beams which have spatial-variant SoPs. Spatial manipulation the SoPs of light beams offers another dimension in light modulation, and is proved to lead to new effects and phenomena that can expand the functionality and enhance the capability of optical systems. The light beams with inhomogeneous SoP in their cross sections are termed as "Vector Beams". One particular example is optical beams with cylindrical polarization symmetry, the so-called cylindrical vector (CV) beams. [4]

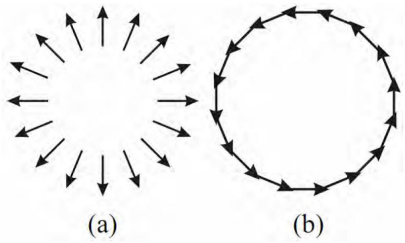


**Figure 1.1: The SoP distributions of radially and azimuthally polarized beams** - Black arrows indicate the local polarization. (a)Radially polarized beams, (b)Azimuthally polarized beams

The simplest and most typical CV beams are radially polarized beams and azimuthally polarized beams, of which in the beam front, the SoPs are along radial and azimuthal orientations, respectively, as shown in Fig.1.1. The spatial SoPs of radially and azimuthally polarized beams are orthogonal to each other, and can be identified by a polarizer, as shown in Fig.1.2.

Actually, as Fig.1.3 shown, the SoPs of radially and azimuthally polarized beams coincide with $TE_{01}$ and $TM_{01}$ modes in cylindrical coordinate [18]. In 1961, E.Snitzer theoretically described these electromagnetical modes [19], and after the invention of lasers, in 1972, two groups experimentally realized $TE_{01}$ and $TM_{01}$ modes [18, 20]. Among them, the group leaded by P. Dieter designed a mode selector in the laser

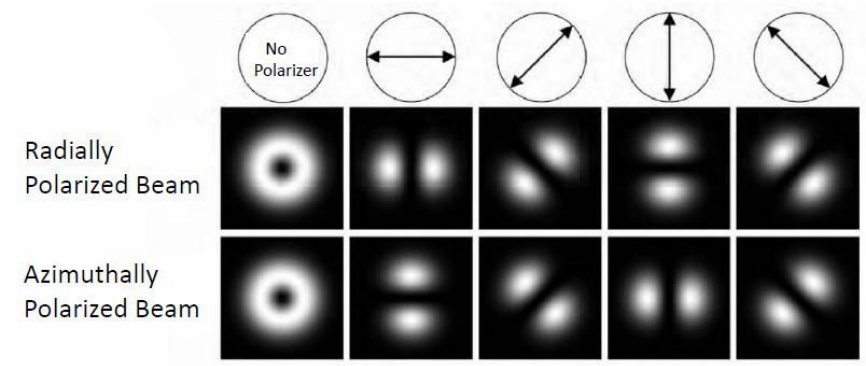


**Figure 1.2: The intensity distributions of radially and azimuthally polarized beams** - Black arrows indicate the orientations of polarizers.

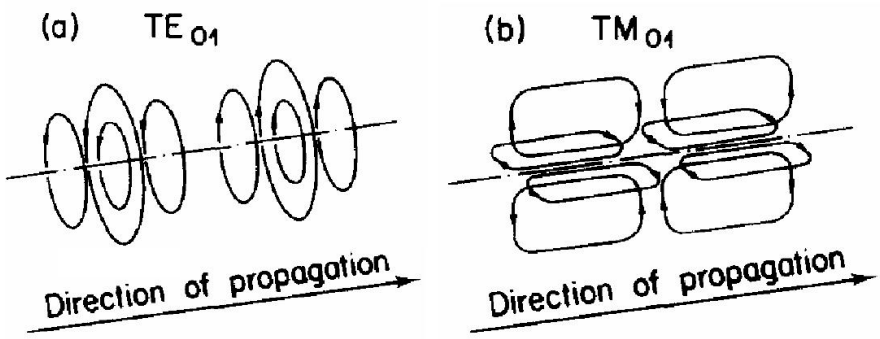


**Figure 1.3: Illustration of electric field vectors in $TE_{01}$ and $TM_{01}$ modes** - (a)$TE_{01}$,(b)$TM_{01}$, recopied from [18].

cavity, and generated azimuthally polarized modes ($TE_{01}$ modes), also in the paper, the authors mentioned when azimuthally polarized modes passing through a predesigned optical rotator, radial mods ($TM_{01}$ modes) would be realized [18]. In the same year, the group leaded by Y. Mushiake designed a special optical oscillator in the laser cavity, to force the output of the laser to be radially polarized modes [20]. After these preceding works, until 2000, in near 30 years, because the lack of applications, the researches of vector beams had almost stagnated. In this period, only limited literatures can be found on vector beams, several groups generated vector beams experimentally [21–25], and in theory, the group leaded by D.G.Hall in the university of Rochester did a series of works on vector beams, for example, deducing the azimuthal Bessel-Guass beam solution from the free-space azimuthal paraxial wave equation [26], finding the vector-beam solutions of the Maxwell's equations [27], investigating the diffraction characters of vector Bessel-Gauss beams [28] and the phenomena of focal shift in vector beams [29].

In 2000, a paper on vector beams published by T. Brown group in the university of Brown drew numerous attentions [30], in the paper, the authors theoretically analyzed the tight focal characters of radially and azimuthally polarized beams. They found for radially polarized beams, a strong longitudinal electric field presents in their focal spot; while in the case of azimuthally polarized beams, a pure longitudinal magmatic field will be realized in the focal volume. These characters shed new light on vector beams. Also in the same paper, a mathematical method proposed by B.Richrds and E.Wolf, named Richard-Wolf vector diffraction theory was set to be the standard numerical method to analyze the focal field of vector beams [31]. In 2003, R.Dorn and his collaborates experimentally realized a focal spot in size of $0.16\lambda^2$ for radially polarized beams, which is much smaller than $0.26\lambda^2$ for linearly polarized beams [1], the important point of this work is that, by introducing vector beams, breaking the diffraction limit is possible. Based on this paper, a explosive research enthusiasm on vector beams had been starting, a number of papers about focal engineering with vector beams [32–34], and applications of vector beams in microprocessing, laser accelerating, single molecule imaging, near field optics, nonlinear optics, optical manipulation and quantum information [35–40] are published.

More information, from theories to experiments about vector beams in the optical frequency region will be found in Chapter 4.

## 1.3 Vector Beams in the Terahertz Range

Although literatures on vector beams in the optical spectrum are now relatively affluent, ineluctable conundrum presents when transplanting this concept into the THz range. In optical range, the generation of vector beams mainly relies on mode selection, phase modulation and direct SoP modulation, because the optical elements of mode selecting, phase modulating and SoP modulating are sufficiently developed. Nevertheless, the very wide bandwidth of the THz range (typically 0.1-10 THz) induces it difficult to make such elements to cover the whole THz band, so it is hard to select vector modes or to convert linearly polarized beams into vector beams. For example, there is no good candidate of wave-plates (WPs) to cover the broad THz range, while in the case of optical range, segmented HWPs are frequently used to transfer linearly polarized beams to vector beams. Until now, the generation of the broadband THz vector beams is still an open and challenging topic. There are several papers discussing about the generation of THz vector beams, PC antennas [41–44], mode selectors [45], laser filaments in air [46–48], velocity-mismatched optical rectification [49], grooves on metal wires [50] are reported to generate THz vector modes experimentally. However, these methods suffer from obvious drawbacks and require several improvements. In the case of conventional photo-conductive antennas, the spectrum of THz radiation is limited in low THz frequency range, and it is difficult to increase the radiation intensity. With laser filaments, the generated THz radial modes were proved to be not ideal, local ellipticity had been observed [47, 48]; and in this method, a powerful laser is required. Furthermore, a common problem of the reported THz vector beam generation methods is the inflexibility, e.g. for PC antennas, an antenna with radial symmetry can only be used to generate radially polarized beams; if azimuthally polarized beams are needed, another antenna with azimuthal symmetry has to be fabricated. It is difficult to switch between radially and azimuthally polarized THz vector modes in present methods.

For the convenience of THz applications, it should be critical to introduce vector beams into the THz spectral range. One example is THz wave-guiding, in 2004, the group leaded by D.M.Mittleman reported bare metal wires, which support a plasmonic mode (known as Sommerfeld wave) on their surfaces in the THz range, are one of the best candidates for guiding THz waves because of their very low losses, negligible

dispersion, and structural simplicity [51]. The guiding modes on bare metal wires are radially polarized modes, so radially polarized THz beams can be introduced to efficiently couple to bare metal wire waveguides. Also azimuthally polarized modes are proved to be important in bore core THz waveguides [52].

In the THz range, bio-imaging is one of the most important applications, the sharper focal spot of radially polarized beams is potential to increase the resolution of THz imaging. Moreover, the longitudinal electric/magnetic field existing in the focal volume of radially/azimuthally polarized beams are believed to be promising in THz applications.

In Chapter 5, the present researches on THz vector beams will be introduced, and the generation of THz vector beams will be discussed. Also in Chapter 5, we will demonstrate a new method of THz vector beam generation, and the 2D polarization features of THz vector beams will be characterized [1], the experimental results are correspondent with theoretical predictions.

In Chapter 6, the generated THz radial beams are introduced to efficiently couple onto bare copper wires, to achieve low-attenuation and low-dispersion THz waveguiding in a broad spectral range. The energy coupling efficiency is experimentally determined for the first time, the number is as large as 66%, that proves the efficient coupling of propagating THz radial beams to metal wires is achieved.

At last, in Chapter 7, the summarization of this thesis, and future prospects will be given. Based on the efficient coupling and waveguiding scheme, a near-field probe is proposed to achieve sub-wavelength THz imaging. More works on THz vector beams are expected.

[1] In Chapter 5, for the completeness of the storyline, the author of this thesis includes the results from ref.[53], of which the author of this thesis is also a co-author, but the work is mainly leaded by Mr. Ryo Imai. For this part of content, including the THz vector beam generation with the segmented GaP(111), and the characterization of $E_z$, the priority belongs to Mr. Ryo Imai.

Chapter 2

# Generation and Detection of Terahertz Pulses

In the present chapter, the underlying physical principles of THz pulse generation and detection will be discussed. Basically, the typical waveform of broadband THz emission is a single-cycle pulse, which is an ultimate transform-limited waveform. The THz pulses are in the time scale of several picoseconds (ps), and generated by employing nonlinear optical responses of bound electrons (optical rectification) in nonlinear crystals, or transient photocurrents in semiconductor substrates, all these two effects are induced by ultrashort optical pulses from femtosecond (fs) lasers. The electron response time in these effects is not exactly transient, yet fast enough to induce sub-ps polarizations or photocurrents.

## 2.1 Generation and Detection of Terahertz Pulses Based on Photoconductive Antennas

The success story of photoconductive THz antennas comes with the invention of fs Ti:sapphire laser systems. Photoconductive antennas made for free space THz emission are based on ultrafast photoconductive (PC) switches, also named as Auston switches [54]. The first photoconductive antenna was excited with a pulsed dye laser [16]. However, from the early 1990s, since mode-locked Ti:sapphire lasers were applied for excitation, the PC antennas became widely used. The most popular systems for pulsed THz generation and detection today always use GaAs-based photoconductive antennas excited with mode-locked Ti:sapphire lasers.

The invention of PC THz antennas is an notable landmark in THz spectroscopy technique. This invention is not a semantic improvement, rather it opens up new

experimental possibilities in the THz spectrum. PC antennas excited with near-infrared (NIR) fs laser pulses can emit single-cycle THz pulses, such pulses can be used in the THz time-domain measurements. Commonly, a PC antenna is an electrical switch inspired by laser, in structure typically it is electrodes deposited on a PC semiconductor substrate, the semi-isolating substrate is isolator without laser excitation, and when the substrate is shot by fs laser pulses, a sudden increase in the number of free carriers (electrons and holes) generated by photons lead to the transient photoconductivity increasing, then the substrate becomes conductor in a short period. To achieve such switch processes, the photon energy of the laser excitation must be sufficiently larger than the bandgap energy of the material. Figure 2.1 briefly introduces a PC switch, in which a DC bias voltage and a load resistor are connected with the semiconducting material. When laser excites free electrons and holes in the substrate, the photocurrent flows through the circuit [5].

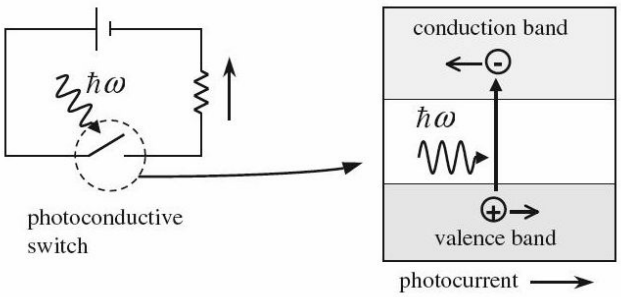


**Figure 2.1: Illustration of PC Switch** - Photons are gating PC switch [5].

In order to either generate or detect THz wave, both switching-on and switching-off action in the PC antenna should occur in the sub-ps time scale. The switch-on time directly depends on the laser pulse duration, and the switch-off time is mainly determined by the photo-carrier lifetime in the semiconductor substrate of the antenna. Thus, not only a short laser pulse duration, but also a short carrier lifetime is a key feature for ultrafast photoconductive switching. For high qualified photoconductive materials, high carrier mobility and high breakdown voltage are also vital, to ensure the PC antenna can bear more photon carriers. Several photoconductive materials have been tested for PC switches: chromium-doped gallium arsenide (Cr-GaAs),

low-temperature grown gallium arsenide (LT-GaAs), radiation-damaged silicon-on-sapphire (RD-SOS), indium phosphide (InP), and amorphous silicon [55–58].

In this work, LT-GaAs based antennas are used in THz experiments. The carrier lifetime of LT-GaAs substrate is in the sub-ps range: the LT-GaAs samples grown between 180 and 240 °C have sub-ps carrier lifetimes. The shortest lifetime that ~ 0.2 ps is obtained when the growth temperatures are near 200 °C [59]. The effective carrier mobilities of LT-GaAs are reported to be 200-400 $cm^2/V{\cdot}s$ [55]. Because the hole mobility in LT-GaAs is one order of magnitude lower than the electron mobility, carrier transport in the THz frequency range is dominated by electrons.

### 2.1.1 Generation of Terahertz Pulses from Photoconductive Antennas

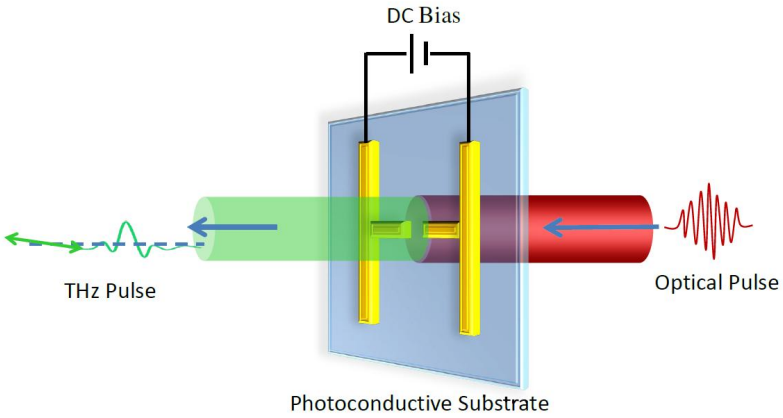


**Figure 2.2: Schematic diagram of THz pulse emission from a PC antenna** - The impulse current arising from the acceleration and decay of photon carriers is the source of the THz pulses.

As Fig.2.2 shown, THz pulses can be emitted from a PC antenna under fs laser pulse excitation and a bias voltage. A typical PC antenna THz emitter consists of two metal electrodes deposited on a semiconductor substrate. between the electrodes, a DC bias is applied. In the electrode gap, fs optical pulses shutter the carriers (electrons and holes) in the semiconductor, the photon energy of the excitation pulses should be larger than the bandgap energy. The bias field induced by the DC voltage accelerates the photocarriers, at the same time, the charge density declines primarily by trapping of carriers in defect sites on the time scale of carrier lifetimes. THz field emits from

the impulse current arising from the acceleration and decay of photon carriers, the polarization of the THz emission depends on the geometry of the electrode.

PC antennas can be designed in various forms, for example, bow-tie, dipole, logarithmic periodic, and logarithmic spiral antennas. The latter two types, however, are only used for continuous-wave THz generation by photomixing and not used in generating broadband THz pulses, since in these two types, the polarization orientations are for different frequency components of THz emission. Typical scales of the PC antennas are a few $\mu m^2$ for the photoconductive gap and several tens of $\mu$m for the metal electrodes. Commonly the peak emission frequency of PC antennas lies in the sub-THz to 1 THz region. [44]

Because the typical scale of a PC antenna is much smaller than the wavelength of the emitted THz radiation, a PC emitter is always modelled as a Hertzian dipole antenna. Since the size of the emitter is comparable to the spot size of the optical beam ($\sim$ 10 $\mu$m), and is much smaller than the wavelength of the THz emission $\lambda_{THz}$ (300 $\mu$m at 1 THz), the validity of dipole approximation is ensured. Here we only concern about the THz emission in the so-called far-field range, where the radiation fields is at large distances from the emitter: $r \gg \lambda_{THz}$. [5]

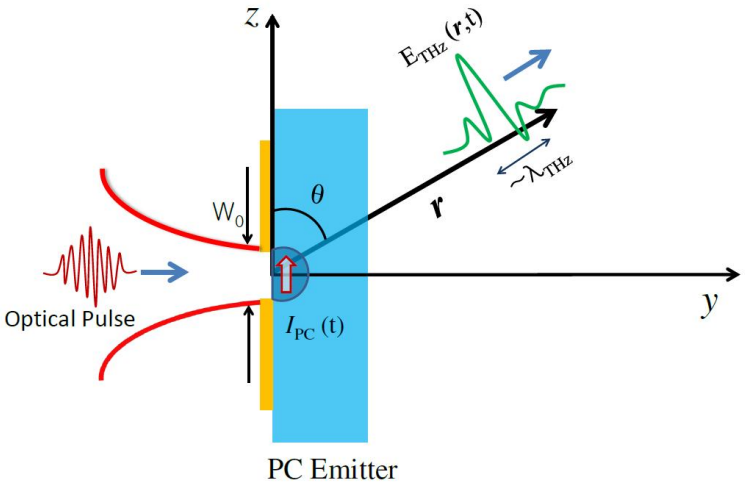


**Figure 2.3: Electric dipole radiation from a PC emitter** - Laser spot size $w_0$~10 $\mu$m, THz emission $E_{THz}(\boldsymbol{r},t)$, $\boldsymbol{r} \gg \lambda_{THz}$.

As described in ref.[5], and as shown in Fig.2.3, a focused optical pulse is gating a

PC THz emitter, the spot size $w_0$ of the focused optical beam is in dimension of $\sim 10\ \mu$m, a bias DC voltage is applied between two electrodes, then the photoconductive current $I_{PC}$ generated in the substrate is a function of time. As a result, the THz wave $E_{\mathrm{THz}}(\boldsymbol{r},t)$ is emitted in the azimuthal angle $\theta$. The free-space dipole radiation in far-field region can be written as eq.2.1:

$$E_{THz}(t) = \frac{\mu_0}{4\pi}\frac{sin\theta}{r}\frac{d^2}{dt_r^2}[p(t_r)]\vec{e_\theta}, \tag{2.1}$$

where $p(t_r)$ is the dipole moment of the source at the delayed time $t_r = t - r/c$. The time derivative of the dipole moment can be expressed as eq.2.2:

$$\frac{d\mathbf{p}(t)}{dt} = \frac{d}{dt}\int \rho(\mathbf{r}',t)\mathbf{r}'d^3\mathbf{r}' = \int \mathbf{r}'\frac{\partial\rho(\mathbf{r}',t)}{\partial t}d^3\mathbf{r}', \tag{2.2}$$

from electrodynamics, the photocurrent density $\rho(\mathbf{r},t)$ and the charge carrier density $\mathbf{J}(\mathbf{r},t)$ should obey the continuity equation, eq.2.3:

$$\nabla\cdot\mathbf{J} + \frac{\partial\rho}{\partial t} = 0, \tag{2.3}$$

then the integration can be written as eq.2.4:

$$\frac{d\mathbf{p}(t)}{dt} = -\int \mathbf{r}'\nabla\cdot\mathbf{J}(\mathbf{r}',t)d^3\mathbf{r}' = \int \mathbf{J}(\mathbf{r}',t)d^3\mathbf{r}', \tag{2.4}$$

to simplify the discussion, here we assume the carrier transportation is in one dimension (lies in z axis in Fig.2.3) , then eq. 2.4 is simplified to eq.2.5:

$$\frac{dp(t)}{dt} = \int J(z',t)d^3\mathbf{r}' = \int_{-w_0/2}^{w_0/2} I_{PC}(z',t)dz' = w_0 I_{PC}(t), \tag{2.5}$$

in which $w_0$ is the spot size of the optical beam, and $I_{PC}$ is the photocurrent, finally the THz emission can be expressed as eq.2.6:

$$\mathbf{E}_{THz}(t) = \frac{\mu_0 w_0}{4\pi}\frac{sin\theta}{r}\frac{d}{dt_r}[I_{PC}(t_r)]\vec{e_\theta} \propto \frac{dI_{PC}(t)}{dt}. \tag{2.6}$$

From eq.2.6, it can be straightforwardly concluded that the THz radiation is proportional to the time derivative of the photocurrent between the antenna gap. And following the deductions in [5, 60, 61], by introducing Lorentz-Drude model to describe the carrier dynamics of the photon-excited electron-hole pairs, and assuming

the optical pulse is Gaussian with a pulse duration of $2\sqrt{ln2}\tau_p$, finally, the photocurrent is determined by several parameters: DC bias field $E_{DC}$, the max value of optical Gaussian pulse $I^0_{opt}$, and a function related to constants including momentum relaxation time $\tau_s$, carrier lifetime $\tau_c$ of the substrate material, and the optical pulse duration $\tau_p$. The final equation have the form that shown in eq.2.7:

$$\mathbf{E}_{THz}(t) \propto \frac{dI_{PC}(t)}{dt} \quad , \quad I_{PC}(t) \propto E_{DC} I^0_{opt} f(\tau_s, \tau_c, \tau_p, t). \tag{2.7}$$

From eq.2.7, the output power of a PC emitter depends on two parameters: the bias voltage and the optical pump power. When the optical pump power is low and the bias field is weak, the amplitude of the THz radiation increases linearly with both parameters [62]. The breakdown voltage and the saturation of photon-carriers in the substrate material limits the maximum THz emission power. The breakdown field of LT-GaAs is reported to be ~ 300 kV/cm [62], which corresponds to a 150 V bias voltage for a 5 $\mu$m gap space. The THz output power saturates at high optical pump power, this saturation physically originates from the screening of the bias field by photon-carriers.

### 2.1.2 Time-Domain Detection of Terahertz Pulses with Photoconductive Antennas

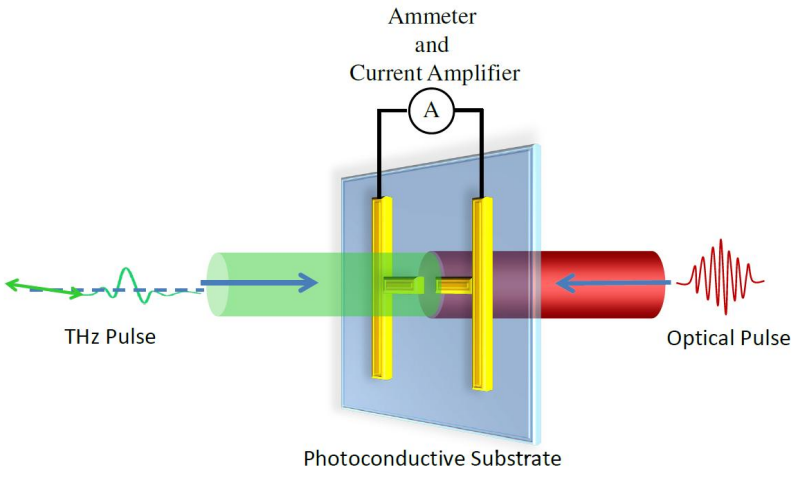


**Figure 2.4: Schematic diagram of THz pulse detection with a PC antenna** - Photocarriers exited by the optical pulse accelerate under the THz electric field, then the photocurrent is measured with an ammeter.

The underlying physical mechanism of THz detection using a PC antenna is a reversal to that of THz emission from a PC emitter, so the dynamics of photocarriers discussed in the last section can be directly applied to THz wave detection. Figure 2.4 is a analogue to Fig.2.2, which sketching THz detection with a PC antenna, a fs optical pulse is gating the antenna. Different from PC THz emission, in detection, without a DC bias voltage applied between the electrodes, a voltage induced by the THz electric field will accelerate the photocarriers then generates photocurrent in the gap. Same as a emitter, the photocurrent lasts for the carrier lifetime, which is much shorter than the THz pulse duration, so it fits for time-domain waveform measurement. Typically, a photocurrent is quite weak that in the sub-nanoamp scale, thus current amplifiers are necessary to convert such weak current signals into measurable voltages. In order to enhance the SN ratio, the signal is always processed by a lock-in amplifier synchronized with a wave chopper. This method is called photoconductive sampling or, briefly, PC sampling.

As described in ref.[6], in PC sampling the photocurrent in the antenna is [63]:

$$J(t) = \int v(t)g(t-t')dt, \tag{2.8}$$

where $v$(t) is the voltage between the photoconductive gap, given by eq.2.9:

$$v(t) = \int H(\omega)E(\omega)e^{i\omega t}d\omega, \tag{2.9}$$

here the incident electric field $E_{\mathrm{THz}}(t)$ is Fourier transformed to the frequency domain, written as $E(\omega)$, and $H(\omega)$ is the transfer function of the antenna, which is defined as the ratio between the voltage induced at the antenna electrodes and the incident electric field. The photocurrent is given by:

$$J(t) = \int I(t')[1 - e^{1-exp(t-t')/\tau_s}]e^{(t-t')/\tau_c}dt'. \tag{2.10}$$

where $I(t')$ is the intensity of the laser excitation. From eq.2.10, it is concluded that the output signal of PC detection depends on not only the incident field $E_{\mathrm{THz}}(t)$, but also the momentum relaxation time $\tau_s$ and the carrier lifetime $\tau_c$ of the semiconductor substrate. It was experimentally proved that when THz detection is implemented with a short dipole without a substrate lens, $H(\omega) = 1$, then $v(t)$ becomes linearly proportional to the incident THz signal $E_{\mathrm{THz}}(t)$ [63].

Moreover, eq.2.9 is also showing that the transfer function of the antenna $H(\omega)$ limits the detection bandwidth of a PC detector, then the detection bandwidth will depend on the carrier dynamics in the semiconductor substrate. It means the photocurrent signal is not an exact replica of the real THz waveform, but exhibits frequency filtering through the conductivity. Commonly in the PC sampling method the bandwidth is limited to up to ~4 THz due to antenna parameters.

## 2.2 Generation and Detection of Terahertz Pulses Based on Nonlinear Effects in Crystals

Optical rectification and electro-optic effect are twin second-order nonlinear processes which principally inverse to each other, in both processes, an ultrafast optical pulse is involved with an electro-optical material, to generate or detect the THz radiation. Materials can be used in this method include zinc-blende semiconductors (GaAs, GaP, ZnTe, CdTe, InP), $LiNbO_3$, $LaTiO_3$, or organic crystals (DAST) [64, 65].

Physically, the optical rectification processes produce transient polarizations $P(t)$, when fs optical pulses illuminate an electro-optical material, these transient polarizations emit THz radiation to free space. The THz radiation is proportional to the second time derivative of the low-frequency part of $P(t)$, which is similar as the case of a transient dipole. [64]

Very short pulses can be emitted in this method, the time scale is much shorter than the PC antenna method. For example, in ref.[66], a bipolar pulse in the time scale as small as 180 fs (FWHM) is produced using optical rectification. The production efficiency of optical rectification depends on the second-order nonlinear optical coefficients ($\chi^{(2)}$) of the EO materials, and the phase matching conditions. The spectral content of the THz radiation produced by this method is much broader attaining 50 THz than that produced using the PC antenna method [67].

In this work, zinc-blende crystals are used for THz generation and detection, zinc-blende semiconductors are among the most commonly used EO materials in THz generation/detection. When the photon energy of the excitation laser is larger than the crystal bandgap energy($E_{photon} > E_g$), as in the case of unbiased GaAs, two physical mechanisms are involved in THz emission: the carrier's acceleration, and optical rectification. The first mechanism is canceled when the laser excitation normally incidents to the crystals, so that only optical rectification contributes to the THz emission [68]. Moreover, optical rectification can be obtained by employing photons that have smaller energy than the semiconductor bandgap energy($E_{photon} < E_g$) to illuminate the crystals. In this method, the amplitude of the THz emission strongly depends on the optical pulse polarization and the crystallographic orientation. [6]

On the other hand, besides PC detectors, also free-space electro-optic (EO) sampling measurements register the electric field of THz pulses in the time domain, in these

measurements, both amplitude and phase can be obtained at the same time with high precision. The EO sampling makes use of the Pockels effect in EO crystals. The Pockels effect is a physical reversal to optical rectification, an optical probe field and the THz field are involved in this effect. Because the Pockels effect happens instantaneously in THz measurements, the outputs of free space EO sampling measurements are directly proportional to $E_{\mathrm{THz}}(t)$ [69]. In EO sampling measurements, the THz electric field will introduce a phase retardation $\delta\phi$ of the optical field over the distance $\delta z$; such phase retardation strongly depends on the electro-optic crystal type and orientation. Free-space EO sampling utilizes various electro-optic crystals: uniaxial crystals like $LaTiO_3$ or $LiNbO_3$ ; or isotropic crystals like ZnTe(110) with a zinc-blende structure. ZnTe is a material for which a high signal-to-noise ratio was obtained.

In comparison between PC sampling and free-space EO sampling, free-space EO sampling is able to detect signals in a much larger bandwidth (100 GHz-37 THz) [70].

### 2.2.1 THz Emission with Optical Rectification in Nonlinear Crystals

Optical rectification is a second order nonlinear effect in crystals. With excitation at a single frequency $\omega$, the second order nonlinear polarization includes two terms: the sum frequency term $P^{(2)}(\omega+\omega)$, which is also known as second harmonic generation (SHG); and the optical difference frequency term $P^{(2)}(\omega-\omega)$, it is a DC signal which is known as optical rectification.

With a fs pulse excitation, in the spectrum range of the pulse $\omega_{pulse}$, the sum and difference frequency components occur between arbitrary two frequencies $\omega_1$ and $\omega_2$ $(\omega_1, \omega_2 \in \omega_{pulse})$ :

$$P_i^{(2)\pm}(\omega_3 = \omega_1 \pm \omega_2) = \sum_{\omega_3=\omega_1\pm\omega_2} \sum_{jk} \epsilon_0 \chi_{ijk}^{(2)}(\omega_3 = \omega_1 \pm \omega_2) E_j(\omega_1) E_k(\pm\omega_2), \qquad (2.11)$$

where $\chi_{ijk}^{(2)}$ is the second-order nonlinear coefficient, and $(i, j, k) = x, y, z$ is the coordinate label, in THz generation, only difference frequency term $P_i^{(2)-}(\Omega)$ $(\Omega \equiv \omega_1 - \omega_2)$ is considered, then eq.2.11 is rewritten in the form :

$$P_i^{(2)-}(\Omega) = \int_{-\infty}^{\infty} \sum_{jk} \epsilon_0 \chi_{ijk}^{(2)} E_j(\omega_2 + \Omega) E_k^*(\omega_2) d\omega_2. \qquad (2.12)$$

The time domain equation is obtained from the Fourier transform of eq.2.12,

$$\begin{aligned} P_i^{(2)-}(t) &= \mathcal{F}^{-1}[P_i^{(2)-}(\Omega)] = \int_{-\infty}^{\infty} P_i^{(2)-}(\Omega) e^{i\Omega t} d\Omega \\ &= \int_{-\infty}^{\infty}\int_{-\infty}^{\infty} \sum_{jk} \epsilon_0 \chi_{ijk}^{(2)} E_j(\omega_2+\Omega) E_k^*(\omega_2) d\omega_2 e^{i\Omega t} d\Omega \\ &= \sum_{jk} \epsilon_0 \chi_{ijk}^{(2)} \int_{-\infty}^{\infty} E_j(\omega_2+\Omega) e^{i(\omega_2+\Omega)t} d\Omega \int_{-\infty}^{\infty} E_k(\omega_2) e^{-i\omega_2 t} d\omega_2 \\ &= \sum_{jk} \epsilon_0 \chi_{ijk}^{(2)} E_j(t) E_k(t) \propto I(t). \end{aligned} \tag{2.13}$$

Now we write a full version of eq.2.12 including propagation terms, and take $\omega_2$ as a parameter in $P_i^{(2)-}$, as eq.2.14:

$$\begin{aligned} P_i^{(2)-}(\omega_2;\Omega) e^{i(\mathbf{k}(\Omega)\cdot\mathbf{r}-\Omega t)} &= \sum_{jk} \epsilon_0 \chi_{ijk}^{(2)} E_j(\omega_2+\Omega) e^{i[\mathbf{k}(\omega_2+\Omega)\cdot\mathbf{r}-(\omega_2+\Omega)t]} E_k^*(\omega_2) e^{-i[\mathbf{k}(\omega_2)\cdot\mathbf{r}-\omega_2 t]} \\ &= \sum_{jk} \epsilon_0 \chi_{ijk}^{(2)} E_j(\omega_2+\Omega) E_k^*(\omega_2) e^{i[(\mathbf{k}(\omega_2+\Omega)-\mathbf{k}(\omega_2))\cdot\mathbf{r}-\Omega t]}. \end{aligned} \tag{2.14}$$

From eq.2.14, the second-order polarization $P_i^{(2)-}(\omega_2;\Omega)$ has an imaginary term $e^{i\Delta_\mathbf{k}\cdot\mathbf{r}}$, where $\Delta\mathbf{k}(\Omega) \equiv \mathbf{k}(\Omega) - \mathbf{k}(\Omega+\omega_2) + \mathbf{k}(\Omega_2)$, it means, if $\Delta\mathbf{k}(\Omega)$ is equal to zero, the THz emission at different position in the crystal will be in phase, then the constructive interference induces strong THz radiation; either $\Delta\mathbf{k}(\Omega)$ is not equal to zero, the destructive interference in crystal will weaken the THz radiation.

In the identical equation $\Delta\mathbf{k}(\Omega) \equiv \mathbf{k}(\Omega) - \mathbf{k}(\Omega+\omega_2) + \mathbf{k}(\Omega_2)$, it should be noticed that $\Omega \ll \omega_2$, so we write the Taylor series of $\Delta\mathbf{k}(\Omega)$, and reserve only the first derivation:

$$\Delta\mathbf{k}(\Omega) = \left.\frac{dk}{d\omega}\right|_{\omega=\omega_2} \Omega - \mathbf{k}(\Omega). \tag{2.15}$$

Referring the dispersion relationship, note that the group refractive index $n_{gr}(\omega_2) = c \left.\frac{dk}{d\omega}\right|_{\omega=\omega_2}$, and the refractive index $n_{ph}(\Omega) = c\frac{k(\Omega)}{\Omega}$. Consequently, velocity matching in a dispersive medium can be achieved only for a certain THz frequency when the optical pulse envelope travels at the phase velocity of the monochromatic THz wave. The optimal velocity-matching condition for a broadband THz pulse is that the optical

group velocity is the same as the phase velocity of the central frequency of the THz spectrum.

In the experiments of this thesis, ZnTe and GaP are used for THz generation, the constants are listed below [65]:

**Table 2.1:** Constants of *ZnTe* and *GaP*

| Crystal | EO Coefficient (pm/V) @($\mu$m) | refractive Index @($\mu$m) | Group Refractive Index | Refractive Index @(THz) |
|---|---|---|---|---|
| ZnTe | 4.04 @ 0.633 | 2.853 @ 0.8 | 3.31 | ~3.19 |
| GaP | 1.43 @ 1.150 | 3.61 @ 0.886 | 3.57 | ~3.4 |

So we summarize the characters of ZnTe and GaP as below:

- ZnTe is the most widely used nonlinear crystals for THz generation, due to the useful characteristics of ZnTe: velocity-matching near 800 nm, high transparency at optical and THz frequencies, and large EO coefficient. However, the phonon of ZnTe exhibits large absorption from 3 THz, so it is difficult to generate THz emission higher than 3 THz with ZnTe.

- GaP are also zinc-blende crystals, in comparison with ZnTe, the EO coefficient is smaller, and for widely used Ti:Sapphire fs lasers at 800 nm, the velocity-matching condition is not satisfied, the velocity-matching condition satisfies when choosing lasers with wavelength of about 1000 nm as the excitation. Nevertheless, the lowest phonon resonance energy is larger than ZnTe, that allows the THz emission to broaden to 7 THz; also GaP is heavily used in semiconductor industry, so it is easy to get large and high qualified samples.

### 2.2.2 The Polarization of THz Radiation from Nonlinear Crystals

As described in ref.[5], in eq.2.12, $\chi^{(2)}_{ijk}$ is the second-order nonlinear susceptibility tensor element in the crystal coordinate system. When the indices are permutable, we can use the contracted notation:

$$d_{il} = \frac{1}{2}\chi^{(2)}_{ijk}, \tag{2.16}$$

where

$$\begin{array}{cccccc} l = 1 & 2 & 3 & 4 & 5 & 6 \\ jk = 11 & 22 & 33 & 23, 32 & 31, 13 & 12, 21 \end{array} \tag{2.17}$$

Substituting 2.17 to 2.12, then the second-order polarization in nonlinear crystals can be expressed as:

$$\begin{pmatrix} P_x \\ P_y \\ P_z \end{pmatrix} = 2\epsilon_0 \begin{pmatrix} d_{11} & d_{12} & d_{13} & d_{14} & d_{15} & d_{16} \\ d_{21} & d_{22} & d_{23} & d_{24} & d_{25} & d_{26} \\ d_{31} & d_{32} & d_{33} & d_{34} & d_{35} & d_{36} \end{pmatrix} \begin{pmatrix} E_x^2 \\ E_y^2 \\ E_z^2 \\ 2E_yE_z \\ 2E_zE_x \\ 2E_xE_y \end{pmatrix}. \tag{2.18}$$

If the cryptographic system is highly symmetric, many of the 18 tensor elements vanish, moreover, only a few nonvanishing elements are independent. ZnTe and GaP used in the experiments of this thesis are zinc-blende crystals, zinc-blende crystals has the crystal class of $\bar{4}3m$. This crystal class has three nonvanishing contracted matrix elements and only one of them is independent: $d_{14} = d_{25} = d_{36}$, and its *d-matrix* is:

$$\begin{pmatrix} 0 & 0 & 0 & d_{14} & 0 & 0 \\ 0 & 0 & 0 & 0 & d_{14} & 0 \\ 0 & 0 & 0 & 0 & 0 & d_{14} \end{pmatrix}. \tag{2.19}$$

When an optical fs pulse incidents into zinc-blende crystals, the THz radiation depends on the direction of the optical field in the crystal coordinate system. An arbitrary optical field in the crystal frame can be expressed as:

$$\mathbf{E}_0 = E_0 \begin{pmatrix} \sin\theta\cos\phi \\ \sin\theta\sin\phi \\ \cos\theta \end{pmatrix}, \tag{2.20}$$

here $\theta$ and $\phi$ are polar and azimuthal angle respectively, substitute eq.2.19 and eq.2.20 to eq.2.18, we have the nonlinear polarization in the crystals:

$$\begin{aligned} \begin{pmatrix} P_x \\ P_y \\ P_z \end{pmatrix} &= 2\epsilon_0 d_{14} E_0^2 \begin{pmatrix} 0 & 0 & 0 & 1 & 0 & 0 \\ 0 & 0 & 0 & 0 & 1 & 0 \\ 0 & 0 & 0 & 0 & 0 & 1 \end{pmatrix} \begin{pmatrix} \sin^2\theta\cos^2\phi \\ \sin^2\theta\sin^2\phi \\ \cos^2\phi \\ 2\sin\theta\cos\theta\sin\phi \\ 2\sin\theta\cos\theta\cos\phi \\ 2\sin_2\theta\sin\phi\cos\phi \end{pmatrix}. \\ &= 4\epsilon_0 d_{14} E_0^2 \sin\theta \begin{pmatrix} \cos\theta\sin\phi \\ \cos\theta\cos\phi \\ \sin\theta\sin\phi\cos\phi \end{pmatrix} \end{aligned} \tag{2.21}$$

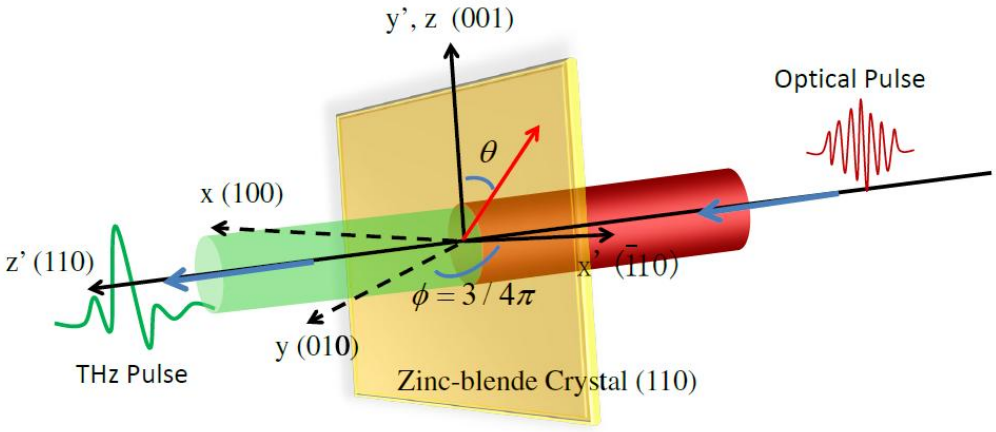


**Figure 2.5: A linearly polarized optical wave is incident on a zinc-blende crystal(110) normally** - $\theta$ is the angle between the optical field and the (001) axis.

Here we consider the laser incident normally on the (110) plane of zinc-blende crystal, in this case, from eq.2.21, the THz emission amplitude reaches the maximum, and $\phi = 3/4\pi$, as shown in Fig.2.5. Under this condition, eq.2.21 is written as:

$$\begin{pmatrix} P_x \\ P_y \\ P_z \end{pmatrix} = 2\epsilon_0 d_{14} E_0^2 \sin\theta \begin{pmatrix} \sqrt{2}\cos\theta \\ -\sqrt{2}\cos\theta \\ -\sin\theta \end{pmatrix}. \tag{2.22}$$

and in the lab coordinate system $x'(\bar{1}10)y'(001)z'(110)$, the nonlinear polarization is written as eq.2.23:

$$\begin{pmatrix} P_{x'} \\ P_{y'} \\ P_{z'} \end{pmatrix} = 2\epsilon_0 d_{14} E_0^2 \sin\theta \begin{pmatrix} -2\cos\theta \\ -\sin\theta \\ 0 \end{pmatrix}. \tag{2.23}$$

From eq.2.23, it can be concluded the the maximum intensity of THz emission is obtained at $\theta = \sin^{(-1)} \sqrt{2/3}$,($\theta \approx 55°$). This angle corresponds to an optical field that is parallel to either the $(\bar{1}11)$ or $(1\bar{1}1)$ axis. In this case, the emitted THz polarization is parallel to the polarization of the incident laser pulse.

In chapter 5, the case of the laser incident direction lies normal to the (111) plane of zinc-blende crystals will be discussed.

### 2.2.3 Free-Space Electro-Optic Sampling

Utilizing the Pockels effect in EO crystals, Free-space EO sampling measures THz electric field in time domain. The Pockels effect is also related to the second-order polarization in nonlinear crystals, it is a principally reversal to optical rectification, it is shown as eq.2.24:

$$\begin{aligned} P_i^{(2)-}(\Omega) &= 2\sum_{jk} \epsilon_0 \chi_{ijk}^{(2)} E_j(\omega) E_k(\Omega) \\ &= \sum_j \epsilon_0 \chi_{ij}^{(2)} E_j(\omega), \end{aligned} \tag{2.24}$$

where $\chi_{ij}^{(2)} = 2\sum_k \chi_{ijk}^{(2)} E_k(\Omega)$ is the susceptibility tensor induced by the THz electric field. From Eq.2.24, it is concluded that when applying an static electric field in a nonlinear crystal, the field will introduce birefringence to the crystal, and the birefringence is proportional to the applied field amplitude. So inversely, by measuring the field-induced birefringence, the applied field amplitude can be determined.

In free-space EO sampling measurements, ZnTe is most commonly used, since the useful characteristics of ZnTe for THz generation (velocity-matching near 800 nm,

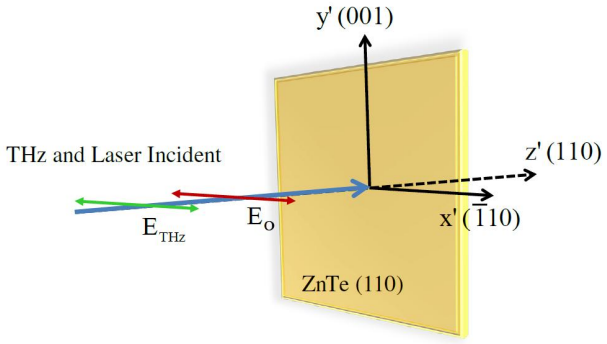


**Figure 2.6: THz measurement with Pockels effect in ZnTe(110)** - Both the THz electric field and the optical polarization are parallel to the $(\bar{1}10)$ axis.

high transparency at optical and THz frequencies, and large EO coefficient) also fit for efficient EO sampling measurements. In the measurements, always the (110) oriented ZnTe crystals are used, because in this orientation, similar as discussed in generation mechanisms that the THz emission reaches maximum, the field induced birefringence is also maximized when both the THz electric field and the optical polarization are parallel to the $(\bar{1}10)$ axis, as Fig.2.6 shown. Under this setup, the nonlinear polarization in eq.2.24 is expressed as:

$$\begin{aligned}\begin{pmatrix} P_x \\ P_y \\ P_z \end{pmatrix} &= 4\epsilon_0 d_{14} \begin{pmatrix} 0 & 0 & 0 & 1 & 0 & 0 \\ 0 & 0 & 0 & 0 & 1 & 0 \\ 0 & 0 & 0 & 0 & 0 & 1 \end{pmatrix} \begin{pmatrix} E_{O,x}E_{\mathrm{THz,x}} \\ E_{O,y}E_{\mathrm{THz,y}} \\ E_{O,z}E_{\mathrm{THz,y}} \\ E_{O,y}E_{\mathrm{THz,z}} + E_{O,z}E_{\mathrm{THz,y}} \\ E_{O,z}E_{\mathrm{THz,x}} + E_{O,x}E_{\mathrm{THz,z}} \\ E_{O,x}E_{\mathrm{THz,y}} + E_{O,y}E_{\mathrm{THz,x}} \end{pmatrix} \\ &= 4\epsilon_0 d_{14} \begin{pmatrix} 0 \\ 0 \\ E_{O,x}E_{THz,y} + E_{O,y}E_{THz,x} \end{pmatrix} \\ &= -4\epsilon_0 d_{14} E_O E_{THz} \hat{\mathbf{z}},\end{aligned} \tag{2.25}$$

where $E_O$ and $E_{\mathrm{THz}}$ represent the optical electric field and the THz electric field respectively:

$$\mathbf{E}_O = \frac{E_O}{\sqrt{2}}\begin{pmatrix}-1\\1\\0\end{pmatrix} \quad and \quad \mathbf{E}_{\mathrm{THz}} = \frac{E_{\mathrm{THz}}}{\sqrt{2}}\begin{pmatrix}-1\\1\\0\end{pmatrix}. \tag{2.26}$$

The THz field induced nonlinear polarization will vary the polarization of the detection optical field, in the case described in eq.2.25, the nonlinear polarization is orthogonal to the incident optical field, it means when a linearly polarized optical probe passing through a ZnTe(110) detection crystal simultaneously with a THz field, then the THz field induced birefringence will lead the probe pulse evolves into an elliptically polarized pulse.

The the THz electric field induced ellipticity resulted can be transferred to current difference and measured with a balanced-detection system, by introducing a setup shown in Fig.2.7. In this setup, the THz field induced birefringence makes the probe pulse to be slightly elliptically polarized, when a linearly polarized optical probe pulse and the THz pulse pass through the EO crystal at the same time, the probe pulse sequently passing through a QWP, and evolves into an almost circularly, but in fact elliptically polarized pulse. After the QWP, a Wollaston prism is placed and splits the probe pulse into two orthogonal components, these two components travel to a balanced-detection system, such detection system measures the intensity difference $I = I_{y'} - I_{x'}$ between these two orthogonal components. From the description above, this intensity difference is proportional to the THz amplitude.

When a probe pulse travels through a crystal with thickness $L$, due to the Pockels effect, the differential phase retardation $\Delta\varphi$ of the pulse is given as:

$$\Delta\varphi = (n_y - n_x)\frac{\omega L}{c} = \frac{\omega L}{c} n_O^3 r_{41} E_{\mathrm{THz}}, \tag{2.27}$$

where $n_x$ and $n_y$ are refractive index at the optical frequency for $x$- and $y$- polarized pulses, $n_O$ is the refractive index at the optical frequency and $r_{41} = d_{14}$= 4 pm/V is the EO coefficient. The intensities of the two probe beams at the balanced photo-detector are (assuming $\Delta\varphi$ is very small, actually, in EO sampling, it holds true):

$$\begin{aligned} I_{x'} &= \frac{I_0}{2}(1 - \sin\Delta\varphi) \approx \frac{I_0}{2}(1 - \Delta\varphi) \\ I_{y'} &= \frac{I_0}{2}(1 + \sin\Delta\varphi) \approx \frac{I_0}{2}(1 + \Delta\varphi) \end{aligned}, \tag{2.28}$$

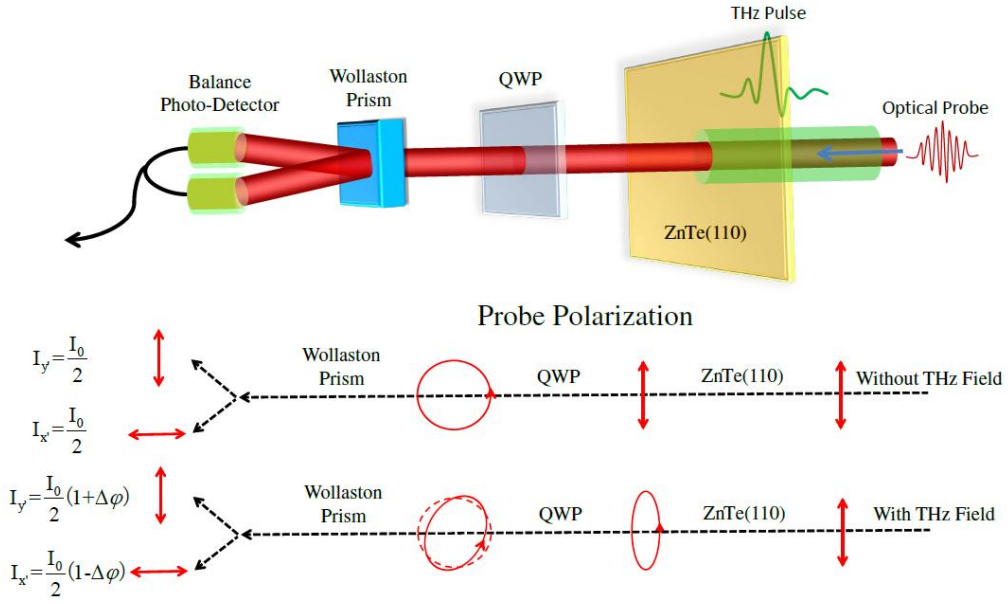


**Figure 2.7: Free-space EO sampling balance measurement** - THz electric field is measured finally by a balanced-detector.

where $I_0$ is the incident probe intensity. Thus, the THz field amplitude is determined by the signal of the balanced photo-detection system:

$$I = I_{y'} - I_{x'} = I_0 \Delta\varphi = \frac{I_\omega L}{c} n_O^3 r_{41} E_{\mathrm{THz}} \propto E_{\mathrm{THz}}. \tag{2.29}$$

Similar as PC detectors, in a realistic situation the temporal or spectral resolution of EO sampling is limited by a detector response function $H(\omega, \omega_{\mathrm{THz}})$, in EO sampling measurements, $H(\omega, \omega_{\mathrm{THz}})$ is mainly determined by three factors: finite pulse duration of optical probe, dispersion of nonlinear susceptibility and mismatch between optical group and THz phase velocity. As a result, the EO signal is the convolution of the THz field with the detector response function $H(\omega, \omega_{\mathrm{THz}})$. For example, with ZnTe(110), the response in frequency range higher than 3 THz is negligible due to the phonon absorption.

## 2.3 Introduction to Terahertz Time Domain Spectroscopy Systems

The typical pulse duration of broadband THz pulses are several ps, then by introducing time-resolved pump-probe technique, the THz pulse shape in time-domain can be registered with fs laser pulses, whose pulse duration is ~ 100 fs, as Fig.2.8 shown.

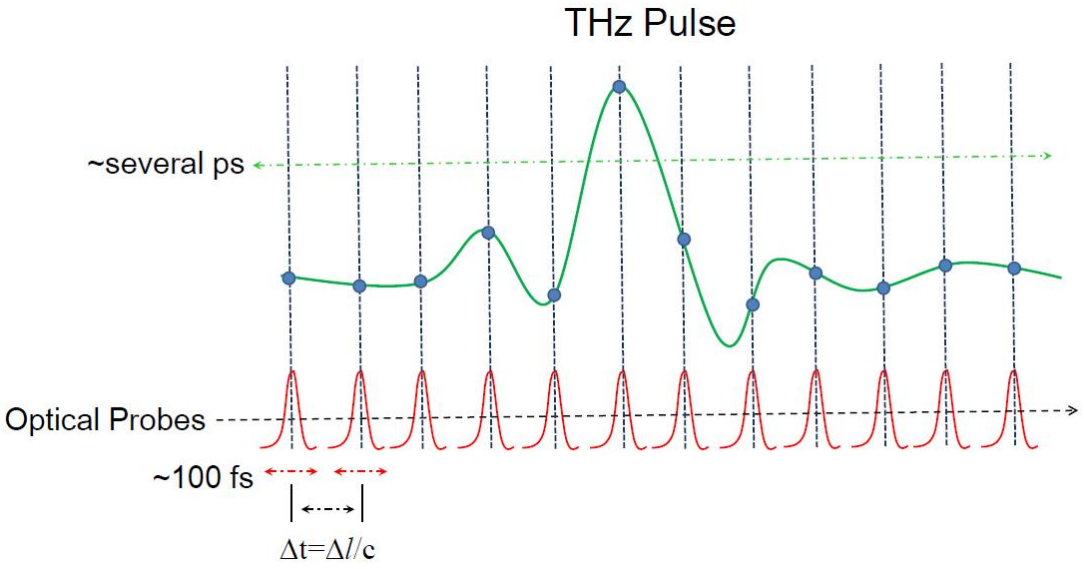


**Figure 2.8: Time-resolved pump-probe measurement of a THz pulse** - THz pulse duration ~several ps, laser pulse duration ~100 fs, the time resolution depends on the laser pulse duration and the time delay $\Delta t$.

The resolution of time-resolved pump-probe measurements depends on two factors: the pulse duration of the fs probe lasers, and the time sampling step $\Delta t$. Commonly, in THz experiments, Ti:Sapphire fs lasers are served as the light sources, the pulse duration is in the scale of 100 fs. In the experiments, time delay is always achieved by a translation line that converts the time sampling step $\Delta t$ to $\Delta l$, the relation between $\Delta t$ and $\Delta l$ is $\Delta t = \Delta l/c$ (c is the speed of light), as shown in Fig.2.9. Because in the measurements, the pulse shape including both amplitude and phase information of each frequency ingredient, this setup is named THz time-domain spectroscopy (THz-TDS) system.

In the THz-TDS measurements, the minimal time sampling step $\Delta t$ and the total sampling time $T$ determine the resolution $\Delta\omega$ and the upper limit $\omega_{\max}$ in the frequency

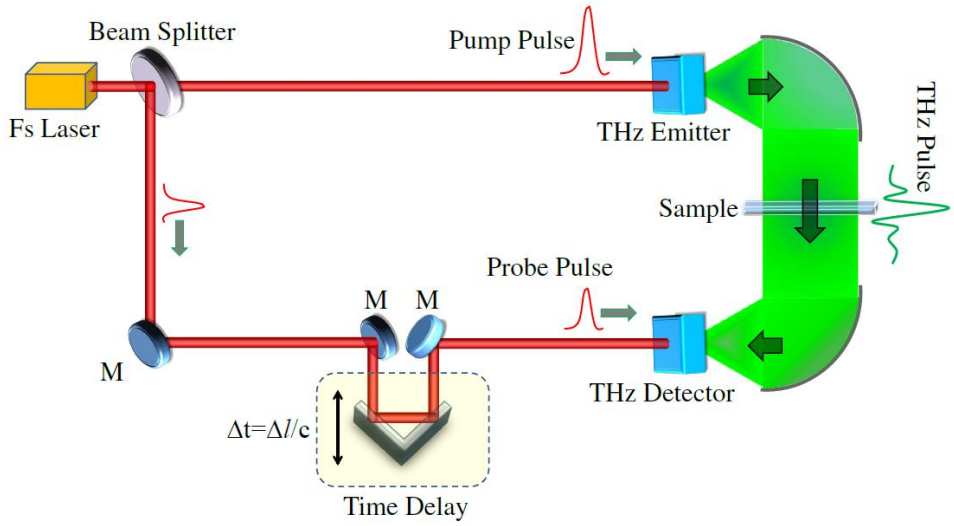


**Figure 2.9: THz time-domain spectroscopy (THz-TDS) system** - M=Mirror, the delay line converts space delay $\Delta l$ to time delay $\Delta t$, $\Delta t = \Delta l/c$ (c is the speed of light).

domain, the relationship can be expressed as eq.2.30:

$$\frac{\Delta\omega}{2\pi} \cdot T = 1; \quad \frac{\omega_{\max}}{2\pi} \cdot \Delta t = 1. \tag{2.30}$$

In Fig.2.9, the THz emitter can be any type of THz sources, e.g., nonlinear crystals, PC antennas; while the THz detector can be both PC antennas and free-space EO sampling systems.

More details about THz-TDS systems in the experiments of this thesis will be introduced in Chapter 3.

Chapter 3

# Basic Experimental Setups

In the present chapter, details of the basic experimental setups in this thesis will be shown. In Chapter 2, the underlying physical mechanisms of THz generation and detection with PC antennas and nonlinear crystals are briefly introduced, the simplest prototype of a THz-TDS setup is discussed. However, in the experiments of this thesis, to analyze THz vector beams, 2D THz-TDS systems are necessary, several modifications and improvements should be made on the THz-TDS setups; and to achieve the best results, optimizations are necessary. These details will be presented hereon, including light sources, parameters, test results and 2D scanning THz-TDS setups.

## 3.1 Light Sources Used in the Experiments

In the experiments of this thesis, mode-locked Ti:Sapphire fs lasers are used as light sources, including Mira900, RegA9000 (Coherent Inc.), Hurricane (Spectra-Physics Lasers, Inc.) and Legend Elite (Coherent Inc.). The specifications of these lasers are shown below.

**Mira900, RegA9000**

RegA9000 (Coherent Inc.) is a Ti:Sapphire fs regeneratively amplified system. The system consists of Mira900 (Coherent Inc.), a CW laser (Verdi V6, Coherent Inc.) pumped mode-locked Ti:Sapphire fs laser, and a regenerative amplifier RegA9000 (Coherent Inc.) pumped with a CW laser (Verdi V10, Coherent Inc.). The output

parameters of RegA9000 are: central wavelength ~ 800 nm, repetition rate ~ 120 kHz, pulse duration ~120 fs, single pulse energy ~10 $\mu$J, output power ~720 mW.

**Verdi (V6, V10)** [71]

Verdi **V** lasers are compact diode-pumped solid state (DPSS) lasers suited for Ti:Sapphire pumping. The working material of Verdi **V** lasers are Nd:$YVO_4$ crystals, which output laser at 1064 nm, the 1064 nm light is frequency doubled in LBO crystals, so finally the output is green CW laser at 532 nm.

**Mira900** [72]

Mira900 mode-locked Ti:Sapphire laser is pumped with the 532 nm light from Verdi V6. Mira900 operates on Kerr lens mode-locking technique. In Kerr lens mode-locking processes, the optical cavities are specifically designed to optimize mode-locking by utilizing changes in the spatial profiles of the beams. These changes originate from optical Kerr effect induced self-focusing effects in Ti:Sapphire crystals, and make the system has the ability to deliver transform limited pulses. The repetition rate of Mira900 is ~76 MHz.

**RegA9000** [72]

RegA9000 is a CW-pumped, Ti:Sapphire regenerative amplifier that amplifies fs pulses at ~120 kHz (up to 300 kHz) repetition rate. RegA9000 requires the output of Mira900 oscillators, it amplifies this output over 1000 times to the $\mu$J level. In RegA9000, inherent group velocity dispersion (GVD) in the amplifier broadens the pulse duration to tens of picoseconds. After extraction, the pulses are re-compressed under 200 fs by a single-grating pulse-compression stage.

**Hurricane** [73]

Hurricane is a Ti:Sapphire regeneratively amplified system produced by Spectra-Physics Lasers Inc., consisting of a seed source and a regenerative amplifier. The seed source is a Ti:Sapphire fs laser MaiTai (Spectra-Physics Lasers Inc.), and the pump laser is Evolution (Spectra-Physics Lasers Inc.) (Q-switched Nd:YLF laser, frequency doubled, output at 527 nm). The output parameters of the system are: central wavelength ~800 nm, repetition rate ~1 kHz, pulse duration ~100 fs, output power ~800 mW.

**Legend Elite** [74]

Legend Elite is a Ti:Sapphire regenerative amplified system produced by Coherent Inc., consisting of a seed source Micra (Coherent Inc.) and a Evolution (Coherent Inc.). Micra (Coherent Inc.) is pumped by Verdi (Coherent Inc.). The output parameters of the system are: central wavelength ~800 nm, repetition rate ~1 kHz, pulse duration ~25 fs, output power ~2.7 W.

In the experiments of recording the intensity profiles of THz vector beams from a segmented GaP(111) crystal with a THz camera (IRV-T0830, NEC Corp.), because of the sensitivity of this camera is relatively low, and the camera tends to be more sensitive in higher frequency range, so the laser Legend Elite was used. In all other experiments in this thesis (except the test experiments in this chapter), Hurricane was used.

## 3.2 Test Results of Antenna Terahertz Detection

In the experiments of this thesis, free-space EO sampling and antenna sampling setups are employed to record THz signals, free-space EO sampling technique is frequently used in Gonokami Group, and more details can be found in ref.[75]. In this section, we will focus on antenna THz detection.

In the experiments, a commercial PC antenna is used, the antenna is among PCA-40-05-10-800 series of Batop Optoelectronics Inc., the details of the antenna are copied from ref.[76]. A photo of the antenna is shown in Fig.3.1.

**Figure 3.1: A photograph of a PCA-40-05-10-800 series antenna(Batop Inc.)** - [76]

PCA-40-05-10-800 series antennas can be used as THz emitters or detectors in pulsed laser THz-TDS systems in the frequency region from 0.1 to 5 THz. The best laser excitation wavelength is ~ 800 nm, and the antenna resonance frequency is near 1THz. The antenna follows a gap design, with a 5 $\mu$m gap laying in the vertical direction, a schema is shown in Fig.3.2, and a photo of the antenna taken under a microscope is shown in Fig.3.3.

Commercially, PCA-40-05-10-800 series antennas are supplied with substrate lenses attached, for the purpose of converging THz emission. However, in this work, we want to exactly analyze the THz field focused with THz lenses of 30 mm and 50 mm focal length, e.g., in Chapter 5, under 30 mm lens focusing, the THz vector field are recorded, and compared with theoretical calculations; and in Chapter 6, the exact THz radially focused field should be submitted to mode overlap calculations. Then when we ordered the antennas, the substrate lenses are asked to be removed and replaced by silicon slabs.

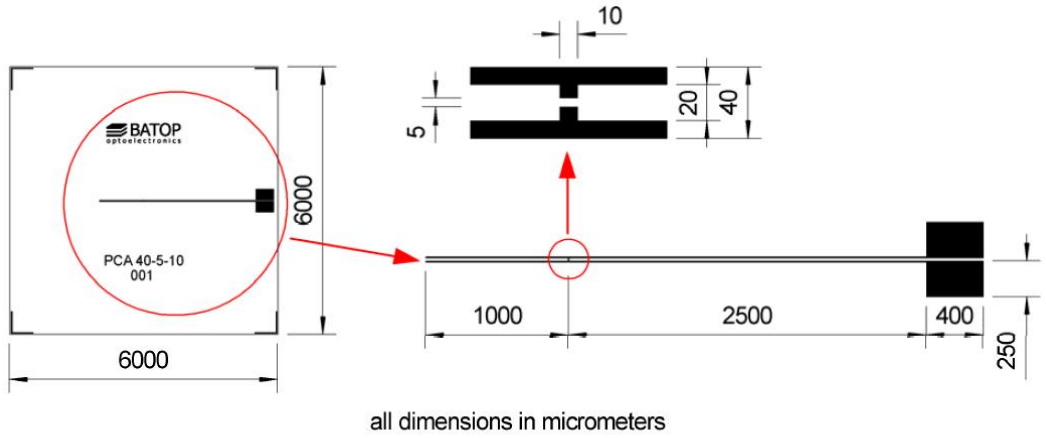


**Figure 3.2: Schema of a PCA-40-05-10-800 series antenna** - [76]

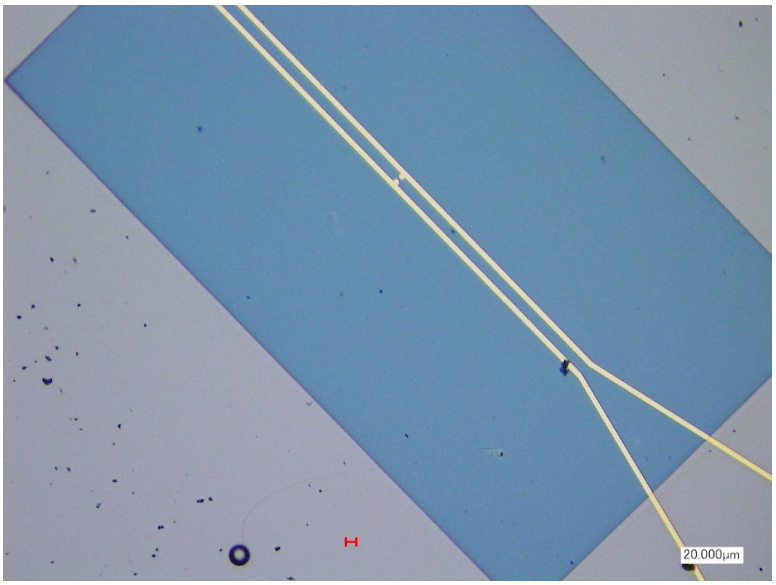


**Figure 3.3: A photo of a PCA-40-05-10-800 series antenna taken under a microscope** - the size of the gap is 5 $\mu$m.

The parameters of PCA-40-05-10-800 series antennas are shown in table 3.1.

**Table 3.1:** PCA-40-05-10-800 Series Antenna Parameters [76]

| Electrical Parameters | Minimum Ratings | Standard | Maximum Ratings |
|---|---|---|---|
| Dark Resistance | 2 MΩ | 2.5 MΩ | 3 MΩ |
| Dark Current @ 10 V | 3 $\mu$A | 4 $\mu$A | 5 $\mu$A |
| Dark Current @ 10 V | | 20 V | 30 V |

Figure 3.4 shows the dark current-voltage curve of PCA-40-05-10-800 series antennas at T = 300 K.

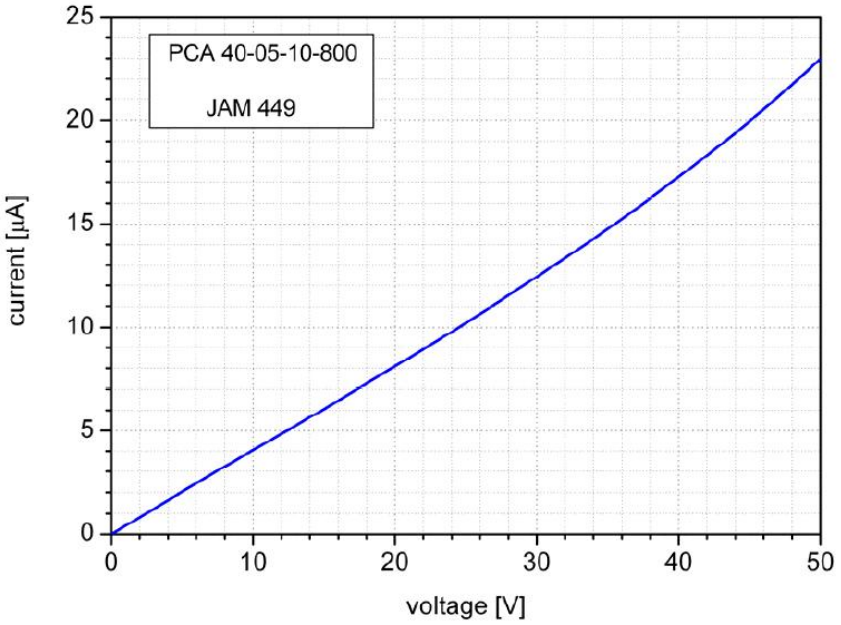


**Figure 3.4: Dark current-voltage characteristic of PCA-40-05-10-800 series antennas** - [76]

The optical characteristics of PCA-40-05-10-800 series antennas are in table 3.2.

**Table 3.2:** Optical Characteristics of PCA-40-05-10-800 Series Antennas [76]

| Optical Excitation Parameters | Minimum Ratings | Standard | Maximum Ratings |
|---|---|---|---|
| Excitation Laser Wavelength | 500 nm | 800 nm | 850 nm |
| Optical Reflectance @ 1040 nm | 32 % @ 500 nm | 7 % @ 800 nm | 8 % @ 850 nm |
| Optical Mean Power | | 40 mW | 80 mW |
| Carrier Recovery Time | | 300 fs | |

The reflection rate of PCA-40-05-10-800 series antennas depends on the wavelength, in the range of 500 ~ 1200 nm, the dependence is shown as:

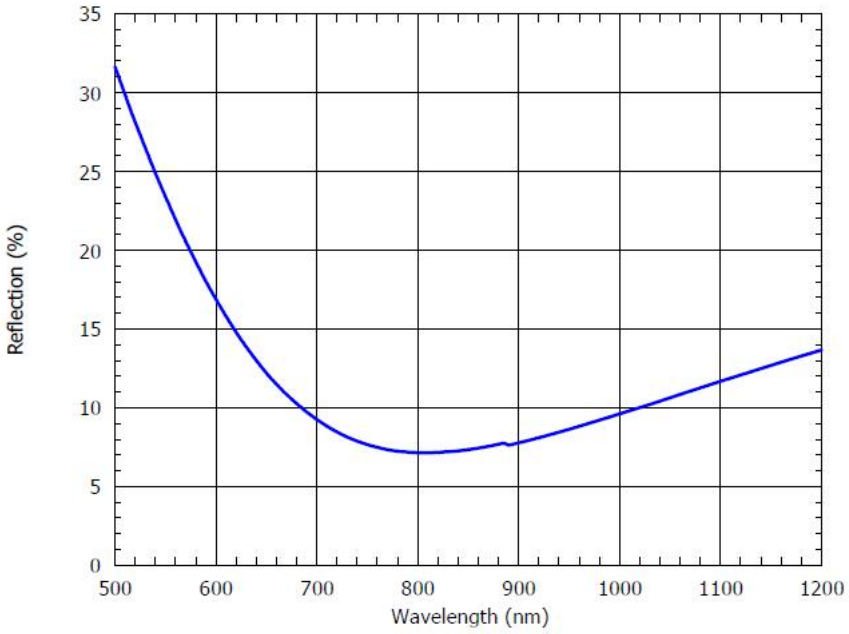


**Figure 3.5: Reflectance dependence of wavelength** - [76]

The resistance(R) dependence of excitation power is shown as:

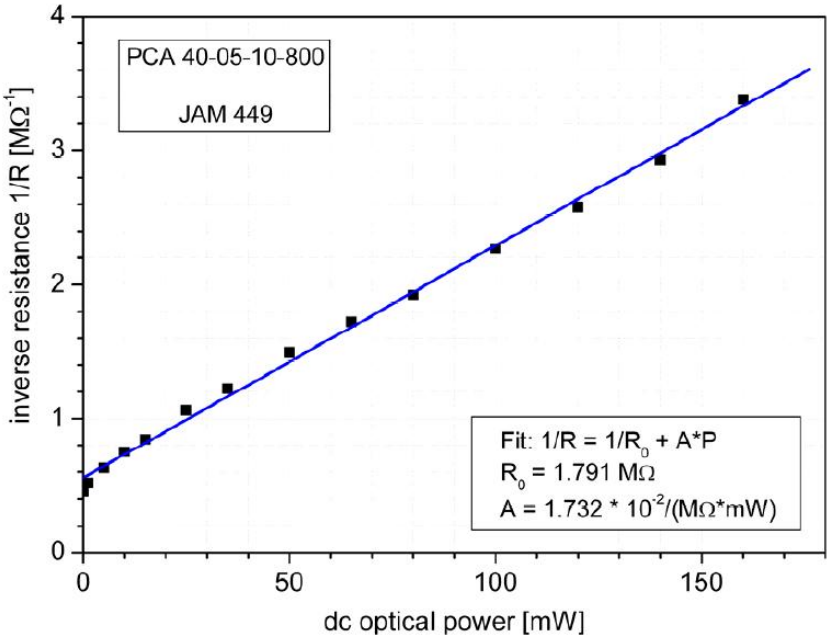


**Figure 3.6: Resistance(R) dependence of excitation power** - [76]

In the experiments of this thesis, a dilemma of choosing the excitation laser presents in PC antenna THz-TDS systems: on one hand, nonlinear crystals are used as THz emitters, lasers with high pulse energy and low repetition rate will increase the amplitude of THz radiation; however on the other hand, for PC antenna detectors, as described in ref.[77], a larger repetition rate laser is better for signal-noise (SN) ratio, because the total charge (current) from the signal increases linearly with the number of sampling pulses, while the charge (current) from noise increases only as the square root of the number of pulses. The laser repetition rate for antenna detection is recommended to be in the order of 100MHz in ref.[77].

To find the best laser for our experiments, Mira900, RegA9000 and Hurricane were tested, the test results are shown below. In all these experiments, lock-in amplifiers were used to achieve better signal-noise(SN) ratio, and for each laser of different repetition rates, the optimizations of the lock-in amplifiers were performed, to ensure the impartiality and validity of the comparison. In comparison with free-space EO sampling setups, which require only small amount (~1%) of the laser power as probe

beams, in PC antenna detection lines, much more powerful probe beams are necessary to excite enough carriers in the photoconductive substrates. As a result, in antenna detection setups, we used 50:50 beam splitters to assign the pump and probe power for Mira900 and RegA9000; while in free-space EO sampling setups, we always use 99:1 beam samplers. Nevertheless, for Hurricane, because of the single pulse energy is large enough , 99:1 beam samplers were used. In all test results, the same ZnTe(110) crystal was used as a THz emitter. In the case of Mira900, the pump laser should be focused on the crystal to ensure the THz signal is detectable. The test setups are shown in Fig.3.7 (Mira900) and Fig.3.8 (RegA9000 and Hurricane).

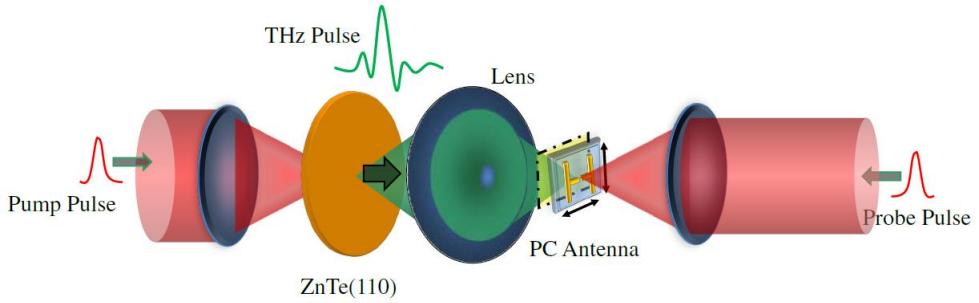


**Figure 3.7: The setup of testing light sources (Mira900)** - Pump:Probe=50:50.

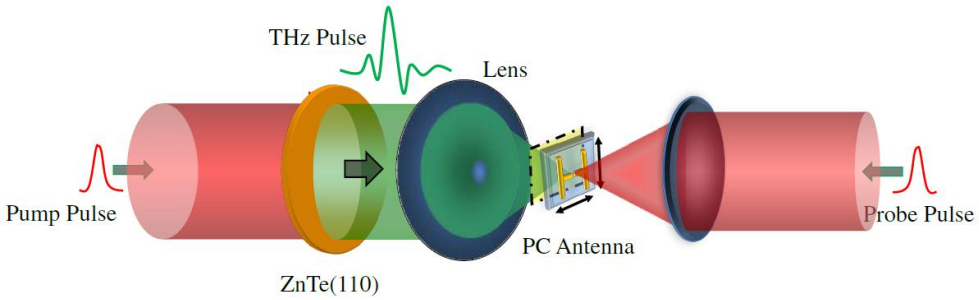


**Figure 3.8: The setup of testing light sources (RegA9000 and Hurricane)** - Pump:Probe=50:50(RegA9000) ; Pump:probe=99:1(Hurricane).

The test results of Mira900 are shown in Fig.3.9 and Fig.3.10, the probe power are

~70mW and ~200mW(maximum respect to the laser output) respectively. From the figures, under the excitation of Mira900, the best SN ratio we obtained was ~ 20 : 1.

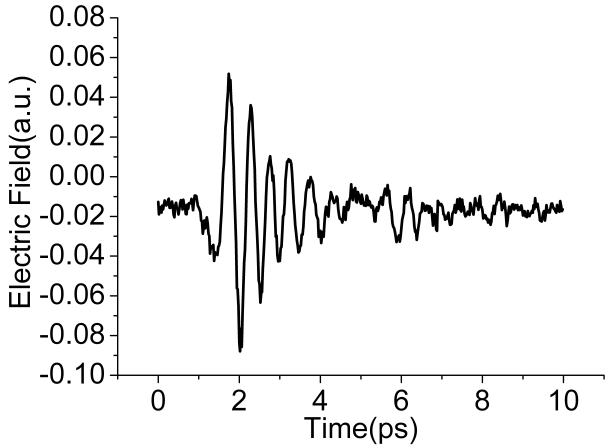


**Figure 3.9: Test result of Mira900** - The probe antenna excitation power is ~70 mW.

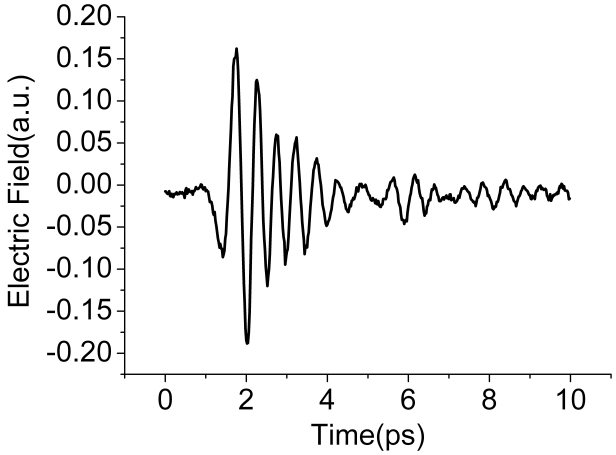


**Figure 3.10: Test result of Mira900** - The probe antenna excitation power is ~200 mW.

The test result of RegA9000 under ~220 mW probe power(maximum respect to the laser output) is shown in Fig.3.11, the scale is the same with Fig.3.9 and Fig.3.10. From the figures we find the SN ratio when using RegA9000 is about 20 times improved in comparison with Mira900, which is as large as $\sim 400:1$, the number is acceptable for the experiments.

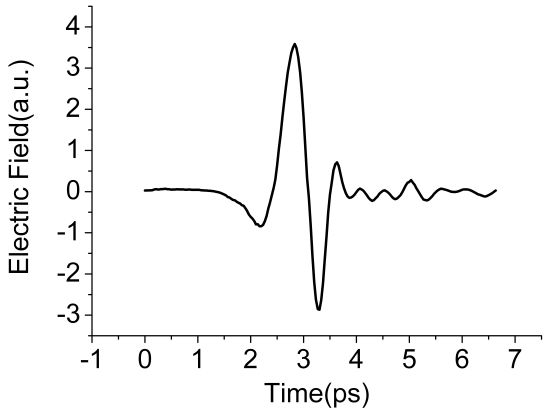


**Figure 3.11: Test result of RegA9000** - The probe antenna excitation power is ~220 mW.

At last, Hurricane was tested, because of the very strong pulse energy of Hurricane, in the setup, the 50:50 beam splitter was replaced by a 99:1 (pump:probe) beam sampler to avoid damaging the antenna. The test result of Hurricane is shown in Fig.3.12, the SN ratio is $\sim 1000:1$, which is the best number under the condition in the lab. So in all experiments including a PC antenna detection line in this thesis, Hurricane was chosen as the excitation laser.

Moreover, also using this test setup (Fig.3.8), we checked the performance of the antenna. We kept the THz beam and the probe beam to be focused on the same point in the antenna detection area (as shown in Fig.3.13), and we scanned the antenna with a translation stage. Principally, the antenna should only respond at the gap, however in our test experiments, we find no signal can be detected at the central gap position shown in the manual (Fig.3.1 and Fig.3.2), and at the position marked in Fig.3.13 (the red area), the detected THz signal can be detected. Moreover, in this marked area, the sensitivity of the antenna is shown in Fig.3.14, the size of the sensitive area is about 0.2 mm×0.8 mm. This result directly shows if we want to use this antenna in 2D scanning

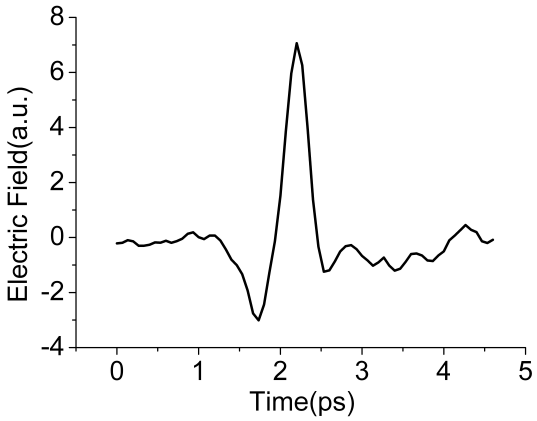


**Figure 3.12: Test result of Hurricane** - The probe antenna excitation power is ~5 mW.

setups, what the resolution of the scanning is (Fig.3.14). To improve the resolution of the antenna, we are planning to attach a pinhole on the antenna surface.

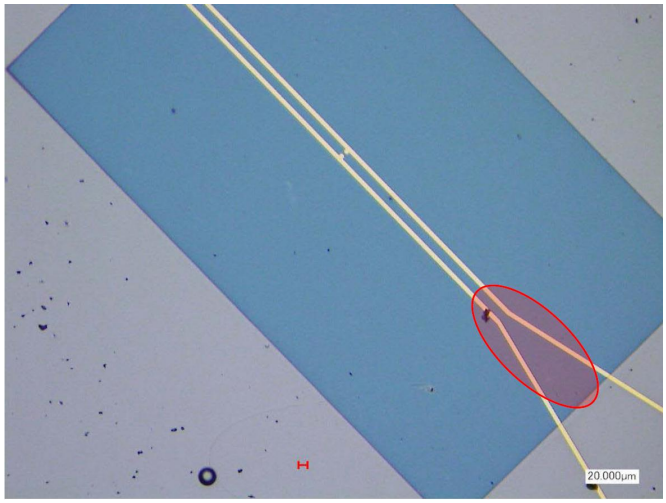


**Figure 3.13: A photo of antenna detection area** - captured by a CMOS camera with a telescope system, the red area indicates the antenna detection area in scanning.

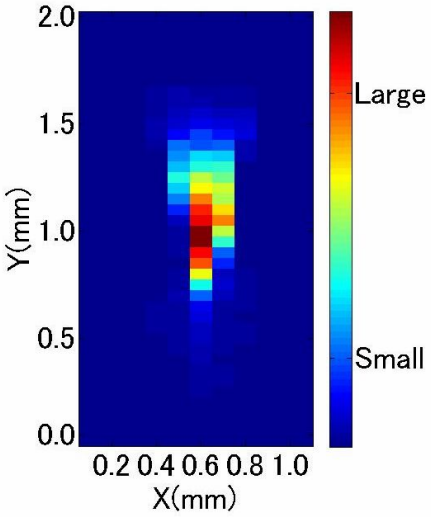


**Figure 3.14: Measured antenna resolution** - the central position coincides the red star in Fig.3.13.

## 3.3 Two-Dimensional Terehertz Time Domain Spectroscopy Setups

In order to analyze the spatial profiles of polarization distribution of vector beams, the THz-TDS systems should be improved to be able to scan in a plane to record the THz waveforms at different positions, we call these setups two-dimensional THz time domain spectroscopy (2D THz-TDS) systems.

We updated both free-space EO sampling lines and PC antenna lines to 2D THz-TDS systems. The 2D free-space EO line is shown in Fig.3.15 [53], the spatial distribution of the transversal electric field components is obtained by scanning the position of the probe beam near the focal point of the focused THz beams on the detection samples, which was achieved by changing the position of the iris/pinhole placed inside the expanded probe beam. Image of the iris/pinhole is formed on the EO crystal by the lens pair ("Lens" and "Tsurupica Lens" in Fig. 3.15), with 3/10 magnification. The spatial resolution of this setup depends on the image size of the iris/pinhole.

For PC antenna lines, it is easier to make a 2D scanning setup by only expanding the probe beam to cover a larger area. In our case, the detection resolution is as shown in Fig.3.14. So if we expand the probe beam, and set the antenna on a translation stage,

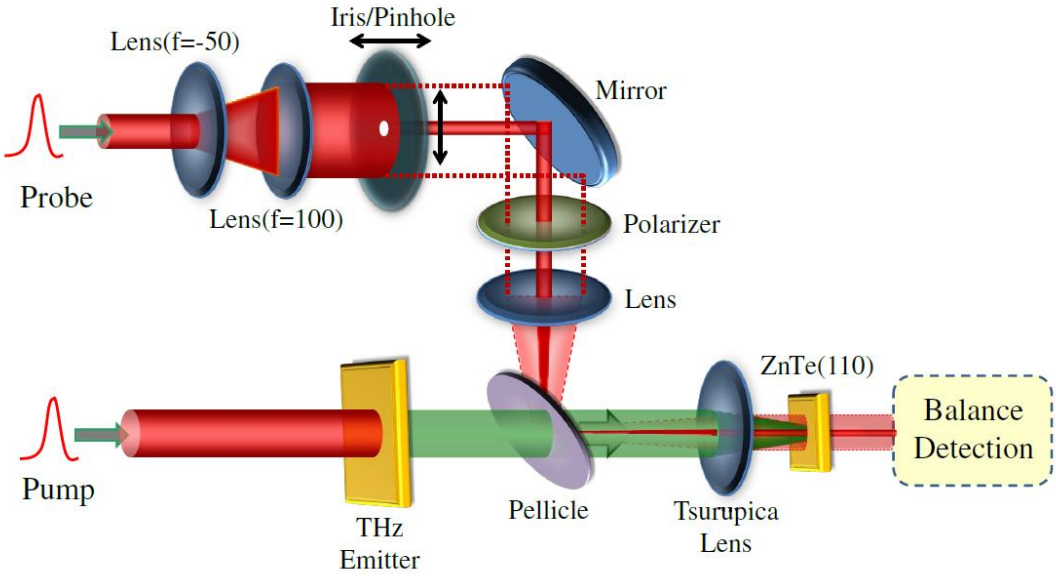


**Figure 3.15: 2D free-space EO sampling line** - Tsurupica lens transmits both THz and optical pulses, the resolution depends on the size of the iris/pinhole.

then the detection area of the antenna will be able to scan in the probe beam area, as shown in Fig.3.16 [78].

To check and optimize the 2D antenna scanning setup, we performed test experiments on a focused THz Gaussian beam, which is the simplest beam, in the test, we inserted a wire grid polarizer (WGP) to force the beam to be polarized along 45° orientation, with the antenna gap arranged in horizontal(x) and vertical(y) directions, two orthogonal components of the THz beam were recorded, and the intensity distribution is shown in Fig.3.17.

Moreover, the electric field vectors are plotted in Fig.3.18, from the figure, it is testified that the electric field is polarized along 45° orientation, so the reliability of the 2D PC antenna line is confirmed.

THz cameras were also introduced to record the intensity distributions of THz beams in the experiments, the details of the THz cameras can be found in ref.[79].

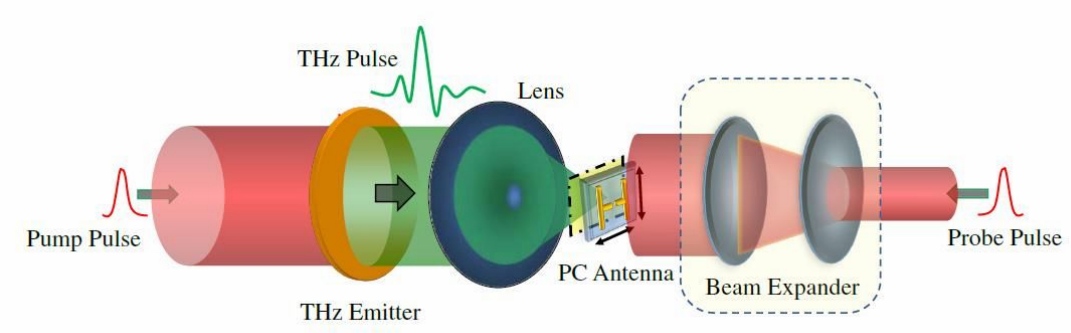


**Figure 3.16: 2D antenna scanning line** - The gap of the antenna is able to scan in the expanded probe area.

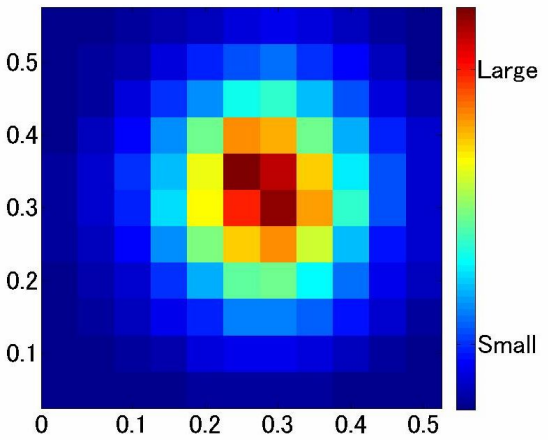


**Figure 3.17: Intensity distribution of a focused THz Gaussian beam** - The electric field is polarized in 45°, length scale: cm.

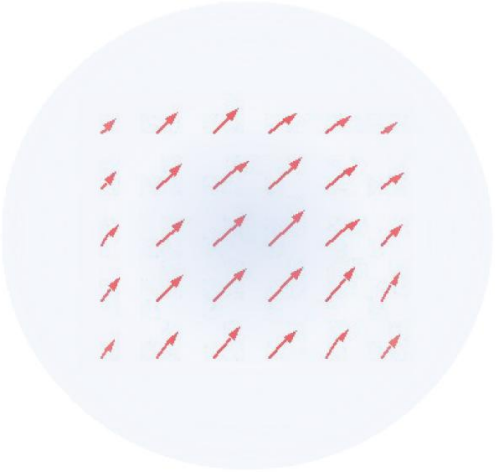

**Figure 3.18: Electric field vectors of a focused** 45° **polarized THz Gaussian beam** - The red arrows indicate the electric field vectors.

Chapter 4

# Introduction to Vector Beams

In this chapter, a brief introduction to vector beams, from concept, mathematical expressions, numerical methods, to experiments in the optical spectrum, will be given. It is attempted to build a informative background of vector beams, including theory, experiments and applications.

## 4.1 Mathematical Expressions of Cylindrical Vector Beams

The CV beams are vector-beam solutions of Maxwell's equations that obey axial symmetry in both amplitude and phase. By solving the scalar Helmholtz equation in the paraxial approximation, the spatial characteristics of optical beams in free space are commonly described by two familiar families of solutions: in rectangular coordinates $(x, y, z)$ the Hermite-Gauss modes, and in cylindrical coordinates $(\rho, \phi, z)$ the Laguerre-Gauss modes [80]. However considering the vector nature of light, it is the vector Helmholtz equation that describes the propagation of the electric field as a whole, whereas the scalar Helmholtz equation can only be used to describe the propagation of either a linearly polarized electromagnetic wave or a single Cartesian component of an arbitrary vector field, this means in the vector Helmholtz equation, the polarization features of optical beams are included. Actually, optical modes with spatial variant polarization are well known in waveguide theory, for example, $TM_{01}$ and $TE_{01}$ modes with radial and azimuthal electric vector orientation [18, 81].

At first, in free space, the typical paraxial beamlike solutions with harmonic temporal dependence are obtained by solving the scalar Helmholtz equation:

$$(\nabla^2 + k^2)E = 0. \tag{4.1}$$

In cylindrical coordinates, with $z$ to be the propagation axis, and with the electric field $E$ taken to be the harmonic temporal dependent form under paraxial approximation:

$$E = f(\rho, \phi, z)e^{i(kz-\omega t)}, \tag{4.2}$$

where $k$ and $\omega$ are the propagation constant and the (circular) frequency ($k = \omega/c$), respectively, the paraxial approximation appropriate for beams neglects $\partial^2 f/\partial z^2$ so that $f(\rho, \phi, z)$ is a solution of the scalar paraxial wave equation:

$$\frac{1}{\rho}\frac{\partial}{\partial \rho}\left(\rho\frac{\partial f}{\partial \rho}\right) + \frac{1}{\rho^2}\frac{\partial^2 f}{\partial \phi^2} + 2ik\frac{\partial f}{\partial z} = 0. \tag{4.3}$$

The elementary Gaussian solution is independent of $\phi$ and can be written as

$$f(\rho, z) = \frac{w_0}{w(z)}e^{-i\phi(z)}e^{(-\frac{\rho^2/w_0^2}{1+iz/L})}, \tag{4.4}$$

where $L = kw_0^2/2$ is the Rayleigh range, $w(z) = w_0[1 + (z/L)^2]^{1/2}$, and $\phi(z) = \tan^{-1}(z/L)$, $w_0$ is the waist parameter. The Gaussian envelope effectively localizes the field along directions transverse to the direction of propagation.

Also from eq.4.3, several higher modes can be realized, one example is Laguerre-Gauss solution $LG_{pl}$, the mathematical expression is shown as:

$$f(\rho, \phi, z) = E_0\left(\sqrt{2}\frac{\rho}{w}\right)^l L_p^l\left(2\frac{\rho^2}{w^2}\right)\frac{w_0}{w(z)}e^{-i\phi_{pl}(z)}e^{(-\frac{\rho^2/w_0^2}{1+iz/L})}e^{il\phi}, \tag{4.5}$$

where $L_p^l(x)$ is the associated Laguerre polynomials that satisfy the differential equation:

$$x\frac{d^2L_p^l}{dx^2} - (l + 1 - x)\frac{dL_p^l}{dx} + pL_p^l = 0, \tag{4.6}$$

and $\phi_{pl}(z) = (2p + l + 1)\tan^{-1}(z/L)$ is the Gouy phase shift. For $l = p = 0$, the solution degenerates to the fundamental Gaussian beam solution. For $l \neq 0$, the LG mode has a vortex phase term $e^{il\phi}$, which is related to orbital angular momentum of light [82].

Another example of solution of eq.4.3 is so-called Bessel-Guass beam solution, the solutions take the general form [83]:

$$f(\rho, z) = E_0 \frac{w_0}{w(z)} e^{-i\phi(z)} J_0\left(\frac{\beta\rho}{1 + iz/L}\right) e^{\left(-\frac{\beta^2 z/(2k)}{1+iz/L}\right)}, \tag{4.7}$$

where $\beta$ is a constant scale parameter, $\phi(z)$ is the Gouy phase shift, and $J_0(x)$ is the zeroth-order Bessel function of the first kind. When $\beta = 0$, the solution reduces to the fundamental Gaussian beam solution.

It should be noted, the solutions shown above are the paraxial beamlike solutions to the scalar Helmholtz equation (eq.4.1), in which the SoPs are assumed to be spatially homogeneous, these solutions are called scalar beams. For scalar beams, the electric field vector on the cross section (i.e., SoP) is independent of the location of observation points. Hereon, if we consider the full vector wave equation for the electric field:

$$\nabla \times \nabla \times \mathbf{E} - k^2 \mathbf{E} = 0, \tag{4.8}$$

where an $e^{-i\omega t}$ time dependence is assumed and $k = \omega/c$. Consider a circularly symmetric, azimuthally polarized ($\phi$-polarized) field, for which ($E$) takes the form:

$$\mathbf{E}(\rho, z) = \vec{e_\phi} F(\rho, z) e^{i(kz - \omega t)}, \tag{4.9}$$

substituting eq.4.9 into eq.4.8 and making the paraxial approximation, we can obtain the single, scalar equation:

$$\frac{1}{\rho}\frac{\partial}{\partial\rho}\left(\rho\frac{\partial F}{\partial\rho}\right) - \frac{F}{\rho_2} + 2ik\frac{\partial F}{\partial z} = 0. \tag{4.10}$$

There is a clear difference in the second terms of eq.4.3 and eq.4.10 for azimuthal symmetry, and the trial solution of eq.4.10 can be written as:

$$F(\rho, z) = E_0 J_1\left(\frac{\beta\rho}{1 + iz/L}\right) e^{\frac{i\beta^2 z/(2k)}{1+iz/L}} f(\rho, z), \tag{4.11}$$

where $f(\rho, z)$ is the elementary Gaussian solution defined in eq.4.4, L is the Rayleigh range defined below eq.4.4, $J_1$ is the first kind Bessel function of order one. This solution corresponds to an azimuthally polarized vector Bessel-Gaussian beam. Due

to the reciprocity between electric component and magnetic component, there should exist a transverse magnetic field solution:

$$\mathbf{H}(\rho, z) = -H_0 J_1\left(\frac{\beta\rho}{1+iz/L}\right) e^{\frac{i\beta^2 z/(2k)}{1+iz/L}} f(\rho, z) e^{i(kz-\omega t)} \vec{e_\phi}. \tag{4.12}$$

For this azimuthal magnetic field solution, the corresponding electric vector in the transverse plane aligns in the radial direction, hence eq.4.12 represents the radial electric polarization state.

If the parameter $\beta$ in the Bessel function is very small, this condition holds true for many applications, instead of the vector Bessel-Gaussian solutions above, always simplified expressions are used. For vector beams with large cross sections, the vector Bessel-Gaussian beam at the beam waist can be approximated as:

$$\mathbf{E}(\rho, z) = A \cdot \rho \cdot e^{-\rho^2/w^2} \hat{e}_i, \quad i = \rho, \phi. \tag{4.13}$$

The amplitude profile of eq.4.13 is exactly the $LG_{01}$ mode, but without the phase vortex $e^{i\phi}$. The spatial amplitude distribution and electric field vector orientation in the cross section of radial and azimuthal mode can be found in Fig.4.1 [4].

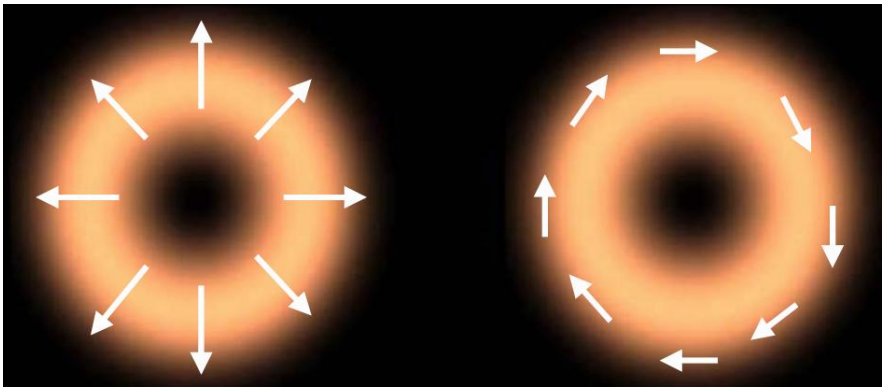

**Figure 4.1: The spatial amplitude distribution and electric field vector orientation in the cross sections of radial and azimuthal modes** - left: radial beam; right: azimuthal beam [4].

## 4.2 Focal Properties of Vector Beams

Because of novel inhomogeneous SoPs in the cross section of vector beams, the focal features of vector beams are special. One example is, as shown in Fig.4.2, under tight focusing, in the focal volume of radially polarized beams, the geometry of the electric field implies the in-plane electric components will be canceled out due to the cylindrical symmetry, while a large longitudinal (z-polarized) electric component ($E_z$) survives. Also this property holds true for magnetic field in the focal volume of azimuthally polarized beams under tight focusing, because of the reciprocity between electric field of radial modes and magnetic field of azimuthal modes, in the focal volume of azimuthal beams, there will be a large $H_z$ component.

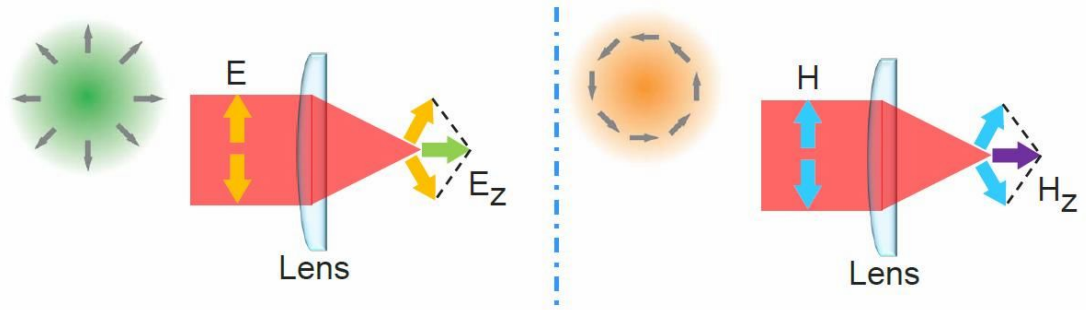


**Figure 4.2: Focused radial and azimuthal beams** - left: $E_z$ in a radial beam; right: $H_z$ in an azimuthal beam.

Based on the modulation of SoPs, vector beams exhibit great potential to manipulate the electromagnetic field in the focus. To sufficiently realize this potential, a theoretical tool to analyze the focal features of vector beams is urgent. In this section, a vector theory of diffraction, invented by B. Richards and E. Wolf in 1959 [31], will be introduced. Several examples about the special focal features of vector beams will be shown.

### 4.2.1 The Vector Theory of Diffraction : Richard-Wolf Integration

The content in this part is following ref.[84], to rewrite the Richard-Wolf Integration [31] to a Fourier transform, then Fast Fourier Transform (FFT) algorithm can be used to calculate the focal field of arbitrarily polarized beams. In comparison with directly performing the integration, this method is much faster.

The basic optical layout and the respective coordinate systems are shown in Fig.4.3 [84].

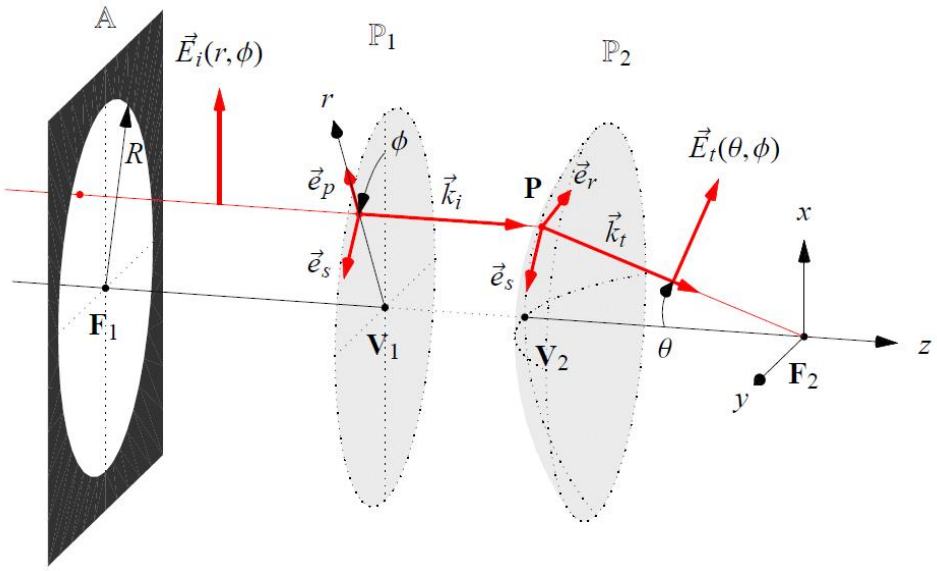


**Figure 4.3: Optical setup** - The objective is represented by the aperture stop $\mathbb{A}$ with radius $R$, the principal planes $\mathbb{P}_1$ and $\mathbb{P}_2$ with vertex points $\mathbf{V}_1$ and $\mathbf{V}_2$, and the foci $\mathbf{F}_1$ and $\mathbf{F}_2$. The focal length $f$ is given as $f = \overline{\mathbf{F}_2\mathbf{V}_2}$. The point $\mathbf{P}$ is the intersection point of a ray with $\mathbb{P}_2$ and shows the relation of the position r at $\mathbb{P}_1$ of the incident wave $\vec{E}_i$ to the propagation angle $\theta$ at $\mathbb{P}_2$ of the transmitted wave $\vec{E}_t$. [84]

From the ray geometry in the figure (red arrows in Fig.4.3), when a coherent and monochromatic ray parallel to the optical axis passing through the aperture stop $\mathbb{A}$, and is transferred to the output plane $\mathbb{P}_2$ from the input plane $\mathbb{P}_1$, $\mathbb{P}_1$ is a spherical surface, which is centered at the focal point $\mathbf{F}_2$. Any ray go through the point $\mathbf{P}$ on $\mathbb{P}_2$ will finally arrive at $\mathbf{F}_2$, then the deflection angle $\theta$ of $\mathbf{P}$ is defined as:

$$\sin\theta = \frac{r}{R}\frac{NA}{n_t}, \tag{4.14}$$

where $r$ is the off-axis coordinate of $\mathbf{P}$, $R$ the aperture stop radius, $NA$ is the numerical aperture of the objective and $n_t$ the refractive index behind the $\mathbb{P}_2$ surface.

The incident field $\vec{E}_i$ at $\mathbb{P}_1$ is decomposed into two orthogonal components (p- and s- polarized), then the unit vectors for p- and s-polarization are:

$$\vec{e_p} = \begin{pmatrix} \cos\phi \\ \sin\phi \\ 0 \end{pmatrix} \quad \text{and} \quad \tilde{e}_s = \begin{pmatrix} -\sin\phi \\ \cos\phi \\ 0 \end{pmatrix}, \tag{4.15}$$

where $\phi$ is the azimuth angle. A ray goes cross surface $\mathbb{P}_1$ to surface $\mathbb{P}_2$ suffers from a $\theta$ deflection, the unit vector transmission between these two principle planes ($\vec{e_p}$ and $\vec{e_r}$) is shown as:

$$\vec{e_r} = \begin{pmatrix} \cos\phi\cos\theta \\ \sin\phi\cos\theta \\ \sin\theta \end{pmatrix}. \tag{4.16}$$

From here we mark the transmitted electric field at $\mathbb{P}_2$ to be $\vec{E}_t(\theta, \phi)$, under the Debye approximation [85], as shown in Fig.4.4, that when considering any point $P'(x, y, z)$ in the focal volume (near the focal point), the distance between $P'$ and a point $Q'$ on the principle plane is $s$, the geometrical relation can be approximately expressed as:

$$s - f = -\mathbf{q} \cdot \mathbf{R}', \tag{4.17}$$

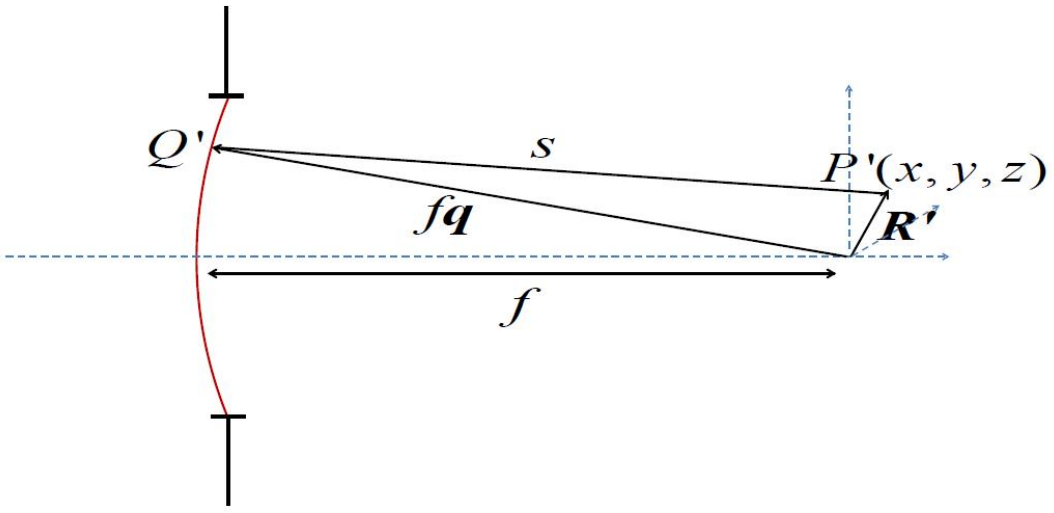


**Figure 4.4: Debye approximation** - under this approximation, $s - f = -\mathbf{q} \cdot \mathbf{R}'$.

and from Huygens-Fresnel's equation, at $P'(x, y, z)$, the local electric field $\vec{E}(x, y, z)$ can be written as:

$$\vec{E}(x, y, z) = -\frac{i}{\lambda_0}\frac{e^{-ikf}}{f}\iint \vec{E}_t(\theta, \phi)e^{iks}dS, \tag{4.18}$$

where $dS$ is the surface element on the principle plane, and can be written as:

$$dS = f^2 d\Omega, \tag{4.19}$$

where $d\Omega$ represents the unit solid angle that $dS$ opens to the focal point, then by substituting eq.4.17 and eq.4.19 into eq.4.18, at any point $(x, y, z)$ in a small sphere near the focal point $\mathbf{F}_2$, the local electric field $\vec{E}(x, y, z)$ can be obtained by integrating $\vec{E}_t(\theta, \phi)$ on the surface $\mathbb{P}_2$ which contributes to it, the equation is shown as:

$$\vec{E}(x, y, z) = -\frac{if}{\lambda_0}\iint_{\Omega} \vec{E}_t(\theta, \phi)e^{i(k_z z - k_x x - k_y y)}d\Omega, \tag{4.20}$$

where $f$ is the focal length of the lens, and $\lambda_0$ is the wavelength. The phase factor $e^{ik_z z}$ accounts for the phase accumulation when propagating along the z-axis, whereas the term $e^{-i(k_x x + k_y y)}$ represents the phase difference of the wave front at off-axis points $(x, y, z)$ with respect to the on-axis point $(0, 0, z)$.

In this integration, in spherically spatial coordinate, $d\Omega$ can be written as $d\Omega = \sin\theta d\theta d\phi$, and the integration become:

$$\vec{E}(x, y, z) = -\frac{if}{\lambda_0}\int_0^{\Theta} \sin\theta \int_o^{2\pi} \vec{E}_t(\theta, \phi)e^{i(k_z z - k_x x - k_y y)}d\phi d\theta, \tag{4.21}$$

this integration extends over the principle surface $\mathbb{P}_2$, i.e. $\sin\Theta = NA/n_t$. And the wave vector $\vec{k}_t$ is given in spherical coordinates $\theta$ and $\phi$ by:

$$\vec{k}_t(\theta, \phi) = k_0 n_t \begin{pmatrix} -\cos\phi\sin\theta \\ -\sin\phi\sin\theta \\ \cos\theta \end{pmatrix} \quad \text{where} \quad \mathrm{k}_0 = \frac{2\pi}{\lambda_0}. \tag{4.22}$$

Another way to evaluate this integration is to rewrite the integration step $d\Omega$ in the plane wave spectrum domain, then the integration will be performed over the surface $\mathbb{P}_1$ instead of $\mathbb{P}_2$. Directly from eq.4.14 and eq.4.22, the integration step $d\Omega$ for a sampling over $\mathbb{P}_2$ can be projected onto $\mathbb{P}_1$, and shown as:

$$d\Omega = \left(\frac{NA}{Rn_t}\right)^2 \frac{rdrd\phi}{\cos\theta} = \left(\frac{NA}{Rn_t}\right)^2 \frac{dxdy}{\cos\theta} = \frac{1}{k_t^2}\frac{dk_x dk_y}{\cos\theta}. \tag{4.23}$$

Substituting this sampling step into eq.4.20 yields:

$$\vec{E}(x,y,z) = -\frac{if}{\lambda_0 k_t^2}\iint_{r<R}(\vec{E}_t(\theta,\phi)e^{i(k_z z)}/\cos\theta)e^{-i(k_x x+k_y y)}dk_x dk_y. \tag{4.24}$$

It should be noted in the plane $\mathbb{P}_1$, when $r > R$, because of the aperture stop, $|\vec{E}_t| = 0$, these points have no contribution to the integration, then eq.4.24 can be extend to the whole plane wave spectrum domain $(k_x, k_y) \in \mathbb{R}^2$, so the integration can be written as a Fourier transform:

$$\vec{E}(x,y,z) = -\frac{if}{\lambda_0 k_t^2}\mathcal{F}[\vec{E}_t(\theta,\phi)e^{ik_z z}/\cos\theta]. \tag{4.25}$$

The Richards-Wolf integration is now expressed as a Fourier transform of the field distribution in the aperture $\mathbb{A}$. In eq.4.25, the term $\vec{E}_t(\theta,\phi)$ representing the field distribution in the aperture $\mathbb{A}$ can be arbitrarily set, including amplitude, phase and polarization information. For example, for x-polarized incident field and radially polarized (r-polarized) incident field with homogeneous amplitude and phase front, the component expressions in Cartesian coordinate system of $\vec{E}_t(\theta,\phi)$ can be written as [30, 31]:

$$\vec{E}_t(x\text{-polarized}) = \begin{pmatrix} \cos\theta + (1-\cos\theta)\sin\phi^2\sqrt{\cos\theta} \\ (\cos\theta - 1)\sin\phi\cos\phi\sqrt{\cos\theta} \\ i\cdot\cos\phi\sin\theta\sqrt{\cos\theta} \end{pmatrix}$$

$$\text{and} \qquad , \tag{4.26}$$

$$\vec{E}_t(r\text{-polarized}) = \begin{pmatrix} \cos\theta\cos\phi\sqrt{\cos\theta} \\ \cos\theta\sin\phi\sqrt{\cos\theta} \\ i\cdot\sin\theta\sqrt{\cos\theta} \end{pmatrix}$$

where the term $\sqrt{\cos\theta}$ accounts for energy conservation before and after the focusing lens [31], while the other terms represent geometrical transformation factors from the entrance pupil $\mathbb{A}$ to the exit pupil $\mathbb{P}_2$.

### 4.2.2 The Focal Features of Vector Beams

With the FFT based numerical method, the focal features of arbitrary beams can be analyzed, directly from eq.4.25 and eq.4.26, the examples of linearly and radially polarized beams are shown as Fig.4.5 and Fig.4.6.

For linear input field, the amplitude distributions of electric component $E_x, E_y$ and $E_z$ in the focal plane ($x$-$y$ plane), and in a plane including the optical axis ($x$-$z$ plane), in Cartesian coordinate system, are shown as Fig.4.5.

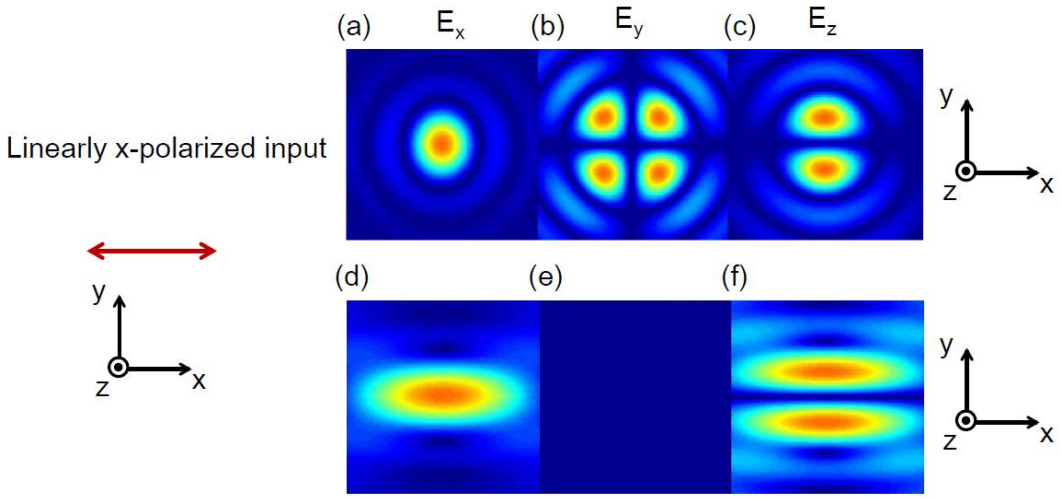


**Figure 4.5: Amplitude distributions of $E_x, E_y, E_z$ of a linear focused beam** - upper: the focal plane($x$-$y$ plane), lower: a plane including the optical axis($x$-$z$ plane) ; from left to right: $E_x, E_y, E_z$.

For radial input field, it is convenient to use cylindrical coordinate system, due to the radial geometry, the component $E_\phi$ in the focal volume is always zero, and the amplitude distributions of $E_\rho$ and $E_z$ are shown as Fig.4.6. It is clear that the in-plane electric component of radial focused beams is a donut mode.

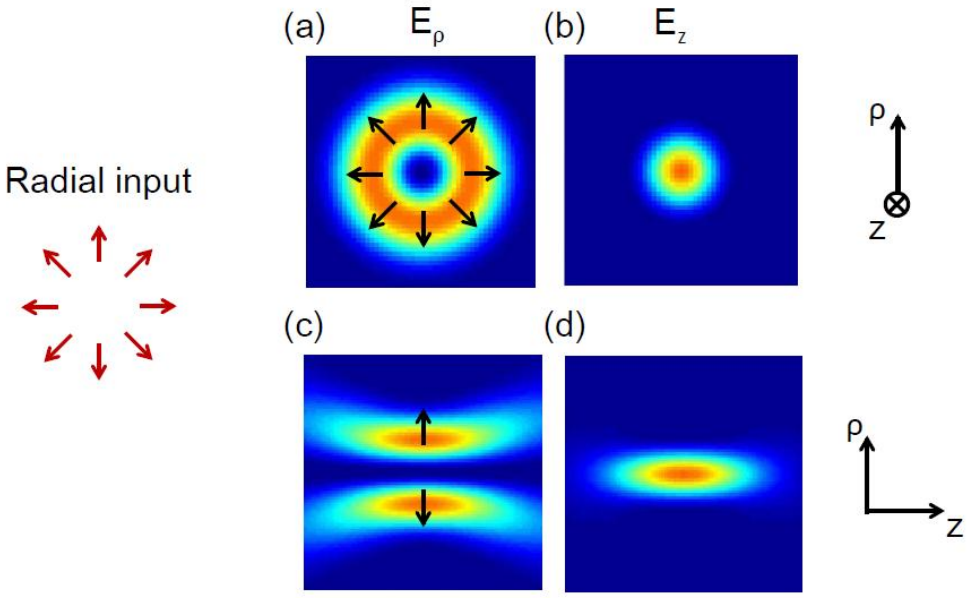


**Figure 4.6: Amplitude distributions of $E_\rho$ and $E_z$ of a radial focused beam** - left: $E_\rho$, right: $E_z$; upper: the focal plane ($\rho$-$\phi$ plane), lower: a plane including the optical axis ($\rho$-$z$ plane).

For azimuthal input field, in the focal volume, the components $E_\rho, E_z \equiv 0$, the amplitude distribution of $E_\phi$ is shown as Fig.4.7 [30]:

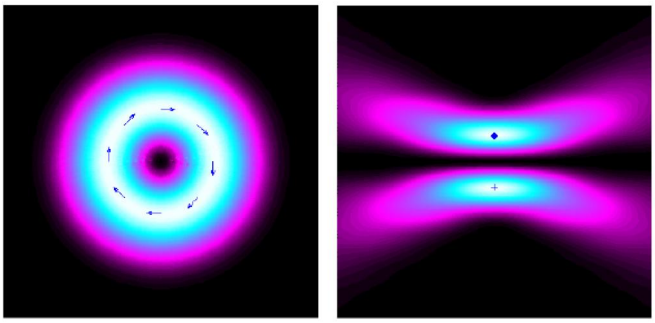

**Figure 4.7: Amplitude distributions of $E_\phi$ of an azimuthal focused beam** - left: the focal plane ($\rho$-$\phi$ plane), right: a plane including the optical axis ($\rho$-$z$ plane) [30].

Because of the unique SoPs of vector beams, the focal properties of vector beams are special. For radially polarized beams, it has been proved when they are tightly focused, the longitudinal polarized $E_z$ component will be dominant, and the focal spot size is smaller than linearly polarized beams [1, 86], it means the sharper focal spot of radially polarized beams breaks the diffraction limit defined by Abbe's Formula: $d = \frac{\lambda}{2NA}$, where $\lambda$ is the wavelength of the illumination, and the numerical aperture(NA) of the lens is defined by $NA = n \cdot \sin\theta$, where $\theta$ is defined as shown in Fig.4.8, and $n$ is the refraction index of the material in the focal space.

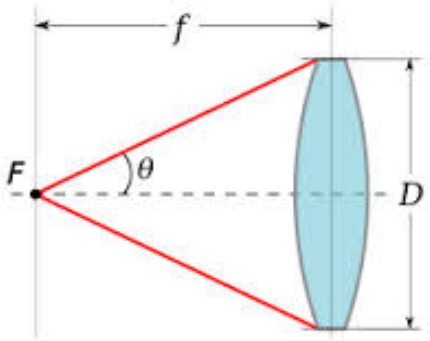


**Figure 4.8: The definition of NA** - $NA = n \cdot \sin\theta$, $n$ is the refraction index of the material where $F$ is in.

In Fig.4.9 reprinted from ref.[1, 86], the focal spot sizes of linearly polarized beams and radially polarized beams are compared, the sharper focus of radial beams is

confirmed.

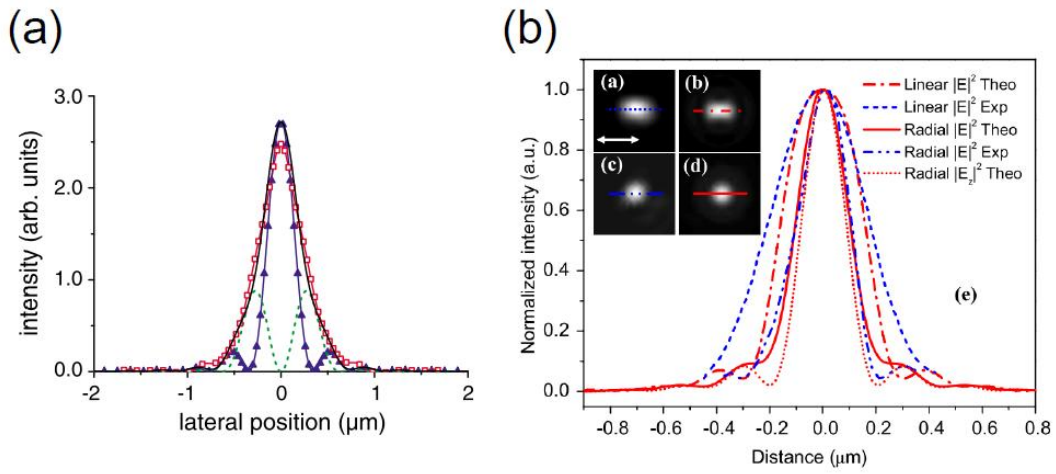


**Figure 4.9: The sharper focus of radial beams** - (a) blue: radial beams, red: linear beams [1, 86].

Moreover, with carefully trimming SoPs and phase distribution of vector beams, 3D designing of focal spot is possible. For example, as shown in Fig.4.10, the authors proposed a ultra-long longitudinal polarized focusing field with radially polarized Bessel-Gaussian beams and a binary phase element, which is named "optical needle" [33]. Another example is, with tailoring a mix mode of radially and azimuthally polarized beams, three-dimensional orientation-unlimited polarization encryption was realized [87], as shown in Fig.4.11.

More examples of focal engineering, e.g., optical chain [88], optical bubble [89] and others [90–92] associated with vector beams are also reported.

Because of the distinguished focal features of vector beams, they have great application potential in many areas, e.g., micro-structuring [35], optical tweezers [93], high resolution microscopic [94], plasmonics and near field optics [95–97], etc..

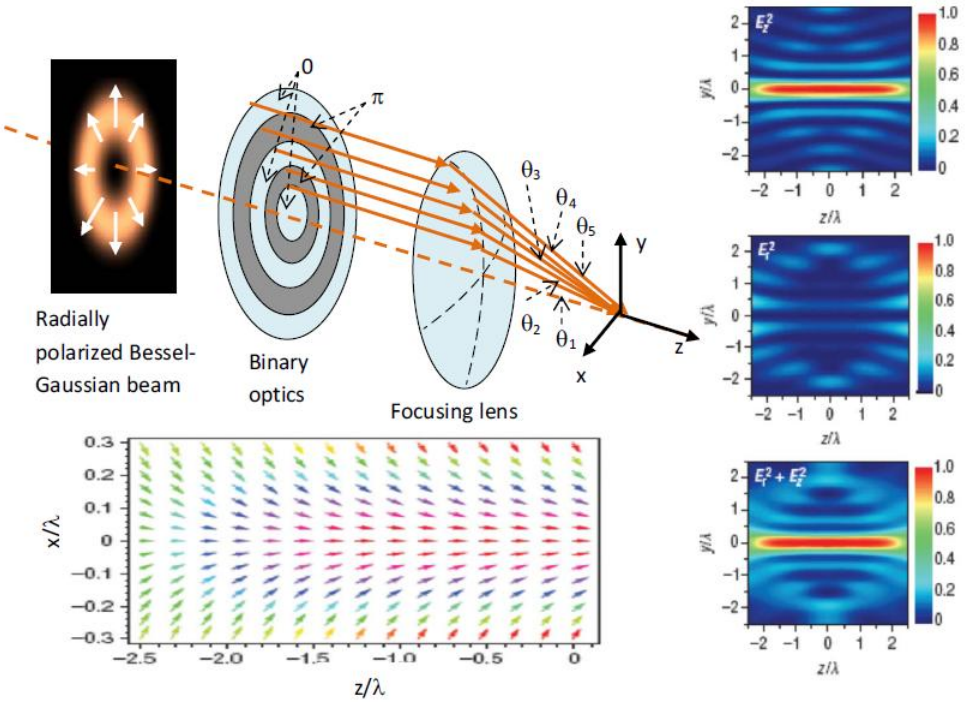


**Figure 4.10: Optical needle** - an optical needle created with radially polarized Bessel-Gaussian beams [33].

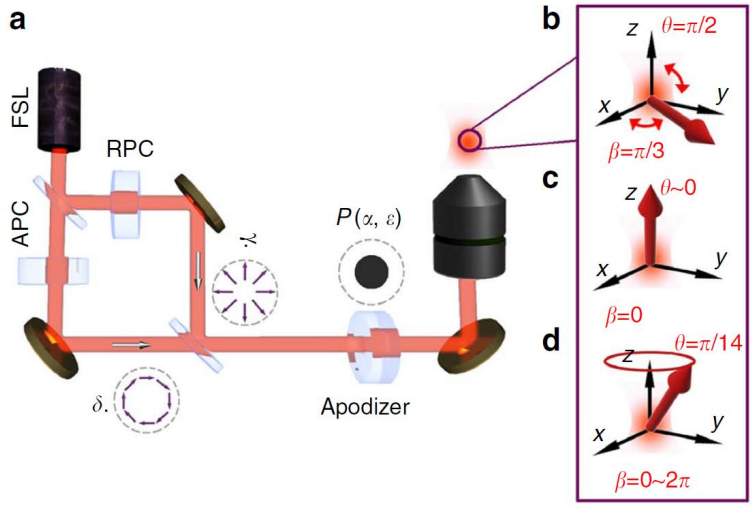


**Figure 4.11: 3D polarization manipulation** - three-dimensional orientation-unlimited polarization encryption [87].

## 4.3 Generation Schemes of Vector Beams in the Optical Spectrum

Driven by the application potential of vector beams, in the past decade, plenty of methods were invented to generate vector beams in the optical spectrum, including active methods that directly force the laser oscillate in vector modes with adding intra-cavity elements, and passive methods that convert the free-propagating laser beams to vector beams. In this section, several examples of optical vector beam generation will be shown for the convenience to discuss the generation schemes of vector beams in the THz spectral range in Chapter 5.

**Generation of a radially polarized laser beam by use of a conical Brewster prism**

As reported in ref.[98], with adding a conical Brewster prism in a Nd:YAG laser cavity, as shown in Fig.4.12, then on the surface of the conical prism, only radially polarized light survives, while azimuthally polarized light suffers from great loss. Considering the axial symmetry of the prism, thus the laser oscillates in the radial mode, the results can be found in Fig.4.13.

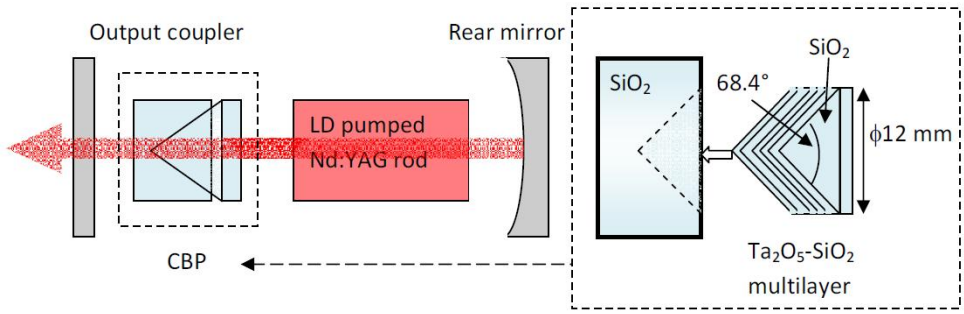


**Figure 4.12: Nd:YAG laser that generates CV beams by using axial dichroism created by a conical Brewster prism** - the structure of the conical Brewster prism is shown to the right [98].

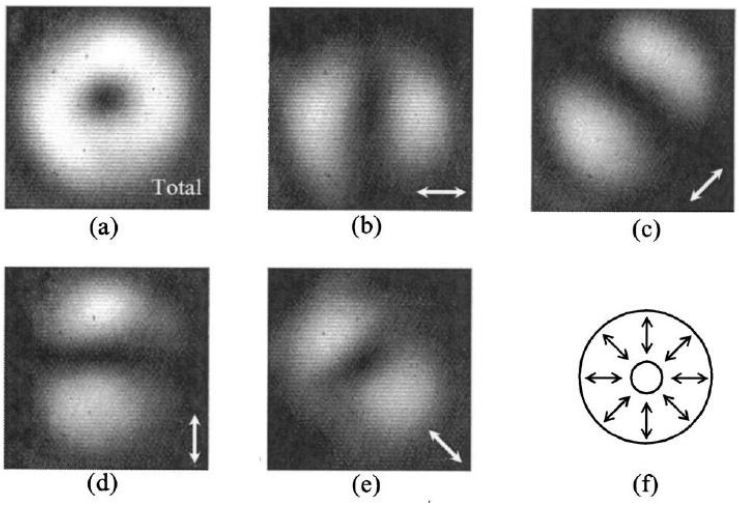


**Figure 4.13: Intensity distribution of the output mode** - (a) total intensity distribution of the laser beam, (b)-(e)intensity distributions after the linear polarizer for the directions indicated by the arrows, (f) schematic representation of the polarization distribution [98].

### Generation of vector beams with segmented half-waveplate mode converters

A segmented half-waveplate(HWP) was used to converter linearly polarized laser beams to radial or azimuthal modes [99], the segmented HWP was made by gluing together eight sectors of segmented $\lambda/2$ plates with different discrete fast axis [1], the fast axis orientations are shown as Fig.4.14, then with linearly polarized laser beams in vertical or horizontal direction passing through this element, after it, radially or azimuthally polarized beams can be realized. Because of discontinuous feature of the segmented converter, the vector modes generated from this method are not ideal vector modes. The mode overlap between these quasi-vector modes and ideal vector modes are evaluated to be $\sim$ 93% [99]. To further clean up the mode, a near-confocal Fabry-Perot interferometer can be used to filter out the undesired modes and keep the radially polarized component [1].

[1]In fact, in ref.[99], 4-piece and 8-piece segmented wave-plates were made, and from theoretical predictions, the purity of vector modes from a 4-piece element is evaluated to be $\sim$ 75%, the number is far lower than in the case of using a 8-piece element, which is $\sim$ 93%.

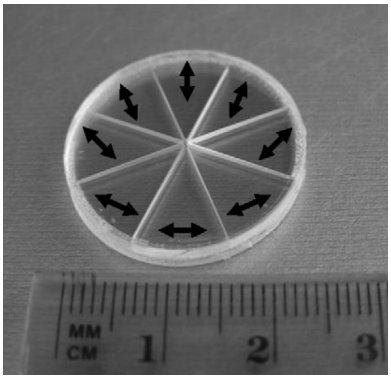


**Figure 4.14: Segmented spatially variant $\lambda/2$ plates that can convert linear polarization into vector polarization** - the arrows indicating the local orientation of the fast axis [99].

### Vector beams generated by space-variant dielectric sub-wavelength gratings

When the period of the grating is smaller than the incident wavelength, only the zeroth order is a propagating order, and such gratings behave as layers of a uniaxial crystal with the optical axes perpendicular and parallel to the grating grooves. By controlling the depth of the grating, the effective birefringence can be manipulated, any desired wave-plates can be realized with this method. In ref.[100], the authors fabricated a continuously spatial-variant $\lambda/4$ plate, with this element, the left or right circularly polarized laser beams passing through it will be transferred to azimuthally or radially polarized beams, as shown in Fig.4.15.

### Generation of arbitrary vector beams with a spatial light modulator and a common path interferometric arrangement

With a common path interferometric arrangement, and a holographic pattern loaded by a spatial light modulator(SLM), arbitrary vector beams can be experimentally realized [101], the experimentally setup is shown in Fig.4.16.

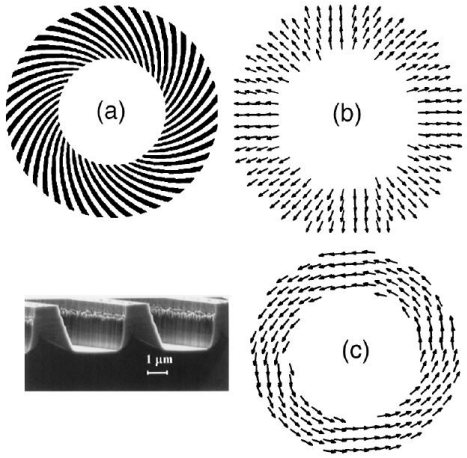


**Figure 4.15: Spatial-variant sub-wavelength grating for vector beams generation** - (a) geometry of the space-variant grating as well as an image of a typical grating profile taken with a scanning-electron microscope. The polarization of the beams when the incident polarization is (b) right-hand circular and (c) left-hand circular are also shown [100].

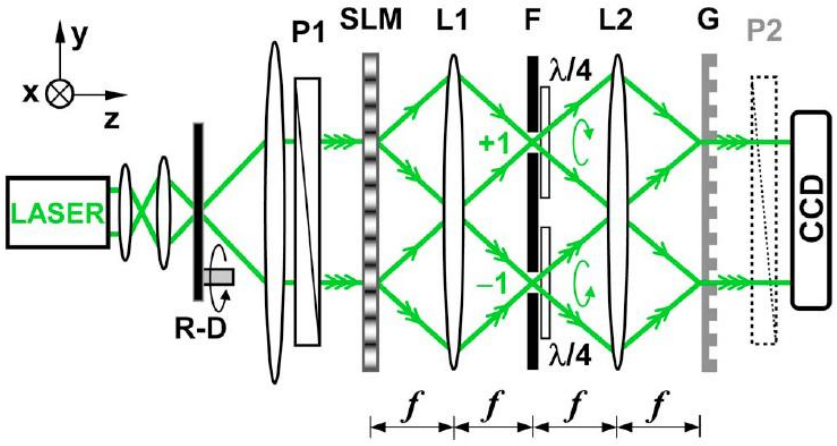


**Figure 4.16: A common-path interferometer setup implemented with a SLM to generate arbitrary vector beams.** - [101]

Chapter 5

# Generation and Characterization of Broadband Terahertz Vector Beams

As introduced in Chapter 4, due to the intriguing properties of vector beams, transplanting this concept to the THz spectral range will be an exciting topic, the generation and applications of "THz vector beams" will exert significant impacts to THz techniques. The realization of THz vector beams will be beneficial for both boosting the THz researches and understanding the nature of vector beams. On one hand, vector beams have great potential in many THz applications, e.g. THz waveguiding [51, 102], THz plasmonics [103, 104], THz near-field optics [105, 106], THz high resolution microscopy, etc.; on the other hand, the THz time-domain spectroscopy technique introduces the possibility to record entire features of vector beams, including amplitude, phase and polarization information. As a result, in the THz region, it is possible to directly measure the longitudinal electric component, and directly observe the physical phenomena related to phase features, such as the Gouy phase shift [107] of vector beams; while in the optical spectrum, it is difficult to directly record the longitudinal electric component and the phase features. Such experiments offering direct evidences of novel vector beam properties, will deepen the understanding of the physical nature of vector beams.

Till now, researches on THz vector beams are limited: the generation of broadband[1] THz vector beams is still a topic waiting for explorations; while the characterization of THz vector beams is not sufficiently realized. In this chapter, the reported generation schemes of THz vector beams will be summarized, and the drawbacks of these

[1] In presented methods, as will be introduced in this Chapter, the bandwidth is typically under 0.5 THz.

methods will be discussed. Then employing nonlinear crystals possessing 3-fold rotational symmetry, two new methods to generate broadband THz vector beams will be introduced. Moreover, with THz cameras and 2D THz-TDS setups, the complete focal features of THz vector beams are characterized, including the features of in-plane electric components, and longitudinal electric/magnetic components in the focal volume of radially and azimuthally polarized THz beams.

## 5.1 Reported Generation Schemes of Terahertz Vector Beams

Because the THz gap is quite different from the optical frequency region, it is impossible to transplant the generation methods of vector beams in the optical range directly to the THz range. For instance, considering the methods introduced in Chapter 4, the first example is adding mode selection elements in laser cavities to force the lasers oscillate in vector modes, this method does not work in the THz band, because there is no THz pulse lasers; another example, mode converters that transfer the linearly or circularly polarized beams to vector beams, e.g., segmented half wave-plates, continuous dielectric sub-wavelength gratings, the problem of these elements is they have a narrow working bandwidth, thus not fit for the broad THz band [1]; the last example is generating optical vector beams with a spatial light modulator (SLM) and a common path interferometric arrangement, however, SLMs are only available in the visible and near-infrared spectra, in the THz range, there is no SLMs available till now.

In the THz spectral range, the generation methods of vector beams are not sufficiently investigated, the reported methods rely on axial symmetry of the THz emission mediums, mode conversion systems transforming linear polarization to radial polarization, or axial symmetrical PC antennas. These methods suffer from several disadvantages. In this section, these methods and their drawbacks will be summarized.

#### Generation of THz radial beams from Cherenkov-type radiation

It has been reported, with fs laser filaments in air [46], or with ZnTe(001) crystals [49], because of the axial symmetry of the THz emission scheme (Cherenkov conic

[1] Recently in Gonokami Group, using segmented stacked broadband $\lambda/4$ THz wave-plates, THz vector beams are successfully generated, the spectral range covers 0.2-2 THz.

shock wave), the generated THz beams will be radially polarized in the forward direction, as shown in Fig.5.1 and Fig.5.2.

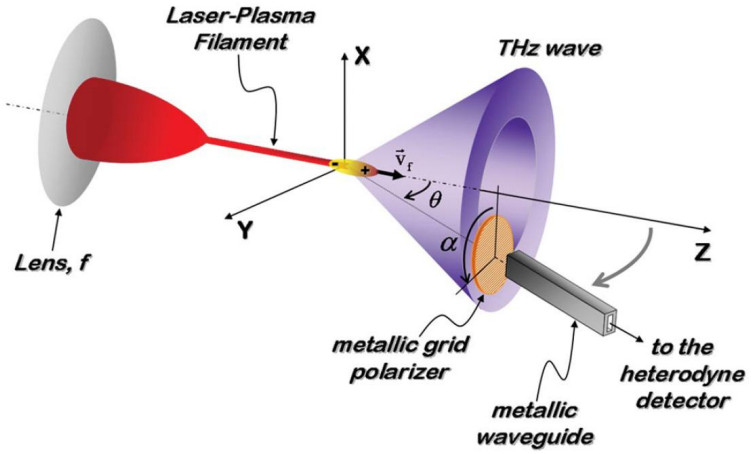


**Figure 5.1: Conical forward THz emission from fs-laser-beam filament in air** - the axial symmetry of the system induces the radial polarization of THz emission [46].

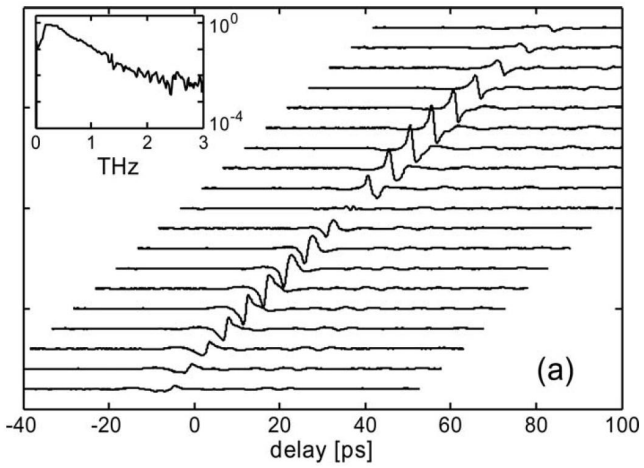


**Figure 5.2: Radially polarized THz beam from a (001)-cut ZnTe crystal** - THz single-cycle waveforms obtained by translating the THz receiver to scan the THz beam profiles [49].

However, the underlying physical mechanism of laser filaments is ambiguous, also the radially polarized THz beams generated from laser filaments are found to be not perfect radial modes, local ellipticity has been observed [47, 48]. Moreover, to realize laser filaments, a quite powerful fs laser is necessary in the experiments; while

for ZnTe(001), the THz emission is rather weak, which may restrict the applications of these methods. In these methods, azimuthally polarized THz beams can not be realized.

**A passive linear-to-radial mode conversion system [45]**

It is well known that, in metallic hollow core waveguides, the supported waveguide modes depend on the diameter of the waveguides, as shown in Fig.5.3, the modes survive only when the inner diameter of the waveguides is larger than the cutoff diameter. The first four modes supported by a hollow core waveguide are shown in Fig.5.4, from the figure, it is clear following in wavelength, scale after the linearly polarized fundamental $TE_{11}$ mode, are the radially polarized $TM_{01}$ mode.

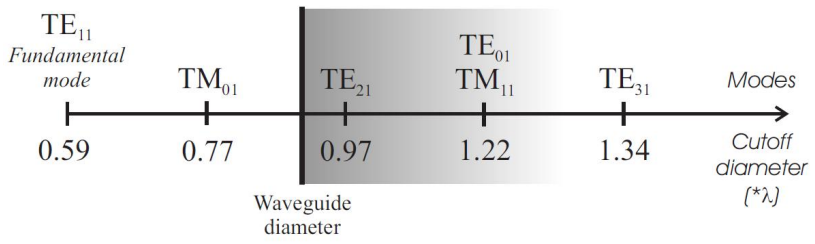


**Figure 5.3: The first modes supported by a hollow core metallic waveguide as the diameter increases** - $\lambda$ is the wavelength [45].

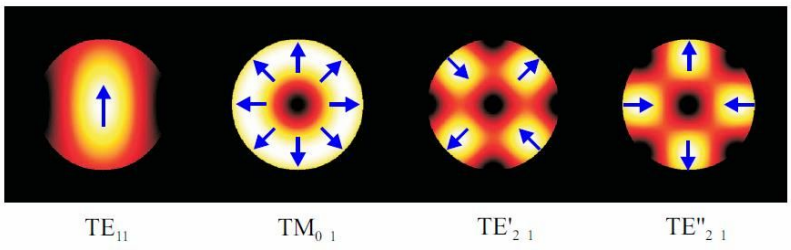


**Figure 5.4: Intensity distribution and electric field orientation (pointed out by arrows) of the first 4 modes supported by a hollow core waveguide with large enough diameter** - [45].

This property of hollow core waveguides can be used to design mode conversion systems from linearly polarized beams to radially polarized beams, as shown in Fig.5.5,

with a discontinuous phase element(DPE), a linearly polarized THz beam is transferred to a mix mode of $TM_{01}$ and $TE_{21}$. After this mix mode passing through a conical hollow core waveguide, of which the diameter of the output end is smaller than the cutoff diameter of $TE_{21}$ mode($0.97\lambda$), the $TE_{21}$ mode will be filtered out, only the radially polarized $TM_{01}$ mode survives.

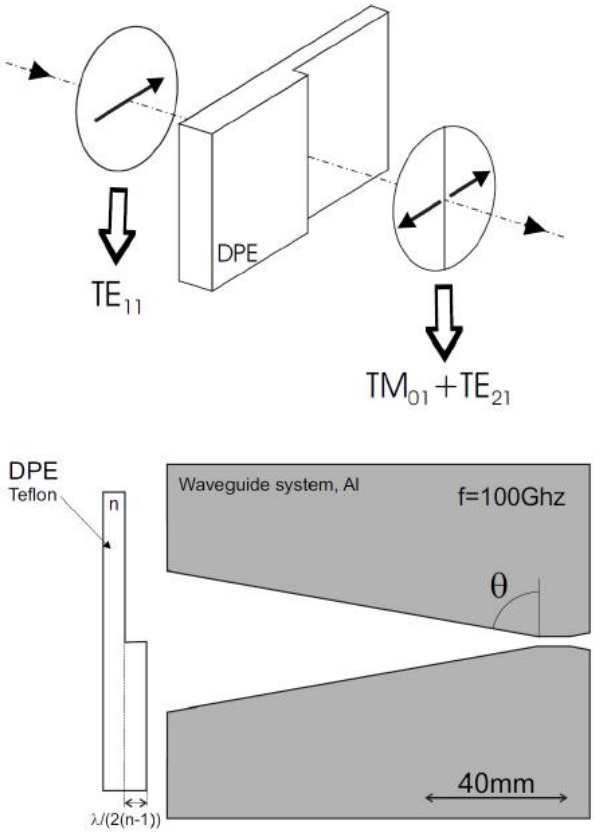


**Figure 5.5: Passive linear-to-radial mode conversion system** - upper: effect of the DPE onto the incident free space Gaussian beam; lower: schema of the first radial polarizer prototype, it is composed of a DPE and a conical waveguide system [45].

It is obvious this method only works at a single frequency, in ref.[45], it is 0.1 THz. So this method can not be used to realize the generation of broadband THz radial beams, and azimuthally polarized THz beams can not be generated with this method.

**THz vector beam generation from axial symmetrical PC antennas**

With special designed axial symmetrical patterns, the PC antennas are able to directly emit radially and azimuthally polarized THz beams [41–44], as shown in Fig.5.6. It should be noted till now only in the results reported by S. Winnerl's group [41, 44], azimuthally polarized THz beams were experimentally realized.

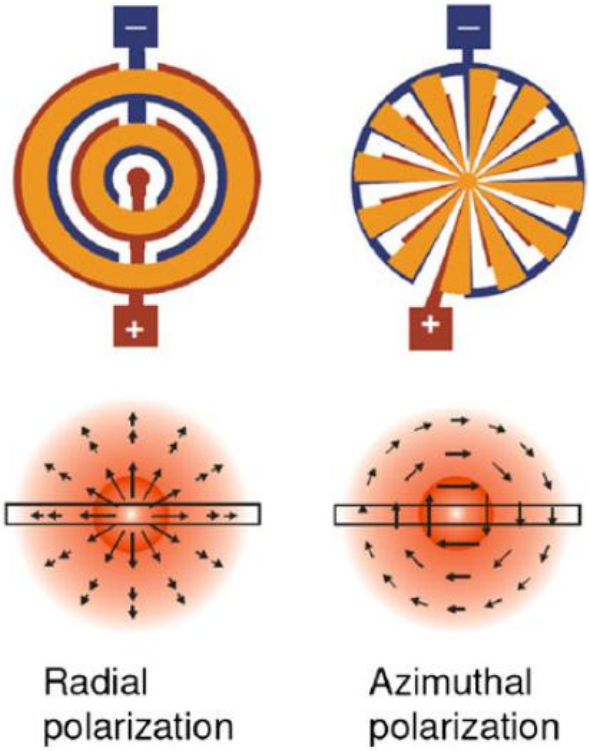


**Figure 5.6: Radial and azimuthal THz beams generated from axial symmetrical PC antenna** - upper: schema of antenna patterns; lower: the related polarization [44].

In comparison with the THz radiation from nonlinear crystals, the bandwidth of the THz radiation from PC antennas is narrower, as described in Chapter 2, for non linear crystals, the upper frequency limit of THz emission is about 50 THz, but for PC antennas, the limit is about several THz; moreover, for PC antennas, the only way to switch from THz radial modes to azimuthal modes, is fabricating another antenna with a different pattern, so it is inconvenient to switch between these two fundamental vector modes in experiments.

## 5.2 Generation of Terahertz Vector Beams with Nonlinear Crystals Possessing 3-Fold Rotational Symmetry

Submitting to the angular momentum conservation law, nonlinear processes occurred in 3-fold rotational symmetrical crystals follow strict selection rules [108]. This fact implies when 3-fold rotational symmetrical nonlinear crystals, e.g., zinc-blende(111) crystals, are used as THz emitters, if the incident laser pulses are linearly polarized, the generated THz pulses will also be linearly polarized, and the polarization of the THz pulses will depend on the polarization of the incident laser pulses, while the amplitude of the THz pulses will be independent of the incident laser polarization, as shown in Fig.5.7. This property which also described in ref.[109], lays the physical basis of the THz vector beam generation methods in this thesis.

Based on this 3-fold principle, an 8-piece segmented GaP(111) crystal and an 8-piece segmented half wave-plate(HWP) laser mode converter are designed and made to genearate radially and azimuthally polarized THz beams. In this section, the THz emission from the (111) plane of zinc-blende crystals will be discussed, and the segmented GaP(111) crystal and the segmented HWP mode converter for THz vector beam generation will be introduced.

### 5.2.1 Terahertz Emission from (111) Plane of Zinc-Blende Crystals

As discussed in Chapter 2, section 2.2.2, when zinc-blende crystals are used to generate THz emission, in the crystal frame, the second-order polarization in nonlinear crystals is shown as eq.5.1:

$$\begin{pmatrix} P_x \\ P_y \\ P_z \end{pmatrix} = 2\epsilon_0 \begin{pmatrix} 0 & 0 & 0 & d_{14} & 0 & 0 \\ 0 & 0 & 0 & 0 & d_{14} & 0 \\ 0 & 0 & 0 & 0 & 0 & d_{14} \end{pmatrix} \begin{pmatrix} E_x^2 \\ E_y^2 \\ E_z^2 \\ 2E_yE_z \\ 2E_zE_x \\ 2E_xE_y \end{pmatrix}. \tag{5.1}$$

In the case that the incident laser pulse is normal to (111) plane of the crystals, setting the laser propagating in $z'$ direction, thus a lab coordinate system $x'y'z'$ is constructed with $z'$ being perpendicular to (111) plane, and $x'$ being normal to the $(\bar{1}10)$ plane,

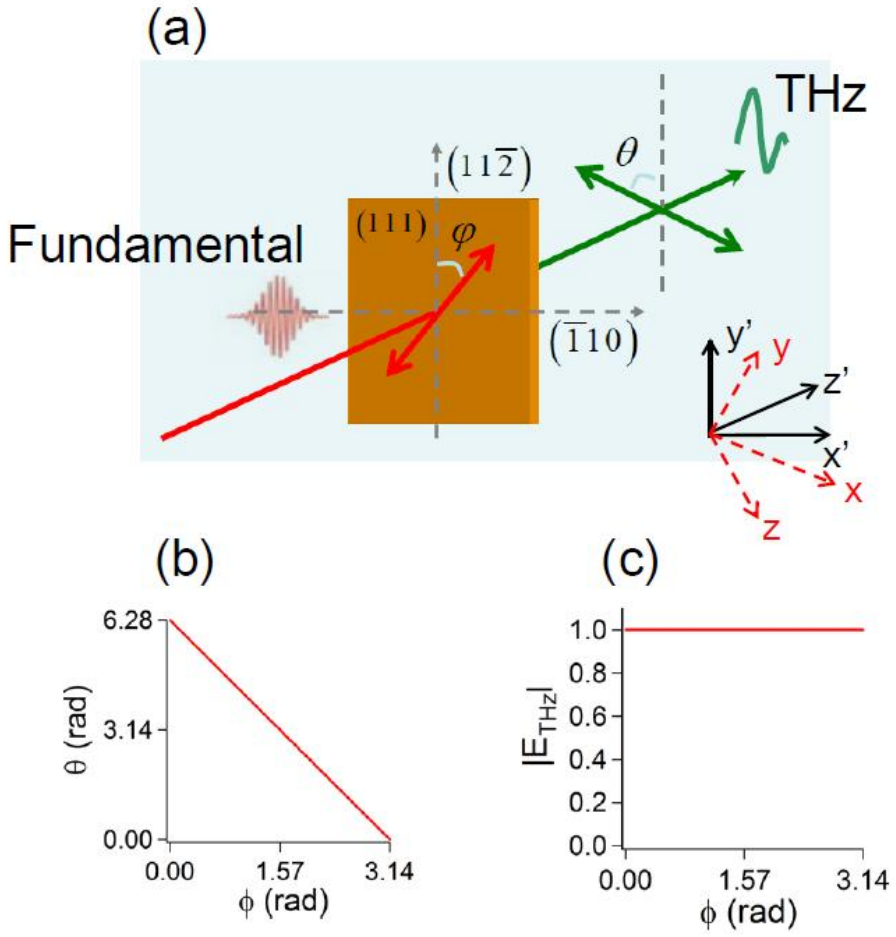


**Figure 5.7: The THz polarization and amplitude dependence of laser polarization** - (a): schema of THz emission from zinc-blende(111) crystals, red arrow: laser polarization, green arrow: THz polarization; (b) and (c): the THz polarization and amplitude dependence of laser polarization.

$y'$ being normal to the $(11\bar{2})$ plane, as shown in Fig.5.7. The transformation relation between the lab system $x'y'z'$ and the crystallographic axes $xyz$ is shown as eq.5.2:

$$\begin{pmatrix} x \\ y \\ z \end{pmatrix} = \begin{pmatrix} -1/\sqrt{2} & -1/\sqrt{6} & -1/\sqrt{6} \\ 1/\sqrt{2} & -1/\sqrt{6} & -1/\sqrt{6} \\ 0 & 2/\sqrt{6} & 1/\sqrt{3} \end{pmatrix} \begin{pmatrix} x' \\ y' \\ z' \end{pmatrix}. \tag{5.2}$$

If a linearly polarized optical beam is normally incident on the (111) plane of crystal, its **E** will be on the (111) plane and can be written in the lab coordinate system $x'y'z'$ as eq.5.3:

$$\mathbf{E}_0(x', y', z') = E_0 \begin{pmatrix} \sin\phi \\ \cos\phi \\ 0 \end{pmatrix}, \tag{5.3}$$

where the angle $\phi$ is the angle between the polarization of the optical pump beam and the $y'$ axis $(11\bar{2})$ as shown in Fig.5.7. Then in the crystallographic system $xyz$, the electric field can be expressed as eq.5.4:

$$\mathbf{E}_0(x, y, z) = E_0 \begin{pmatrix} -1/\sqrt{2}\sin\phi - 1/\sqrt{6}\cos\phi \\ 1/\sqrt{2}\sin\phi - 1/\sqrt{6}\cos\phi \\ 2/\sqrt{6}\cos\phi \end{pmatrix}, \tag{5.4}$$

substituting eq.5.4 to eq.5.1, the nonlinear polarization in the crystal frame $xyz$ is expressed as eq.5.5:

$$\begin{pmatrix} P_x \\ P_y \\ P_z \end{pmatrix} = 4\epsilon_0 d_{14} E_0^2 \begin{pmatrix} 1/\sqrt{3}\sin\phi\cos\phi - 1/3\cos^2\phi \\ -1/\sqrt{3}\sin\phi\cos\phi - 1/3\cos^2\phi \\ -1/2\sin^2\phi + 1/6\cos^2\phi \end{pmatrix}, \tag{5.5}$$

using the coordinate transformation relation eq.5.2, in the lab frame $x'y'z'$, the polarization is:

$$\mathbf{E}_{\mathrm{THz}} \propto \begin{pmatrix} P_{x'} \\ P_{y'} \\ P_{z'} \end{pmatrix} = 4\epsilon_0 d_{14} E_0^2 \begin{pmatrix} 1/\sqrt{6} sin(-2\phi) \\ 1/\sqrt{6} cos(-2\phi) \\ -1/(2\sqrt{3}) \end{pmatrix}. \tag{5.6}$$

Because of the (111) plane of zinc-blende crystals is isotropic, so the THz emission will be parallel to the nonlinear polarization ($\mathbf{E}_{\mathrm{THz}} \parallel \mathbf{P}$). The magnitude of the THz

electric field is thus found to be independent of angle $\phi$, $E_{\mathrm{THz}} \propto 4\epsilon_0 d_{14} E_0^2$ , but its direction $\theta$ (defined in Fig.5.7) changes with angle $\phi$ by [109]:

$$\theta = \arctan\left(\frac{P_{x'}}{P_{y'}}\right) = -2\phi. \tag{5.7}$$

The amplitude of THz emission from (111) plane of zinc-blende crystals is $1/\sqrt{2}$ times smaller in comparison with (110) plane, thus the power is a half.

### 5.2.2 Segmented Wave Plates and Segmented Crystals for THz Vector Beam Generation

Employing (111) plane of zinc-blende crystals, the manipulation of SoPs of THz beams without changing the amplitude becomes possible. Moreover, in the nonlinear processes, the control of SoPs covers the whole frequency range of the THz emission, it means broadband vector beams can be realized using zinc-blende (111) crystals, the bandwidth of the generated vector beams only depends on the bandwidth of THz emission from the crystals. In this thesis, two methods are invented to realize broadband THz vector beams experimentally.

#### Segmented GaP(111) crystal for THz vector beam generation [53]

Cutting several sectors of GaP(111) crystal with pre-designed $(11\bar{2})$ axis orientations, and recombining them, then a segmented crystal with spatial-variant $(11\bar{2})$ axis is obtained for THz vector beam generation. The reason GaP(111) is chosen to make the segmented crystal is that, GaP is frequently used in semiconductor industries, so it is easy to get large wafers of this crystal; moreover, the upper frequency limit of THz emission from GaP(111) is about 7 THz, for the convenience of observing THz vector beams with THz cameras, which are more sensitive in higher spectra, GaP(111) is better than ZnTe(111) (~3 THz). However, in the case of 800 nm laser is used as exitation, the phase matching condition of GaP(111) is not satisfied, then in comparison with ZnTe(111) crystals, the amplitude of THz emission is smaller.

As shown in Fig.5.8, a whole wafer of semi-insulating GaP(111) crystal is prepared, the black arrow indicates the $(11\bar{2})$ axis, the thickness of the wafer is 450 $\mu$m, and the diameter is 2 inches.


**Figure 5.8: A wafer of high resistance GaP(111) crystal** - the thichness of the wafer is 50$\mu m$, and the diameter of the wafer is 2 inches.

Then following the schema shown in Fig.5.9, the GaP(111) wafer is cut to eight triangle pieces, including two pieces with horizontal (11$\bar{2}$) axis in right direction, two pieces with horizontal (11$\bar{2}$) axis in left direction; and two pieces with vertical (11$\bar{2}$) axis in up direction, two pieces with vertical (11$\bar{2}$) axis in down direction, labeled from number 1 to 4, respectively.

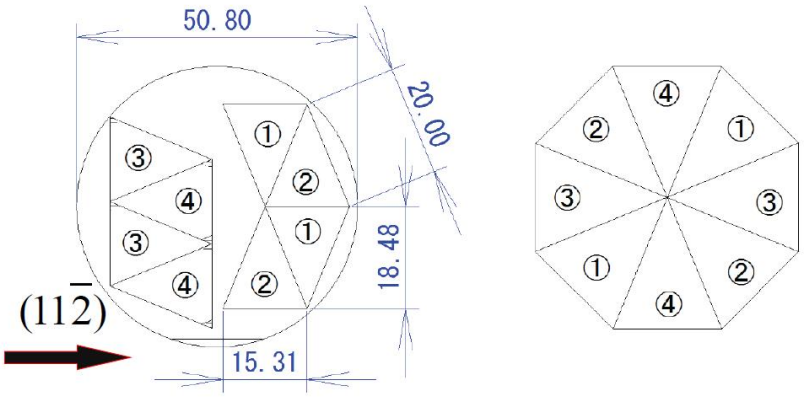


**Figure 5.9: Schema of cutting GaP(111) wafer** - labels: 1. horizontal (11$\bar{2}$) axis in right direction; 2. horizontal (11$\bar{2}$) axis in left direction; 3. vertical (11$\bar{2}$) axis in up direction; 4. vertical (11$\bar{2}$) axis in down direction.

At last, the eight GaP(111) sectors are put delicately on a polytetrafluoroethylene(PTFE) substrate to the designed positions as shown in Fig.5.9. No adhesive is used between the PTFE substrate and the GaP(111) sectors, or between each piece of

GaP(111), to ensure the generated THz emission will not be effected by the adhesive material. In Fig.5.10, a schema of the segmented GaP(111) crystal and a photo of this element are shown.

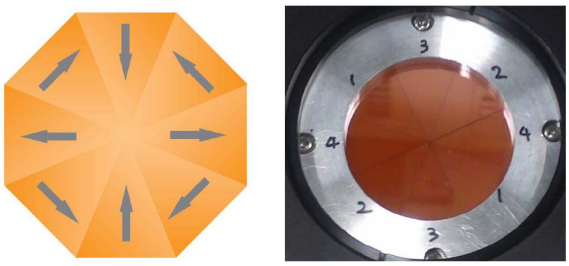


**Figure 5.10: Segmented GaP(111) crystal for THz vector beam generation** - left: a schema of the segmented GaP(111) crystal; right: a photo of the segmented GaP(111) crystal.

With fundamental laser beam linearly polarized in horizontal or 45° direction passing through this segmented GaP(111) crystal, both radially polarized and azimuthally polarized THz vector beams can be realized. So in this method, switching between radially and azimuthally polarized THz is easy in experiments, by only rotating the polarization of the excitation laser beams, or the segmented crystal by 45°, radial beams and azimuthal beams are switchable, as shown in Fig.5.11.

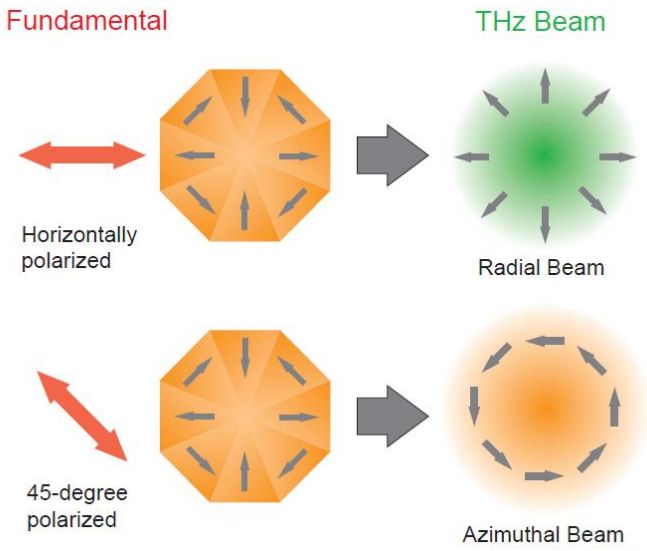


**Figure 5.11: THz vector beam generation from the segmented GaP(111) crystal** - upper: radial beam; lower: azimuthal beam.

**Segmented half-wave plate for THz vector beam generation[78]**

When an excitation laser beam with a specially designed inhomogeneous polarization state passing through a zinc-blende(111) crystal, THz vector beams can be realized (Fig.5.12). To realize such excitation laser beam for THz vector beam generation, a predesigned laser mode converter, consisting of eight pieces of half-wave plate (HWP), was made to transfer the SoPs of the incident laser beams. The fast axis of each piece of HWP is arranged as shown in Fig.5.12(a). When laser beams linearly polarized along the fast axis direction of the top marked piece[Fig.5.12(b)] passing through this element, the laser beams will be converted to the polarization-spatial-variant mode for THz vector beam generation, as shown in Fig.5.12(a).

The THz vector beams can be generated by exciting a whole wafer of zinc-blende(111) crystal with the polarization-spatial-variant mode, as shown in Fig.5.13. Similar as THz vector beam generation with the segmented crystal, switching between radially and azimuthally polarized THz beams can be achieved by simply rotating the orientation of the $(11\bar{2})$ axis of the nonlinear crystal by 90° (Fig.5.13).

In this method, any zinc-blende(111) crystal can be used as the THz generation medium. In comparison with the segmented GaP(111) crystal, ZnTe(111), which is

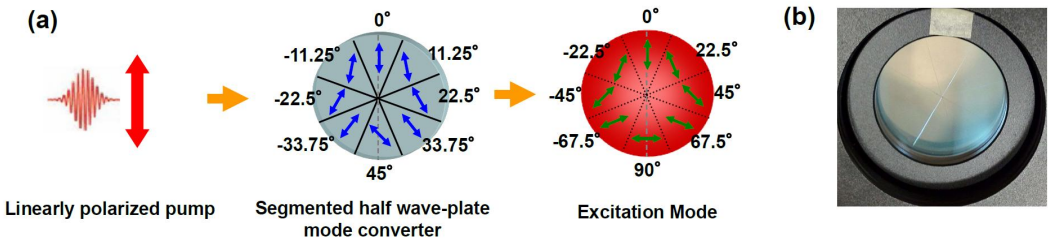


**Figure 5.12: Segmented HWP mode converter** - (a) schematic of the function of the segmented HWP mode converter. The red arrow indicates the polarization direction of the incident beam. The blue arrows show the fast axis orientation for each piece of the wave-plate. The green arrows indicate the polarization direction inside the polarization-spatial-variant mode; (b) A photograph of the segmented HWP mode converter.

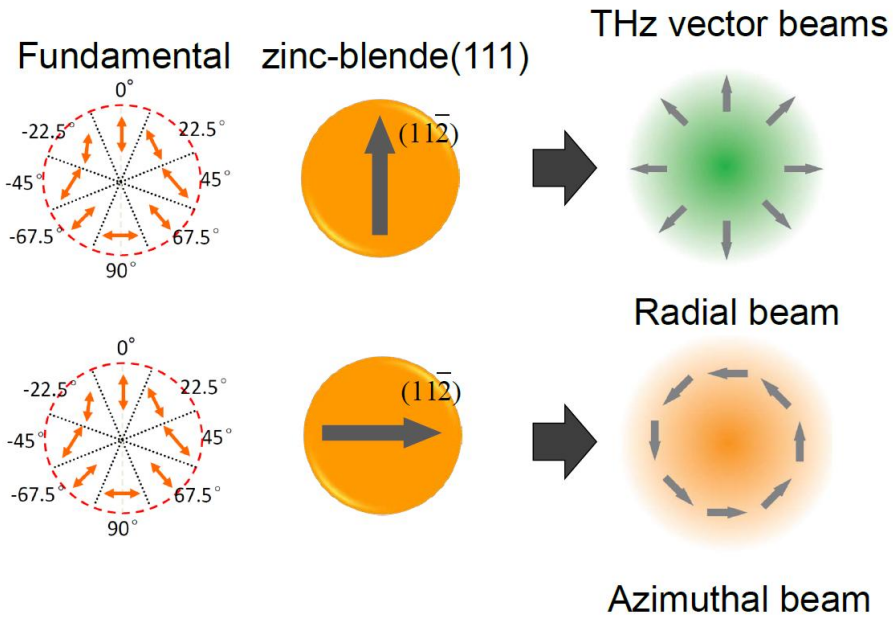


**Figure 5.13: THz vector beam generation from the special polarization-spatial-variant laser mode** - upper: radial beam; lower: azimuthal beam.

difficult to get a large high-qualified wafer, can now be used to generate THz vector beams, and the THz signal from ZnTe(111) is larger than GaP(111) in the case of 800 nm excitation. Of course, in this method GaP(111) can also be used for THz generation to achieve a broader spectrum of generated THz vector beams.

In these two methods, eight-piece approximate devices are used because it is difficult to realize a nonlinear crystal in which the crystal axis varies continuously in space, or an ideal polarization-spatial-variant laser mode. Then different from continuous ideal vector modes, the generated THz vector beams are quasi-vector modes. However, in the case of eight-piece elements are used, the mode overlap between an ideal vector beam and such quasi-vector beam was evaluated as large as 93% [110].

In comparison with reported generation methods of THz vector beams [41, 44–46, 49, 50], these two new methods hold the advantages that stable, broadband, simple in optical alignments and easy-switchable between radially and azimuthally polarized THz beams.

## 5.3 Mode Profile Characterization of Terahertz Vector Beams

With the segmented GaP(111) crystal or the segmented HWP mode converter, THz vector beams can be generated experimentally. The next task of this chapter is to characterize the generated THz vector beams. Firstly, the in-plane electric components should be characterized, to confirm the polarization features of the generated THz vector beams. THz cameras and 2D THz-TDS setups are employed to do this work.

### 5.3.1 Mode Profiles Taken with Terahertz Cameras

THz cameras (IRV-T0830 and IRV-T0831HS, NEC Corp.) were used to record the intensity distribution of in-plane electric components of the THz vector beams, the details and the performance evaluation of the THz cameras used in the experiments can be found in ref.[79].

For the segmented GaP(111) crystal, the experimental setup is shown in Fig.5.14. In this setup, a THz camera (IRV-T0830, NEC Corp.) is used. Since the sensitivity of this camera is low in the lower frequency range, we used GaP(111) crystals, which can generate higher frequency THz emission than ZnTe(111) crystals, and Legend Elite (described in Chapter 3) was used as the excitation laser, because the shorter pulse duration and the higher pulse energy in comparison with other lasers in the lab ensure larger relative THz emission in higher frequency range. The laser was expanded with a beam expander, and directly passed through the segmented GaP(111) crystal. After the crystal, PTFE films and black polypropylene films were used to block the laser beam, while allowing the THz vector beams to pass, and directly before the THz camera sensor, metal mesh filter is attached to fill out the spectrum larger than 10 THz. The generated THz radially and azimuthally polarized beams were focused with a THz lens (Tsurupica, Pax Corp.), in the focal plane, the THz camera (IRV-T0830, NEC Corp.) was placed to record the intensity distribution of electric components. A wire grid polarizer(WGP) was inserted to analyze the polarization features of the vector beams. [1,2]

[1] In fact, the sensitivity of the THz cameras depends on the polarization of incident THz beams [111].

[2] It is possible that we can not observe longitudinally polarized electric component in the focal plane of radial THz beams with THz cameras, simulations and experiments will be carried to confirm this point.

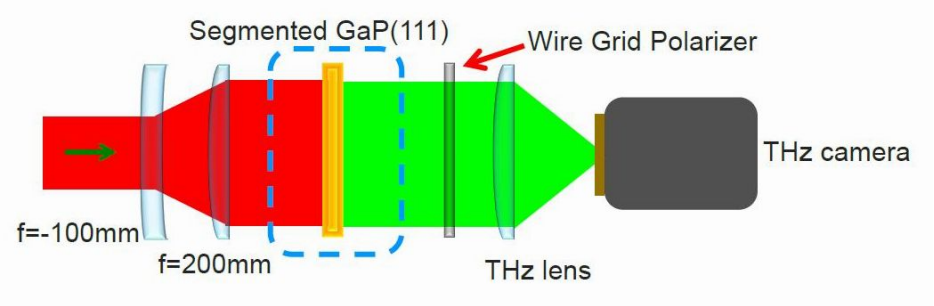


**Figure 5.14: Schema of the THz camera experimental setup** - the segmented GaP(111) crystal was used to generate THz vector beams.

The polarization dependent mode profiles of THz vector beams from the segmented GaP(111) crystal taken with the THz camera (IRV-T0830, NEC Corp.) are shown in Fig.5.15. The red arrows indicate the orientation of the WGP, whereas the first column is taken without WGP. From the pictures, donut shapes of both radial and azimuthal THz modes are observed without WGP; while with inserting and rotating the WGP, two lobes aligned along or perpendicular to the polarization direction are clearly recorded. These results unambiguously indicate that THz radial and azimuthal beams were successfully generated.

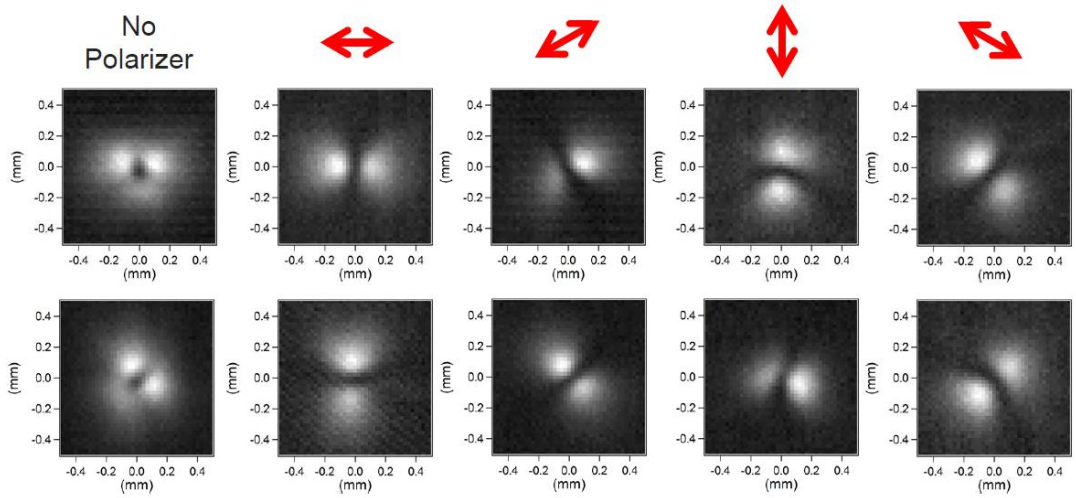


**Figure 5.15: Mode profiles of THz vector beams from the segmented GaP(111) crystal recorded with a THz camera (IRV-T0830, NEC Corp.)** - upper row: radial beam; lower row: azimuthal beam; the leftmost column was obtained without WGP, the red arrows indicate the orientation of a WGP.

For the segmented HWP mode converter, the experimental setup is almost the same, as shown in Fig.5.16. The only difference is in this setup the segmented HWP and a whole wafer of ZnTe(111) were used to generate THz vector beams, because of in this measurement, a new high sensitivity THz camera (IRV-T0831HS, NEC Corp.) was used, the response of this camera in lower frequency range is improved. In this measurement, Hurricane (described in Chapter 3) was chosen as the excitation laser.

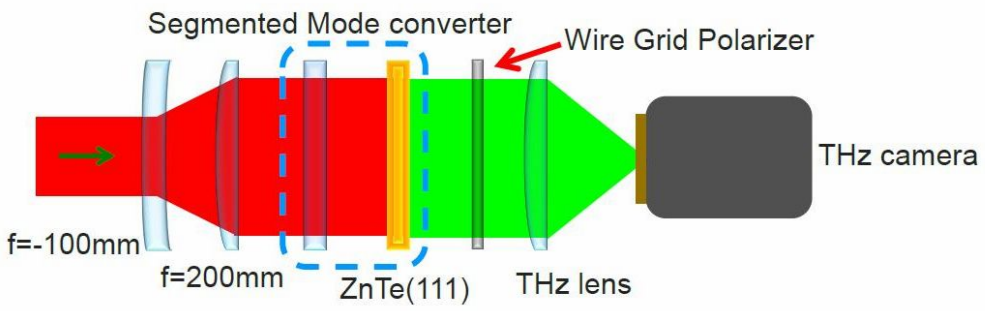


**Figure 5.16: Schema of the THz camera experimental setup** - the segmented HWP and a whole wafer of ZnTe(111) were used to generate THz vector beams.

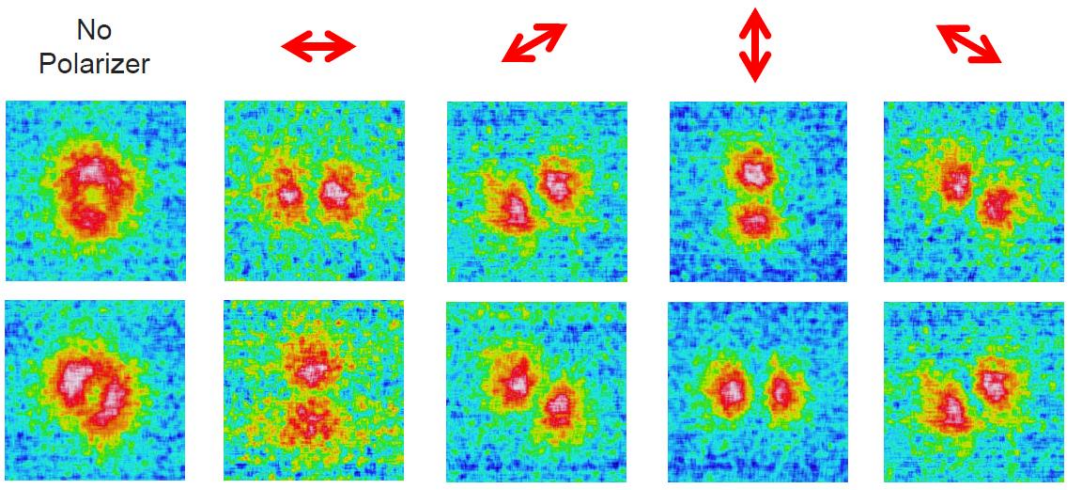


**Figure 5.17: Mode profiles of THz vector beams from the segmented HWP and a ZnTe(111) crystal recorded with a THz camera (IRV-T0831HS, NEC Corp.)** - upper row: radial beam; lower row: azimuthal beam; the leftmost column was obtained without WGP, the red arrows indicating the orientation of a WGP.

In this measurement, a new high-sensitivity THz camera (IRV-T0831HS, NEC

Corp.) was used. The polarization dependent mode profiles of THz vector beams taken with this new THz camera are shown in Fig.5.17, the donut intensity distribution of in-plane electric components and the two lobes related to the polarization direction are clearly observed, confirming the polarization features of THz radial and azimuthal beams. [1]

### 5.3.2 In-plane Electric Components Recorded with 2D THz-TDS Setups

In the optical range, it is difficult to record the phase information of beams. However in the THz range, employing TDS setups, both amplitude and phase features can be recorded in the measurements, so it offers a chance to directly confirm the local SoPs of THz vector beams. In this part, 2D antenna sampling lines are built to characterize the THz vector beams from the segmented GaP(111) crystal or the segmented HWP and a ZnTe(111) crystal. The experimental setup directly follows Fig.3.16 in Chapter 3, in which the THz emitter was the segmented GaP(111) crystal or the segmented HWP and a ZnTe(111) crystal to generate THz vector beams. In all the measurements, Hurricane was used as the excitation laser, and the experimental setup was purged with dry nitrogen gas to prevent absorption of the beams by water vapor.

In the 2D THz-TDS measurements, waveforms at each point are recorded. As shown in Fig.5.18, in the central line of vertically polarized electric component [indicated by the red solid arrow in Fig.5.18 (a), and the red dashed arrow Fig.5.18 (b)], the waveforms are listed in Fig.5.18 (b). It is clear that at offsets in x axis of +1.2 mm and -1.2 mm [marked as the black arrows in Fig.5.18 (a)] from the central dark point, the THz waveforms are opposite [indicated by the black arrows in Fig.5.18 (b)]. These opposite waveforms certificate that at these two positions, the local polarization is along the direction shown as the black arrows in Fig.5.18 (b), this is a direct evidence of vector beams.

For a THz radial beam from the segmented HWP and a ZnTe(111) crystal, the similar results are shown in Fig.5.19.

Moreover, we evaluated the intensity distribution overlap of the in-plane electric components between an ideal focused vector beam and our experimental data obtained by 2D antenna scanning, the result is shown as Fig.5.20, the theoretical and

[1] Because of the polarization dependence of the THz camera, the S/N ratios of x- and y- polarized components are a little different.

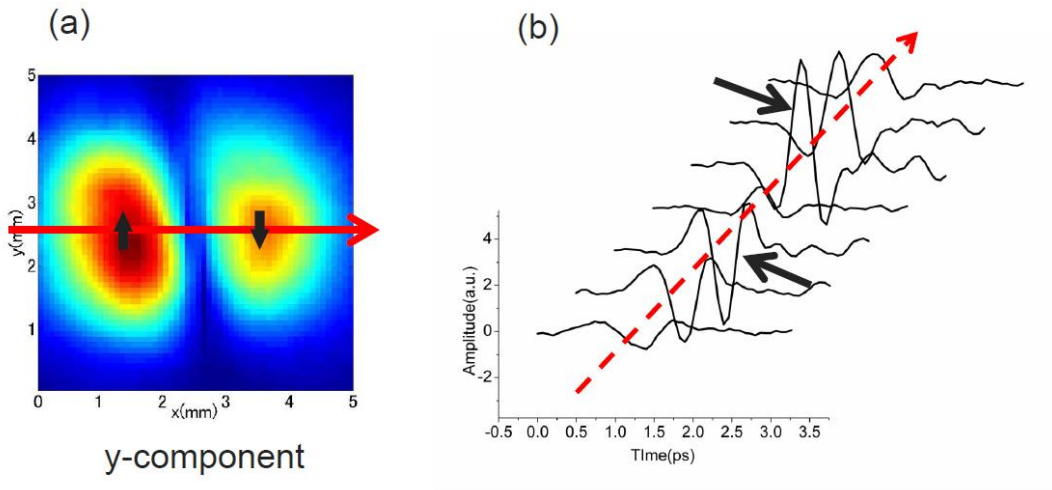


**Figure 5.18: Vertically polarized electric component of a THz azimuthal beam from the segmented GaP(111) crystal** - (a): intensity distribution of vertically polarized electric component, the black arrows indicate the local polarization; (b): waveforms in the central line [indicated by the red solid arrow in (a)].

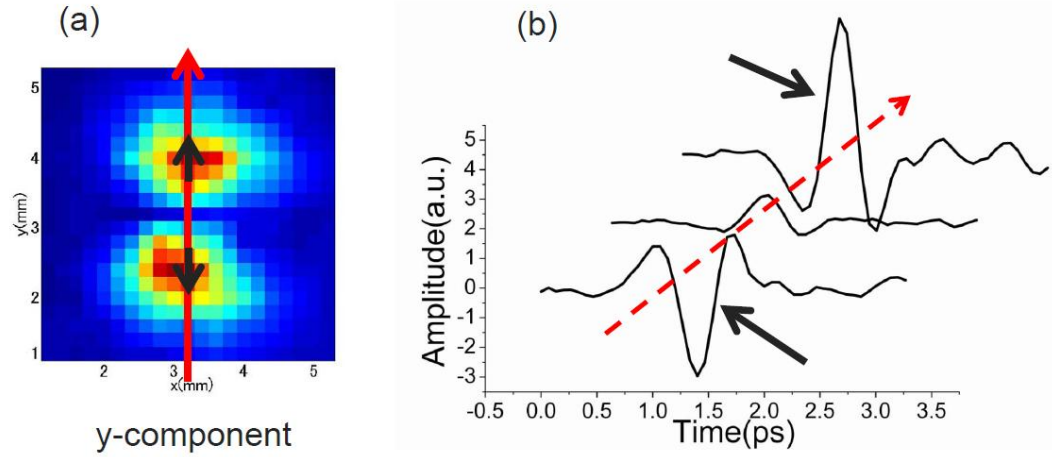


**Figure 5.19: Vertically polarized electric component of a THz azimuthal beam from the segmented HWP and a ZnTe(111) crystal** - (a): intensity distribution of vertically polarized electric component, the black arrows indicate the local polarization; (b): waveforms in the central line [indicated by the red solid arrow in (a)].

experimental results at 0.3 THz are plotted. From the figure, the high quality of THz vector beams in this method is confirmed.

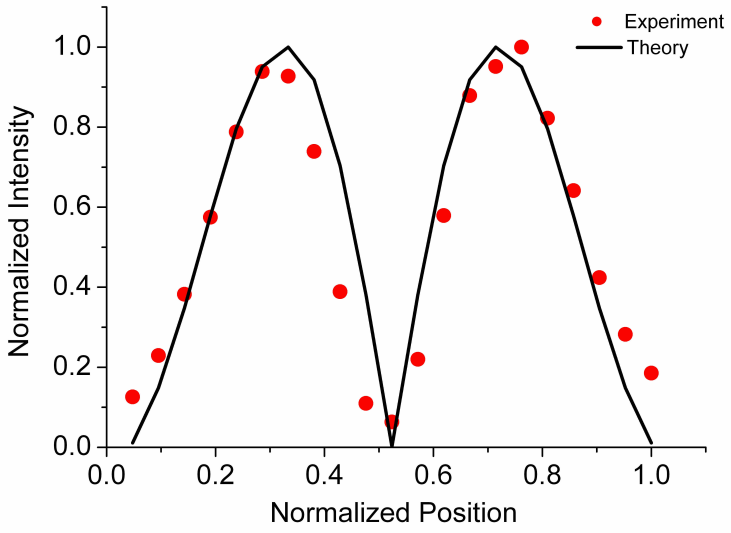


**Figure 5.20: Mode overlap between an ideal focused vector beam and experimentally measured data** - The profiles at 0.3 THz are shown, Black solid line: the theoretical prediction of an ideal focused CV beam; Red dots: experimental data.

From the results shown above, the polarization features of THz vector beams are directly observed in the experiments.

## 5.4 Characterization of Longitudinal Electric and Magnetic Field in Focal Volume of Terahertz Vector Beams

One of the most important focal features of vector beams is that, there is a localized longitudinally polarized (z-polarized) electric or magnetic component in the focal volume of radially polarized or azimuthally polarized beams, respectively. In the optical range, knife edge measurements are performed to confirm the longitudinally polarized electric component in the focus of radial beams [1]. However, in the measurements, the phase information of the longitudinal electric component ($E_z$) was not obtained. Moreover, because of the lack of magnetic response in both the optical and the THz spectrum, the longitudinal magnetic component ($H_z$) in the focal volume of azimuthally polarized beams is not experimentally confirmed up to date.

In this section, benefitting from THz-TDS measurements, the characterization of full information, including the amplitude and phase features, of both $E_z$ in the focus of radial beams and $H_z$ in the focus of azimuthal beams is experimentally realized.

### 5.4.1 Longitudinal Electric Field

This part is following ref.[53]. To detect $E_z$ in the focus of THz radial beams, a 2D EO sampling setup, as introduced in Fig.3.15, Chapter 3, was built. It should be noted, for the purpose of detecting $E_z$, the detection crystal was replaced to be ZnTe(100), which is only sensitive to longitudinally polarized electric THz field [109]. In the experiments, a THz lens with 30 mm focal length was used to focus THz radial beams, and the excitation laser was Hurricane. The results of $E_z$ are shown in Fig.5.21, from the figure, the spatial-temporal image of $E_z$ is observed [Fig.5.21(a)], and a Fourier transformation in time domain is taken, then in space-frequency domain, the distribution of $E_z$ is shown as Fig.5.21(b), the experimental results have a good correspondence with theoretical calculations [Fig.5.21(c), calculated following eq.4.25 and eq.4.26].

If the detection crystal is slightly tilted in the EO sampling setup, a transversal component is observed as a longitudinal component, and vice versa, resulting in some artifact signals. In the current case, the amplitude of the transversal component is expected much stronger than that of the longitudinal component; hence, it is important to exclude the ambiguity due to such artifacts.

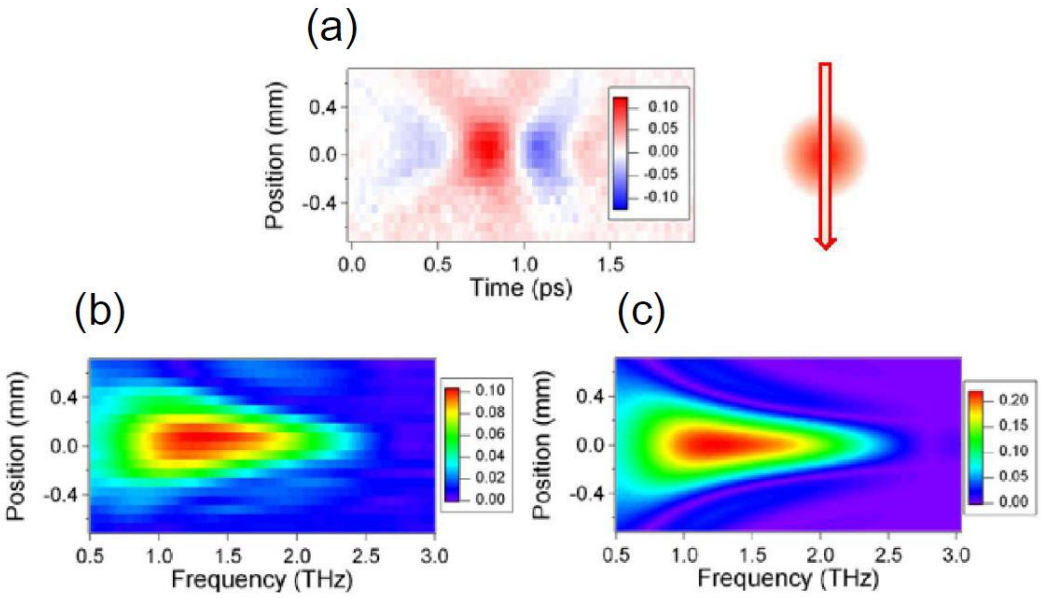


**Figure 5.21: Distribution of** $E_z$ - (a): spatial-temporal image of $E_z$; (b): experimental spatial dependence of THz spectra obtained through the Fourier transformation of the upper figure; (c): theoretically calculated spatial dependence of THz spectra.

As introduced in section 4.2.2, Chapter 4 , in the focal volume of radial beams, there will be localized $E_z$, while in the focal volume of azimuthal beams, the $E_z$ will vanish, as shown in Fig.5.22. Because it is easy to experimentally switch between THz radial and azimuthal beams using the THz vector beam generation methods in this thesis, this feature can be used to confirm the detected $E_z$ is from radial mode focusing. The results are shown in Fig.5.23, from the figure, the vanishing of $E_z$ when we switched from a radial beam to an azimuthal beam is confirmed.

Moreover, as introduced in eq.4.26, between in-plane electric components and longitudinal electric component in the focus of radial beams, there is a constant $i$ difference, which means a $\pi/2$ phase shift should exist between the in-plane electric components and the longitudinal electric component. By using ZnTe(110) or ZnTe(100) as the detection crystals in the 2D EO sampling line, the in-plane electric components or the longitudinal electric component were recorded, this phase shift was confirmed through these results, as shown in Fig.5.24.

All of these experimental results described above, i.e., the electric field distribution,

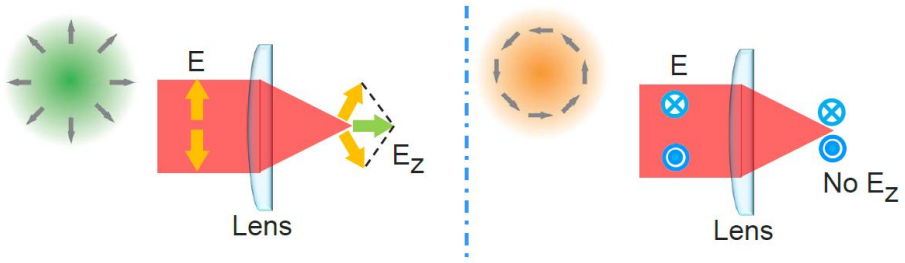


**Figure 5.22: Schema of focusing radial and azimuthal beams** - for radial focusing, a large $E_z$ exists; for azimuthal focusing, $E_z$ vanishes.

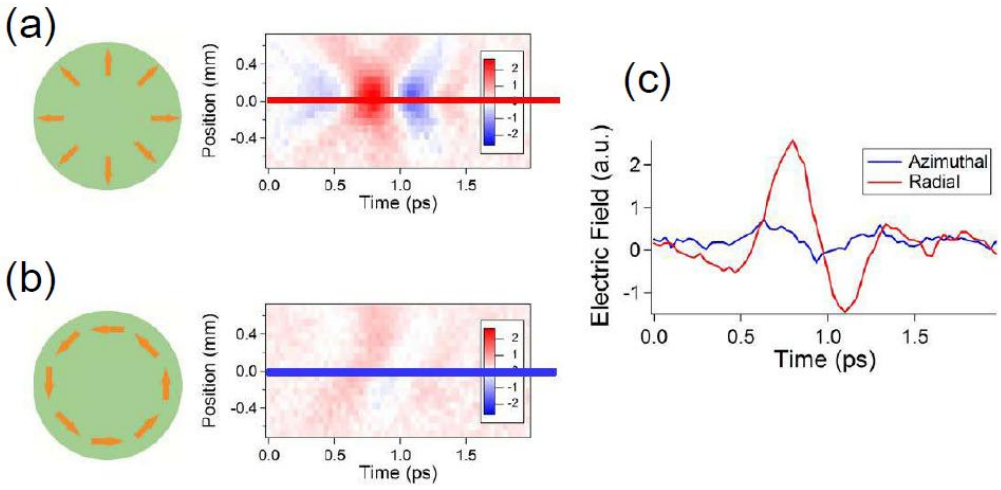


**Figure 5.23: Experimental confirmation of vanishing of** $E_z$ - (a): radial focusing; (b): azimuthal focusing; (c): waveforms at the central point indicated by the red and blue lines in the left.

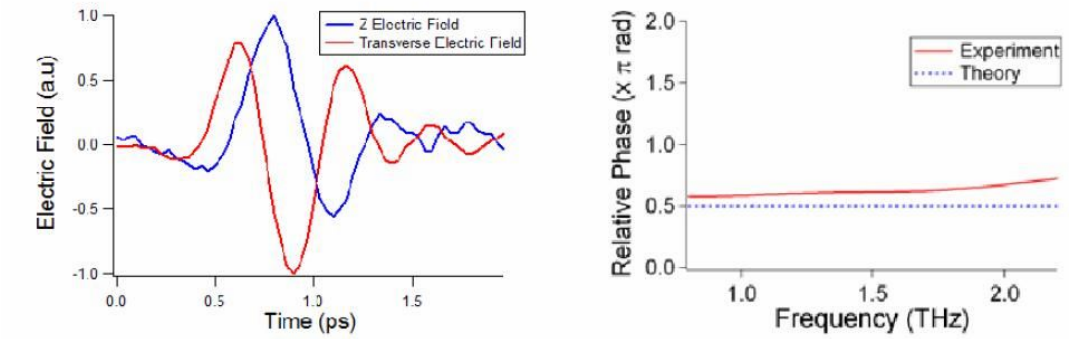


**Figure 5.24: Phase shift between in-plane electric components and longitudinal electric component** - left:THz waveforms; right: relative phase differences of the transverse and longitudinal electric components.

the vanishing of $E_z$ for azimuthal focusing, and the relative phase shift, are consistent with the theoretically predicted properties of longitudinal electric component in the focus of radial beams. Therefore, it is concluded that the longitudinal electric component is experimentally detected by focusing a THz radial beam.

### 5.4.2 Longitudinal Magnetic Field

For the detection of $E_z$, ZnTe(100) can be used. However, in the THz range, as Landau and Lifshitz argued [112], the magnetic susceptibility of all natural materials tails off at microwave frequencies, which means, the characterization of THz $H_z$ component in the focal volume of azimuthal beams will be a quite difficult task.

It is the nature of electromagnetic field, that both $E$ and $H$ components never happen without other ones. $E$ and $H$ components are strongly correlated through the Maxwell's Equations. In another word, $H$ originates from the spatial-temporal inhomogeneity of $E$, and vice versa. Then if we write down the component form of the Maxwell's Equations in Cartesian coordinate system, it should be noted the longitudinal magnetic component ($H_z$) is only related to the in-plane $E$ components, as described in eq.5.8:

$$-\mu\frac{\partial H_z}{\partial t} = \frac{\partial E_y}{\partial x} - \frac{\partial E_x}{\partial y}. \tag{5.8}$$

It means if a measurement includes all information of the spatial-temporal distribution of in-plane electric components $E_x$ and $E_y$, then from the data, the distribution of $H_z$ can be extracted. For example, in 2D THz-TDS systems, recording the distribution of $E_x$ and $E_y$ in space-time is possible, the recorded data are two discrete matrices $E_x^t(x, y)$ and $E_y^t(x, y)$ with the space steps $\Delta x$, $\Delta y$ and the time step $\Delta t$. Then through the discrete version of eq.5.8, as described in eq.5.9, $H_z$ can be easily rebuilt.

$$\begin{aligned} &-\mu \frac{H_z^{t+\Delta t}(x+0.5\Delta x, y+0.5\Delta y) - H_z^{t}(x+0.5\Delta x, y+0.5\Delta y)}{\Delta t} \\ &= \frac{E_y^{t+0.5\Delta t}(x+\Delta x, y) - E_y^{t+0.5\Delta t}(x, y)}{\Delta x} - \frac{E_x^{t+0.5\Delta t}(x, y+\Delta y) - E_x^{t+0.5\Delta t}(x, y)}{\Delta y}. \end{aligned} \tag{5.9}$$

2D THz-TDS measurements were performed to record the spatial-temporal distribution of the in-plane electric components $E_x$ and $E_y$ in the focal plane of an azimuthally polarized THz beam, as shown in Fig.5.25, with time flowing(the red arrows), the spatial distributions of $E_x$ and $E_y$ are roughly pictured (in the figure, only seven time steps are shown, while in the real measurements, the time step number is 100).

The rebuilt $H_z$ in the focus of the azimuthally polarized THz beam is shown in Fig.5.26, the 2D distribution, the spatial-temporal image and the waveform at central point of $H_z$ are plotted. In this measurement, the segmented GaP(111) crystal is used to generate the azimuthally polarized THz beam, in the focus, the peak magnetic field is evaluated to be in the order of $10^{-6}$ T, this number can be several times improved if we use ZnTe(111) as the THz crystal.

From Fig.5.26, the characterization of $H_z$ in the focus of an azimuthally polarized THz beam is successfully achieved.

In this method to map the magnetic field, besides the directly measured in-plane electric waveforms, as implied in eq.5.8, the rebuilt $H_z$ is also determined by two other hidden parameters: the time step $\Delta t$ and the space step $\Delta x$ /$\Delta y$. Because the $H_z$ features are deducted from the in-plane electric field, similar as introduced in Chapter 2.3, the frequency resolution $\Delta\omega$ and the upper frequency limit $\omega_{\max}$ of rebuilt $H_z$ are determined by the time sampling step $\Delta t$ and the total sampling time $T$, the relation is shown as: $\frac{\Delta\omega}{2\pi} \cdot T = 1$; $\frac{\omega_{\max}}{2\pi} \cdot \Delta t = 1$. Moreover, from eq.5.9, the expression before the equal sign is a time derivation of $H_z$, to ensure the validity of this method, the homogeneity of the time derivation of $H_z$ in the time interval $\Delta t$ should be assumed,

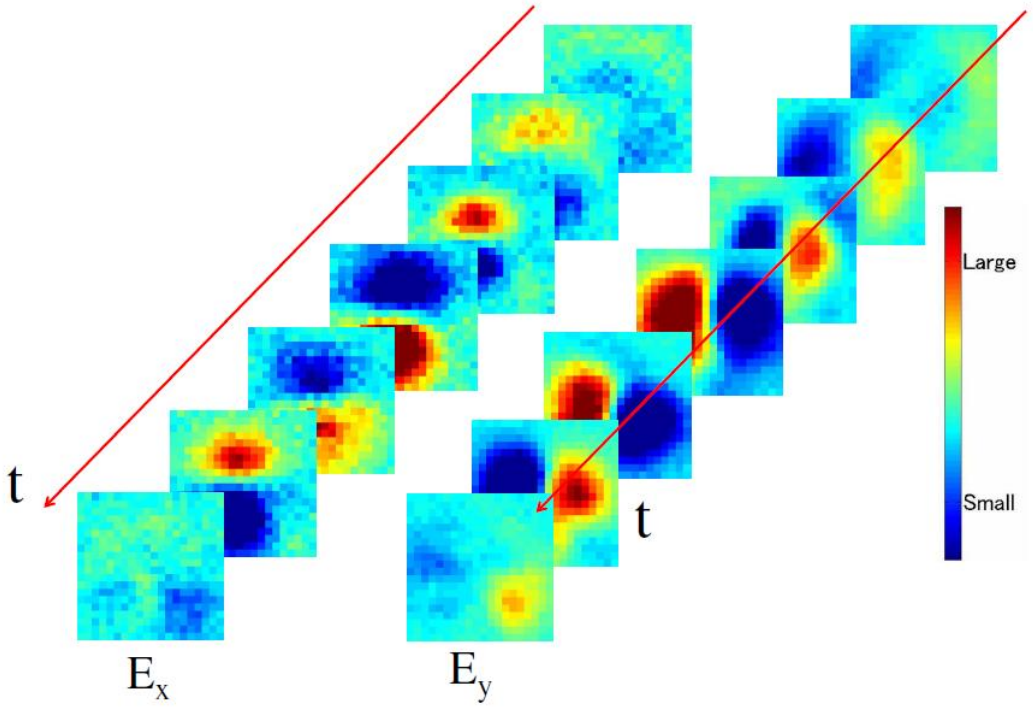


**Figure 5.25:** $E_x$ **and** $E_y$ **in the focal plane of an azimuthally polarized THz beam** - the spatial distributions with time evolving are shown.

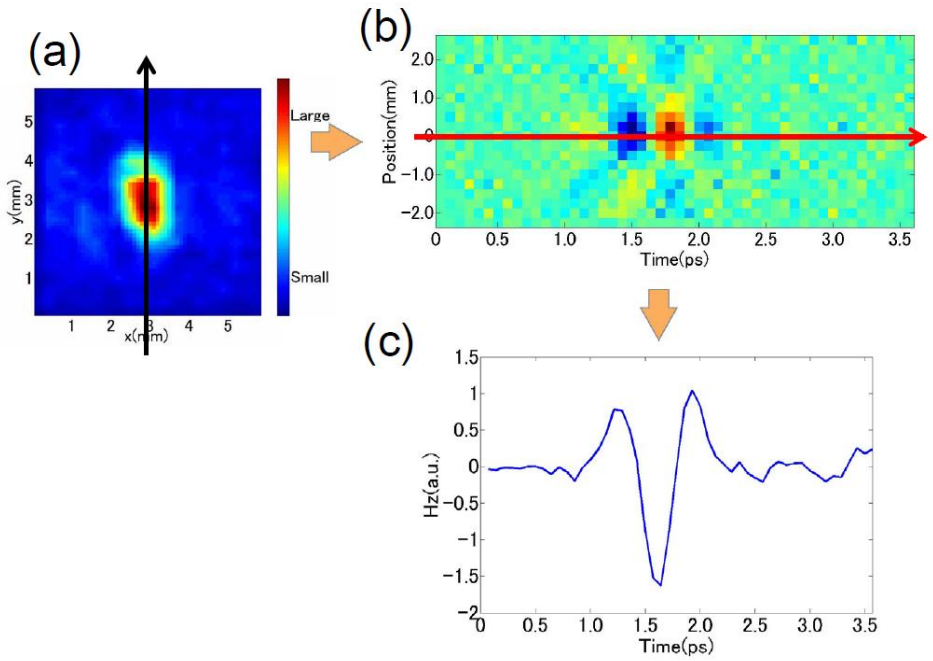


**Figure 5.26: The rebuilt** $H_z$ - (a): 2D distribution of $H_z$, in the central line indicated by the black arrow, the spatial-temporal image is shown as (b); in the central point (red arrow), the waveform is shown as (c).

similarly, in the space interval $\Delta x$ /$\Delta y$, the local electric field should be supposed to be homogeneous. In our measurements, $\Delta t$ is 0.05 ps and $\Delta x = \Delta y = 0.25$mm. To increase the accuracy of this method, improving the space resolution of 2D TDS systems is important.

Chapter 6

# Efficient Coupling of Terahertz Radial Beams to Metal Wires

As one of the most important applications, THz vector beams can be introduced to efficiently couple and propagate in some waveguides. One example is efficient coupling of broadband propagating THz radial beams to bare metal wires, which have characters of low-attenuation and low-dispersion as THz waveguides in a broad spectral range. This technique is potentially applicable for the development of new THz elements.

In this Chapter, a brief introduction to THz waveguides will be given, in the introduction, we emphasize on bare metal wire waveguides [51], which is proved to be one of the best choice of THz waveguiding due to its structural simplicity, low-dispersion and low-attenuation propagation. An efficient coupling scheme to bare metal wires with THz radial beams is the main topic of this Chapter, the experimentally determined data of energy coupling efficiency are shown for the first time. Moreover, the advantages that low-attenuation and low-dispersion of bare metal wire waveguiding are proved to be available in a larger spectral range (up to 2 THz).

Based on the method of efficient coupling of THz radial beams to metal wires, we propose three plans for the next step of our experiments, they are a wire splitter, a tapered tip for plasmonic near-field focusing, and a near-field probe for THz subwavelength imaging. Simulation results are shown to confirm these plans.

## 6.1 A Brief Introduction to Terahertz Waveguides

At present, most THz technologies rely on free propagation of waves rather than on waveguide transportation. THz waveguides provide a promising approach for

overcoming the limitations of the system that use these technologies, such as large diffraction and bulky volumes. However, in the THz range, efficient waveguiding is challenging owing to high losses from the finite conductivity of metals or high absorption of dielectric materials in this spectral range. Moreover, to enjoy the wide bandwidth (0.1-10 THz) of typical time domain measurements, it is necessary to find a guiding scheme without obvious dispersion; the wide band range required for typical time domain measurements makes it difficult to find a guiding scheme without obvious dispersion.

In other words, an efficient THz waveguiding scheme should at least fulfill three basic requirements, they are structural simplicity, low attenuation and low dispersion. Until now, dielectric structures such as planar dielectric waveguides [113], dielectric fibers [114], and polymer tubes [115] as well as metallic structures such as rectangular waveguides [116], slit waveguides [117], and parallel plate waveguides [118] have been shown to support THz wave propagation. However, from the reported theoretical and experimental results, none of the waveguides mentioned above satisfies all three demands, e.g., for metal tubes [119], both attenuation and dispersion is obvious; for dielectric tubes [120], the attenuation is not negligible; for parallel plate waveguides, the structure is bulky.

Bare metal wires, which support a plasmonic mode (known as Sommerfeld wave [121]) on their surfaces in THz range, are one of the best candidates for guiding THz waves because of their very low losses, dispersionless propagation (as shown in Fig.6.1, from the figures, the group velocity of the guiding mode is very near to $c$, and the actuation keeps a low level), and structural simplicity.

However, compared to the other THz waveguides, the cylindrical symmetry of metal wire waveguides poses a significant challenge because the typical linearly polarized THz wave has a very poor spatial overlap with the Sommerfeld mode that is radially polarized. A large mismatch between the waveguide mode and the free propagating mode results in very low incoupling efficiency. In early experiments of THz waveguiding with bare metal wire, the scattering in-couple method was employed [51], but the measured coupling efficiency was lower than 0.5% [42, 122].

To increase the coupling efficiency, radially symmetric antennas [42, 43], mode filters [45, 123], plasmonic in-couplers [124, 125], or directly generating radially polarized modes on metal wires [50] were tried. However, the reported results suffer from

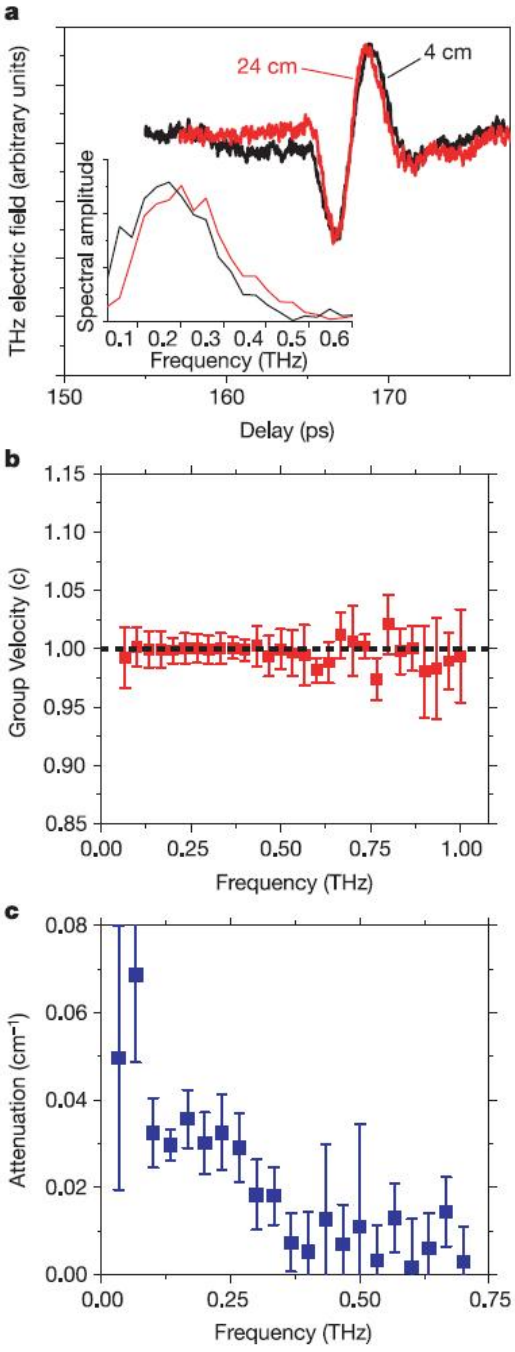


**Figure 6.1: Characteristics of the propagating mode** - (a) THz waveforms measured after 4 cm(black) and 24 cm(red) of propagation distance along the wire; (b) group velocity of the propagating mode as a function of frequency; (c) the electric field amplitude attenuation coefficient of the propagating mode as a function of frequency [51].

narrow bandwidth, typically under 0.5 THz. Moreover, until now, efficient coupling of broadband propagating THz waves to bare metal wires has not been realized, and experimental evaluations of the increased coupling efficiency are not performed.

Previously, in ref.[42], Deibel et al. estimated theoretically a high coupling efficiency for a radially polarized THz emission from a radially symmetric photoconductive antenna with a hyperhemispherical lens to a metal wire (as shown in Fig.6.2). The method was demonstrated without experimental determination of efficiency. Introducing the broadband THz vector beams described in Chapter 5, which is also a promising component in realizing efficient coupling to bare metal wires. Applying this generation method in this thesis, we demonstrate efficient coupling to metal wires from radially polarized THz beams propagating in free space by focusing with conventional lenses. The coupling efficiency is experimentally evaluated, and mode-overlap calculation and numerical simulation are also performed to confirm the validity of the experimental data.

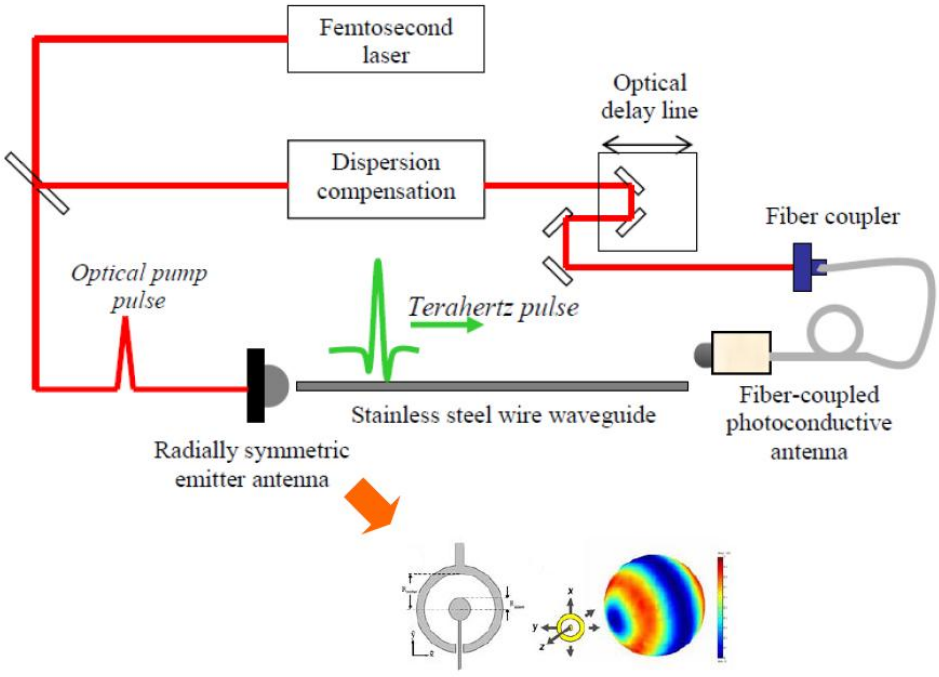


**Figure 6.2: Enhanced THz radiation coupling to metal wires using radial symmetric antennas** - the THz radial mode is directly emitted and coupled to the metal wire [42].

## 6.2 Experimental Setup

In the experiment, the segmented HWP mode converter and ZnTe(111) (as introduced in Chapter 5) were used to generate THz radial beam, because in the case of 800 nm excitation (Hurricane), the related THz amplitude from ZnTe(111) is larger than GaP(111).

The overall experimental setup is shown in Fig.6.3. A THz time-domain spectroscopy (THz-TDS) setup was employed for this investigation. The light source was Hurricane, and polarized along $x$ axis in Fig.6.3. The laser beam was divided into two by a beam sampler; a part with 99% of the total power served as a pump beam and passed through the segmented HWP mode converter to generate a radially polarized THz beam, which was then focused by a THz lens with a 50 mm focal length (Tsurupica, Pax Corp.). The beam size was 10 mm in diameter on the segmented HWP. A straight copper wire with a length of 20 cm and a radius of 0.5 mm was fixed in two polytetrafluoroethylene (PTFE) holders, with one end being placed at the focal point of the lens. At the other end of the copper wire, a photo-conductive antenna was placed for THz detection and the other part of the laser beam (1% of the total power) was introduced as a probe beam. By changing the time delay between the pump pulse and the probe pulse, THz waveforms in the time domain were obtained. In the experiments, a commercial photo-conductive antenna with a 5 micron gap was used. With the gap lying along $x$ or $y$ directions, $x$ or $y$ electric fields of THz wave were detected, respectively. That allowed the detection of all in-plane electric field components of the THz field by changing the in-plane direction of the antenna. In the setup, the probe beam was expanded to a spot with about 20 mm diameter, so the antenna can be moved in that area to scan the THz electric field distribution. Here, a $21 \times 21$ point area is scanned with a resolution of 0.25 mm×0.25 mm. The experimental setup was purged with dry nitrogen gas to prevent absorption of the beams by water vapor.

To experimentally investigate the in-coupling efficiency, antenna scanning was also performed at the in-couple plane (Fig.6.3), with the copper wire removed from the setup, as shown in Fig.6.4. Information about the coupling efficiency is obtained from these two scanning results.

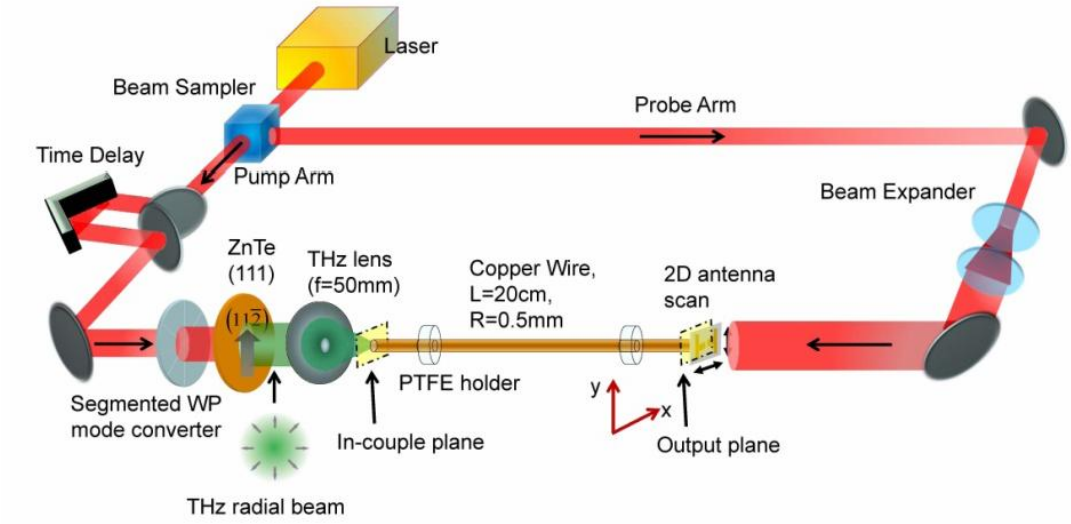


**Figure 6.3: Experimental setup of the metal wire waveguiding** - Segmented HWP and ZnTe(111) were used to generate THz radial beam [78].

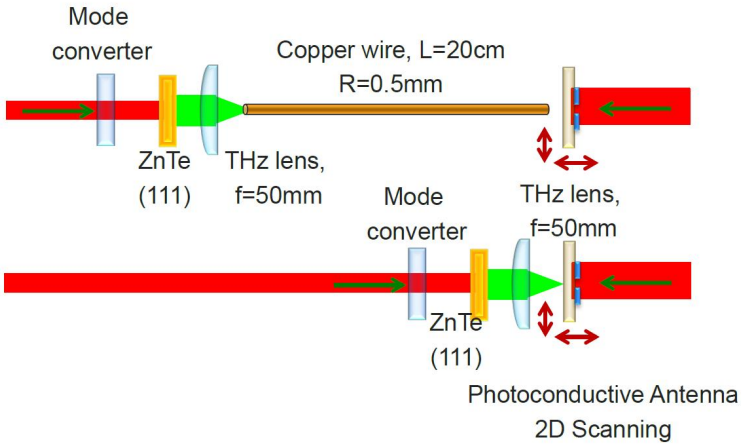


**Figure 6.4: Experimental setup of the metal wire waveguiding** - upper: the setup of scanning output data with the copper wire; lower: the setup of scanning input data with the copper wire removed.

## 6.3 Results and Analysis

Figure 6.5 shows the distribution of THz intensity, which is integrated in time domain ($I(x,y) = \int[E_x^2(x,y,t) + E_y^2(x,y,t)]dt$, $E_z$ can not be detected with the antenna). This image is obtained at the output plane (Fig.6.3) where a donut-shaped electric field distribution is clearly observed. Examples of THz waveforms measured at offsets in $y$ axis of +1.2 mm and −1.2 mm from the central dark point (marked as stars in Fig.6.5(a)) are shown in Fig.6.5(b). It should be noted that the phases are opposite at these two places, confirming that the guiding mode is radially polarized.

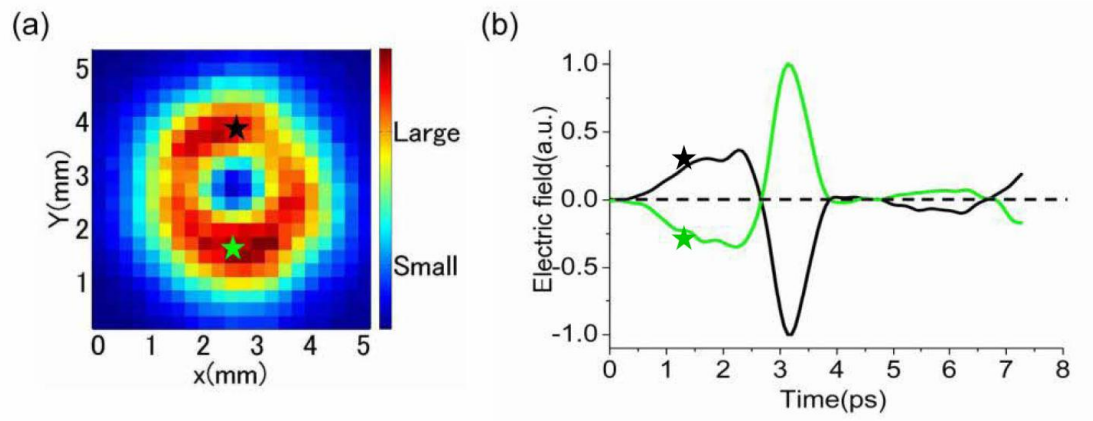


**Figure 6.5: Waveguide mode at the output plane** - (a) Intensity distribution at the output plane. (b) Waveforms at $y$ offset positions of +1.2 mm and −1.2 mm from the center (marked as stars in Fig.6.5(a)) [78].

In Fig.6.6, waveforms (electric fields as functions of time) and spectra in the THz frequency domain of the in-couple plane (black) and output plane (red) are shown. These four graphs are normalized at the peak values. The obtained output plane spectrum [red line in Fig.6.6(a)] is observed over a frequency range of up to about 1.5 THz, which is about three times broader than the previously reported results in which the maximum frequency was only about 0.5 THz [43, 51, 122, 123, 126].

To classify the advantage of the combination of a metal wire with a THz radial beam, two reference measurements were undertaken, the setups are shown in Fig.6.7, and the results are shown in Fig.6.8. In Fig.6.8(a), at the same position at the output plane, the black line shows the THz waveform with the copper wire waveguide,

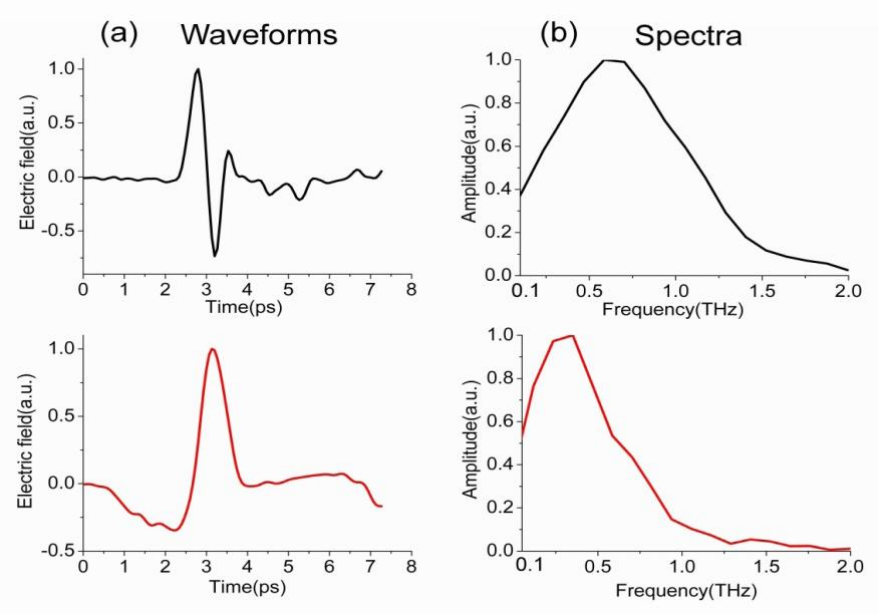


**Figure 6.6: Normalized waveforms (a) and spectra (b)** - Upper (black): In-couple plane; Lower (red): Output plane [78].

while the red line shows the waveform with the copper wire removed from the setup. In Fig.6.8(b), the black line represents the maximum electric field waveform with a radially polarized beam in-coupled, and the red line shows the maximum electric field waveform with an azimuthally polarized beam in-coupled (with the ZnTe(111) crystal rotated by 90°). Comparing these data, the following can be concluded:

1. Only the radially polarized mode is supported on the copper wire. The azimuthally polarized beam cannot be coupled to the wire.

2. The freely propagating THz electric field is at least one order of magnitude smaller than the guiding field.

Another group of measurements had been taken, with a 15 cm copper wire replacing the 20 cm copper wire, the radius of the wires are the same (0.5 mm), as shown in Fig.6.9, the measured waveforms are $E^{15cm}(t)$ (red line) and $E^{20cm}(t)$ (black line), as shown in Fig.6.10. Because in these two measurements, the detection antenna stays in the exactly same position, and the time delay line is also unchanged, so the time origin of these two measurements are completely the same, then by directly comparing Fourier transformation of the waveforms at the output plane of the two different copper wires $\{\tilde{E}^{20cm}(\omega) = FT[E^{20cm}(t)]$ and $\tilde{E}^{15cm}(\omega) = FT[E^{15cm}(t)]\}$, the amplitude at-

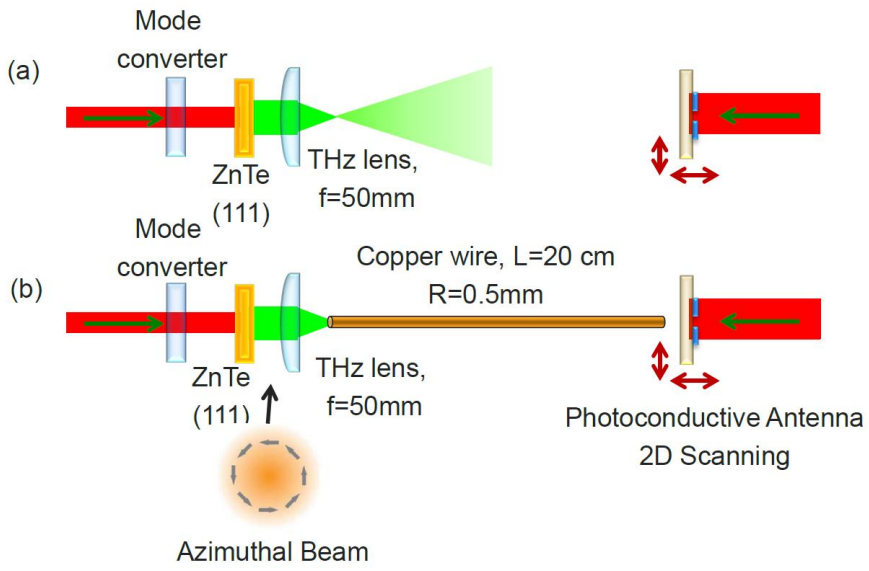


**Figure 6.7: Setups of reference measurements** - (a) the copper wire is removed from the setup; (b) by rotating the ZnTe(111) by 90°, the in-couple mode is changed to an azimuthal beam.

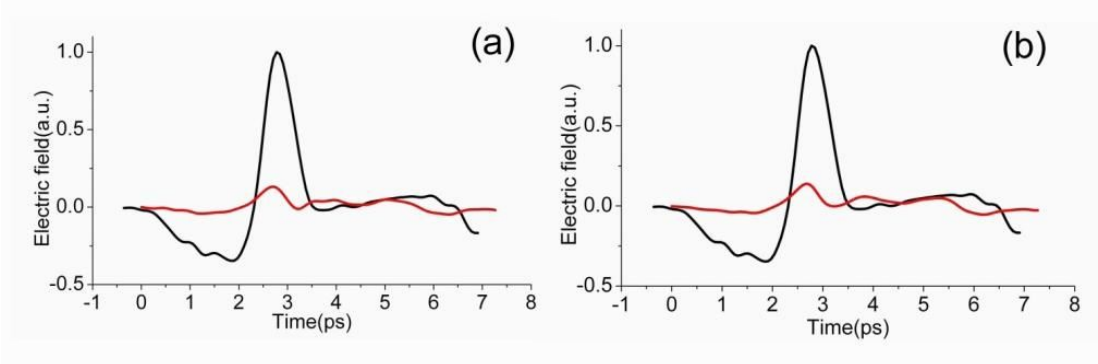


**Figure 6.8: Reference waveforms** - Black lines: waveforms of a guided THz electric field at the output plane. Red lines: (a) waveform measured with the copper wire removed from the setup, (b) waveform with the azimuthally polarized mode in-coupled [78].

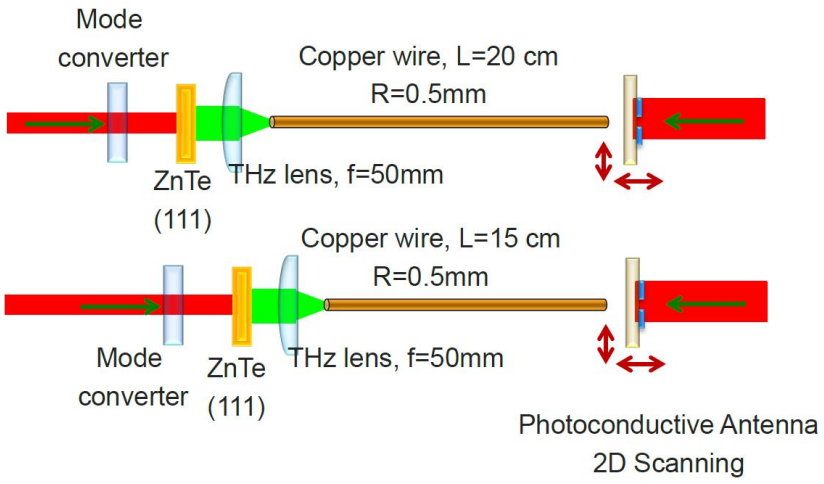


**Figure 6.9: Setups of 15 cm and 20 cm copper wires measurements** - In these two measurements, to ensure the absolute phase dispersion can be extracted, the antenna and the time delay line are keeping totally the same status.

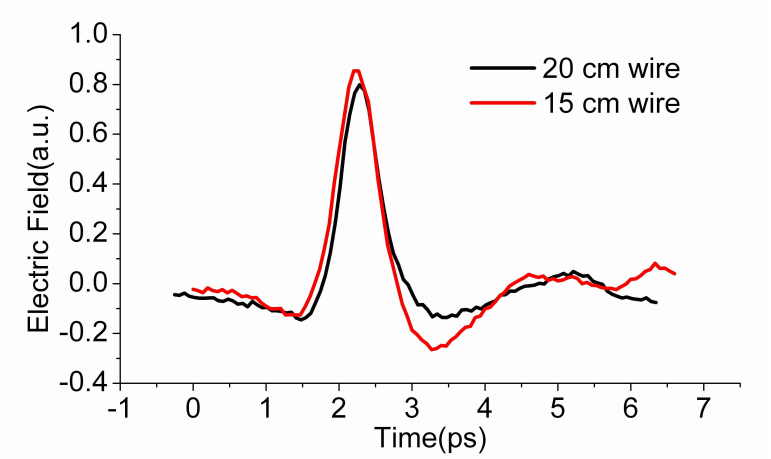


**Figure 6.10: Waveforms after 15 and 20 cm copper wire propagation** - Red: waveform after 15 cm copper wire; Black: waveform after 20 cm copper wire.

tenuation rate and the phase dispersion of the wire guiding mode can be extracted through eq.6.1 (where $\alpha$=Attenuation coefficient, c is the speed of light, $\Delta l$= 5 cm, $\omega = 2\pi f$):

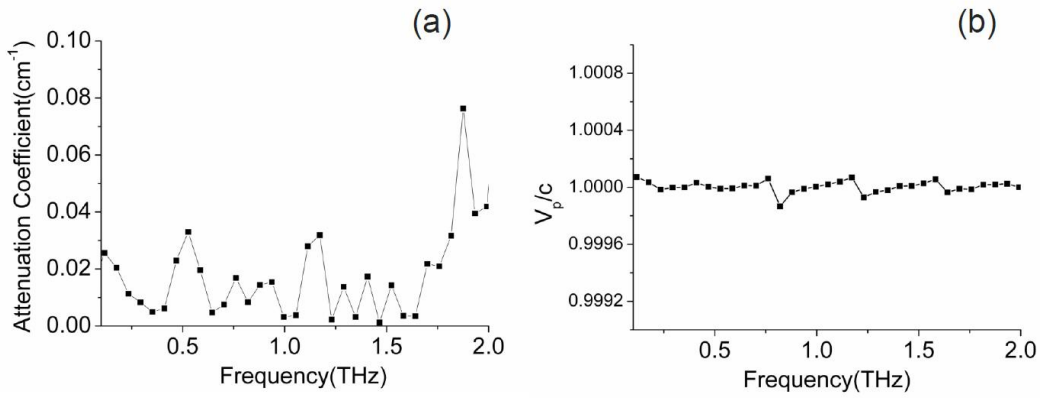


**Figure 6.11: Amplitude attenuation coefficient and phase velocity dispersion of the waveguiding mode** - The data are extracted from the waveforms shown in Fig.6.10.

$$\frac{\tilde{E}^{20cm}(\omega)}{\tilde{E}^{15cm}(\omega)} = \exp(-\frac{\alpha}{2}\Delta l)\exp\left[i\omega\Delta l\left(\frac{1}{v_p}-\frac{1}{c}\right)\right], \tag{6.1}$$

the results are shown in Fig.6.11. From the plots, it has been proved the advantages that low-attenuation and low-dispersion of bare metal wire waveguiding is available in a larger spectral range (up to 2 THz) in comparison with earlier results [122].

To determine the in-coupling efficiency of our method, we meshed both the in-coupled and output planes into $11 \times 11$ grids; in order to reduce the scanning time, we decreased the scanning grid number here in comparison with $21 \times 21$ grids used for measuring the field distribution. Then, at each grid, the THz field $\mathbf{E}_{i,o}(x, y, t)$ was measured (subscript $i$ and $o$ represent in-coupled and output planes, respectively), and a Fourier transformation was performed as follows: $\mathbf{E}_{i,o}(x, y, t) \overset{\text{FT}}{\rightarrow} \mathbf{E}_{i,o}(x, y, \omega)$. Subsequently, the frequency dependence of the in-coupled and output energies were determined by integrating the in-coupled and output planes, respectively: $I_{i,o}(\omega) = \iint dxdy|\mathbf{E}_{i,o}(x, y, \omega)|^2$. Then, the frequency dependence of the coupling efficiency was calculated using $\eta(\omega) = I_o(\omega)/I_i(\omega)$, the results of which are shown in Fig.6.12 (black solid line). From Fig.6.12, it can be seen that the maximum coupling efficiency is as high as 66% at approximately 0.3 THz, while a total efficiency ($\eta = \int I_o(\omega)d\omega/I_i(\omega)d\omega$)

of 17% is found when the propagating THz radial mode energy is coupled to the copper wire. This maximum value is about two orders of magnitude larger than the coupling efficiency measured using the scattering coupling method [122], and slightly higher than the estimated coupling efficiency determined using the antenna-coupling method described in ref.[42].

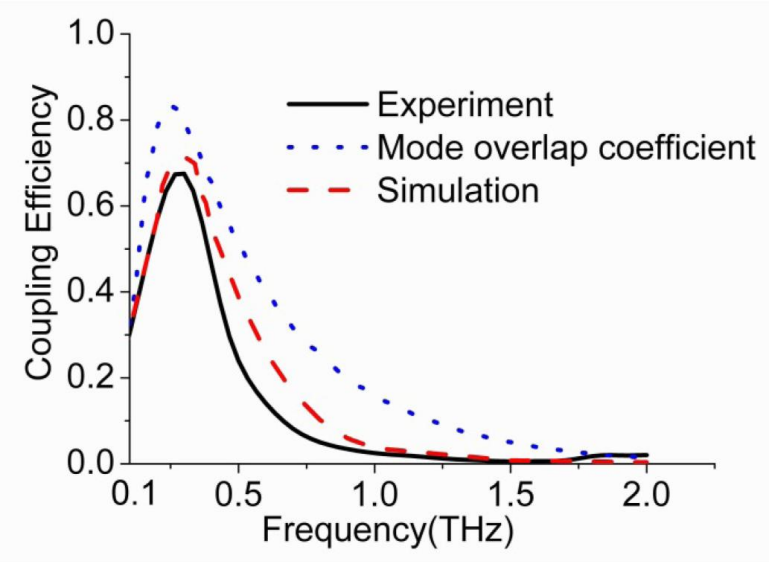


**Figure 6.12: Frequency dependence of the coupling efficiencies** - obtained by experiment, mode-overlap calculation and numerical simulation [78].

To confirm the validity of the experimental values of coupling efficiency, we calculate the mode-overlap coefficient between the in-coupling focused radially polarized field and the guiding Sommerfeld mode. The in-plane electric field of the focused radially polarized beam can be expressed in a cylindrical coordinate system as [30, 127]:

$$E_r(\omega, \rho) \propto \int_0^{\theta_{max}} \cos^{1/2}\theta \sin(2\theta) E_0(\theta) J_1(k_0 \rho \sin\theta) d\theta, \tag{6.2}$$

where $\rho$ is the distance from the optical axis, $\theta$ is the angle that the ray makes with the axis, $\theta_{max}$ is the maximum value of that corresponds to half of the aperture angle determined by the numerical aperture (NA) (in our case, NA = 0.1), $E_0(\theta)$ is the electric field distribution before focusing lens [in the mode overlap calculations, a top-hat distribution of $E_0(\theta)$ was assumed, as shown in Fig.6.13(a); in the numerical simulations using a commercially available program package (CST Micro Wave Studio),

the relative $E_0(\theta)$ is shown in Fig.6.13(b)], $k_0 = \omega/c$ is the wavenumber, and $J_1(x)$ is a Bessel function of the first kind. Because in-plane component is much larger than the longitudinal component $E_z$, in this case, only in-plane component is considered here.

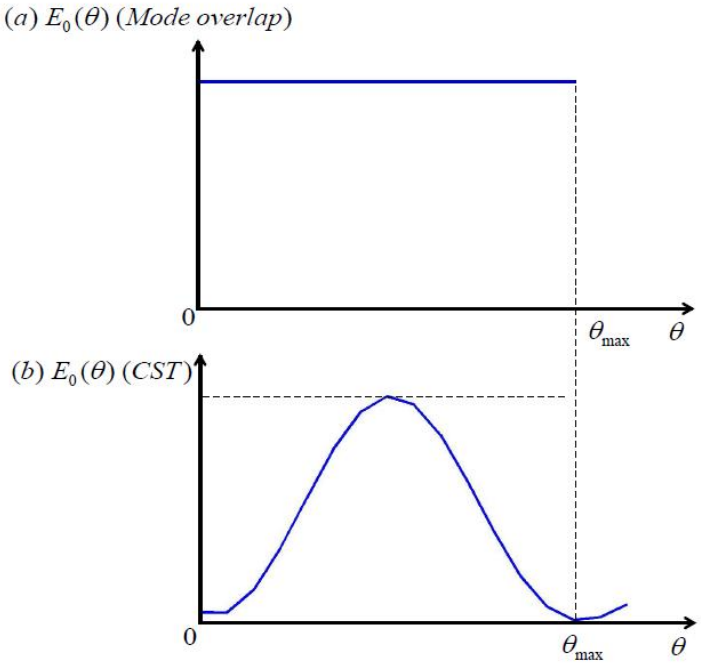


**Figure 6.13: $E_0(\theta)$ in the mode overlap calculations and CST simulations** - (a) $E_0(\theta)$ in the mode overlap calculations; (b) $E_0(\theta)$ in the CST simulations.

Sommerfeld wave guiding on the copper wire can be described by a Hankel function $H^{(1)}(\gamma\rho)$, where $\gamma$ is defined in terms of the propagation constant $k$ ($k \approx \frac{\omega}{c} + i\frac{\omega^2}{2c^3\mu\sigma}$, for a thick copper wire, $\mu$=1, $\sigma$=5.96×10$^7$S·m$^{-1}$ [5]) of the field outside the wire according to $\gamma^2 = (\omega/c)^2 - k^2$[122] and inside the metal, because the relative permittivity of metal is far larger than 1. Hence, the modal field will decay very fast; in fact, it can penetrate into the metal side for only 1 $\mu$m or less [128]. Therefore, the modal field on the copper wire is a hollow-cored mode. The size of the hollow core is determined by the radius of the metal wire $R$, which can be expressed as follows:

$$E_{\text{Sommerfeld}}(\rho) \propto \begin{cases} H_1^{(1)}(\gamma\rho) & (\rho > R) \\ 0 & (\rho < R) \end{cases} . \tag{6.3}$$

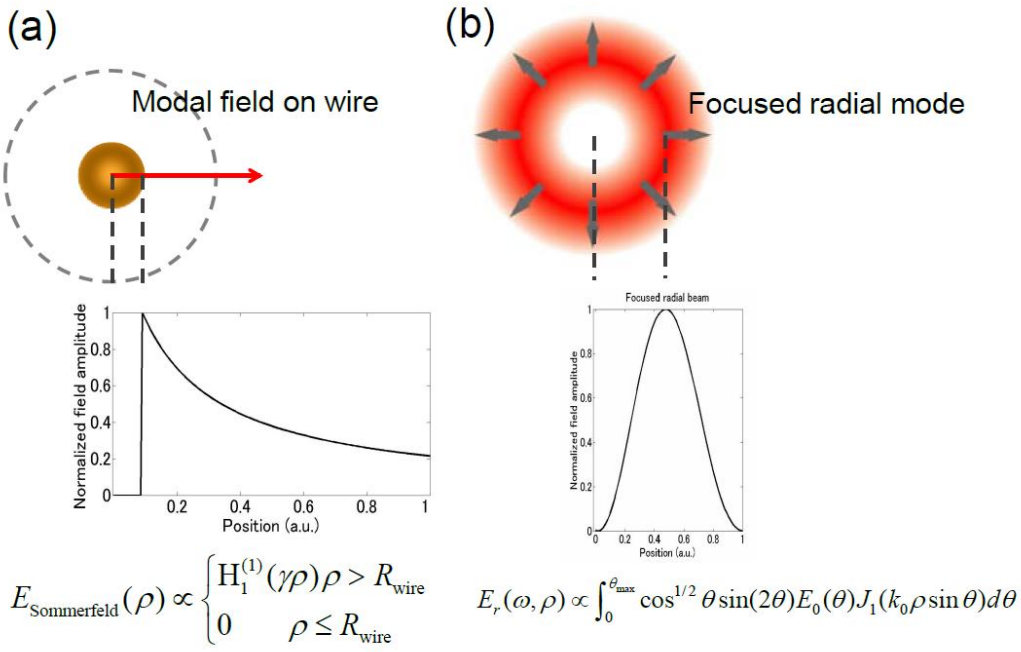


**Figure 6.14: The focused radial mode and the Sommerfeld mode** - (a): Sommerfeld mode, where $\gamma$ is defined in terms of the propagation constant $k$ ($k \approx \frac{\omega}{c} + i\frac{\omega^2}{2c^3\mu\sigma}$, for a thick copper wire, $\mu$=1, $\sigma$=5.96×10$^7$S·m$^{-1}$ [5]) of the field outside the wire according to $\gamma^2 = (\omega/c)^2 - k^2$[122], in the figure, normalized absolute values are plotted, to show the amplitude decay out the metal wire; (b): focused radial mode.

The focused radial mode and the Sommerfeld mode are shown in Fig.6.14, then, the mode-overlap coefficient is defined by the integration [129, 130]:

$$\eta(\omega) = \frac{|\int E_r(\omega) E^*_{\text{Sommerfeld}} \rho d\rho|^2}{\int |E_r(\omega)|^2 \rho d\rho \int |E_{\text{Sommerfeld}}|^2 \rho d\rho}, \tag{6.4}$$

in the calculations, to account for the finite aperture size of real optical systems, the integration is performed in an area with 3.2 mm width (The integration area is determined by measuring the actual beam diameter, in another word, the aperture stop of the actual optical alignments; moreover, slightly increase or decease the integration area will not affect the calculation results much). The calculated result is shown in Fig.6.12 (blue dotted line).

Numerical simulations performed by a commercially available program package (CST Micro Wave Studio) were also applied to determine the coupling efficiency. In the simulation, a model replicating the experimental setup was built. The NA of the focusing lens and the metal wire radius were set to 0.1 and 0.5 mm, respectively, in a frequency range of 0.1-2 THz using a 0.1 THz step size. The field distributions were inspected and the energies passing through the input and output planes of the metal wire were integrated; the ratio of the incident energy and the output energy gives the coupling efficiency. The results of this simulation are shown by the red dashed line in Fig.6.12. One can see that the numerical simulation result reproduces the experiment data well. The mode-overlap calculation also qualitatively supported the experimental and numerically simulated results, but some deviations were observed, especially in the higher frequency region. The main factors contributing to this discrepancy would be the nearly 10% propagation loss in the frequency range higher than 0.5 THz in the 20 cm copper wire [51, 122] and losses at the PTFE holder surfaces (reported to be $< 3\%$).

Moreover, in the calculation of mode-overlap coefficient, it should be noted that the frequency dependence of the coupling efficiency $\eta(\omega)$ is indeed dependent on two parameters: NA of the focusing (depending on $\theta_{max}$ in eq.6.2) and the metal wire radius $R$. By changing one of these two parameters while leaving the other unchanged, the relationship between the $\eta(\omega)$ and the parameters $R$ and NA was investigated; some results are shown in Fig.6.15. In the case where the metal wire radius is constant and set to $R$=0.5 mm [Fig.6.15(a)], when NA becomes smaller, the peak frequency of

coupling efficiency shifts to higher frequencies, while the bandwidth of the coupling efficiency obviously broadens. In the case where the NA of the focusing lens is held at a constant value of 0.1 [Fig.6.15(b)], as the wire radius decreases, the peak coupling efficiency starts to decrease and shifts to higher frequencies when the radius becomes smaller than approximately 0.03 mm.

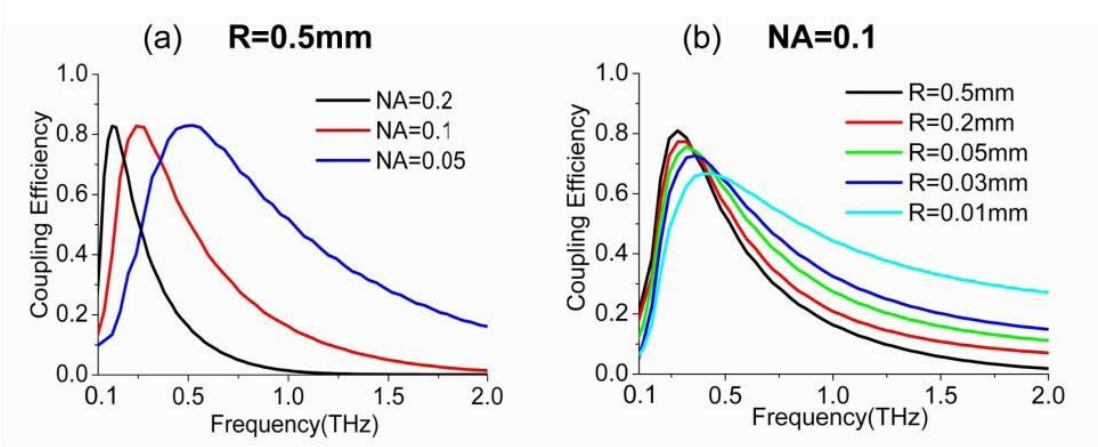


**Figure 6.15: Frequency dependence of mode-overlap calculation** - (a) wire radius $R$ = 0.5 mm, NA = 0.2, 0.1, and 0.05; (b) NA = 0.1, wire radius $R$ = 0.5 mm, 0.2 mm, 0.05 mm, 0.03 mm, and 0.01 mm[78].

Considering these results, it is possible to tune the frequency dependence of the coupling efficiency by choosing an appropriate NA. In particular, it is effective to use a small NA in order to achieve efficient coupling in a higher and broader frequency range, which could be important for many applications of THz technology, such as biomedical imaging [131, 132], THz tomography, and quality control [133].

In our experimental results of energy coupling coefficient, we did not consider the losses of interface reflection at the input and the output ends of the metal wires, and the attenuation on the metal wires. Nevertheless, according to our results shown in Fig.6.11, both the interface reflection and the propagation attenuation can be evaluated. For attenuation, the loss can be straightforwardly decided by the attenuation coefficient shown in Fig.6.11 (a); and for interface reflection, the loss is determined by the Fresnel's Law: $R = \left(\frac{n_1-n_2}{n_1+n_2}\right)^2$, where $R$ is the reflection rate, $n_1$ and $n_2$ are the relative refraction index of free space mode and the waveguiding mode, respectively, in fact, for light in air, $n_1$ is 1, and for waveguiding mode, $n_2$ is determined by the phase velocity

dispersion, $n_2 = \frac{c}{v_p}$, we can find this number in Fig.6.11 (b), it is very close to 1, so the interface reflection is negligible.

Based on these discussions, it can be concluded that in our setup, the energy transferring coefficient of the bare metal wire waveguides mainly depends on the mode-overlap between the focused radial beams and the modal modes on the metal wires. For an intuitive picture of the mode-overlap, we can consider a metal wire with very large radius, in this case, it is obvious that the focal size of high frequency ingredients will be much smaller than the wire size, so they will be reflected by the metal wall. To improve the mode-overlap coefficient, we are now considering to in-couple the radial beams to the tip end of a tapered wire, because for a tapered tip, it is possible that all frequency ingredients can find a good mode-overlap at the positions of different radius, simulations are in performing to check this point.

In conclusion, to employ a convenient method for generating broadband and stable THz vector beams, we demonstrated directly focusing and coupling THz radial beams to a bare copper wire with high efficiency. By applying an antenna scanning THz-TDS setup, the radially polarized guiding Sommerfeld wave was confirmed. The guiding spectra had a wide bandwidth, extending as high as 1.5 THz, which is about three times wider than the previously reported results [43, 51, 122, 123, 126]. The frequency dependence of the energy coupling efficiency was determined by a comparison between the input and output energies, and a sufficient coupling efficiency of 66% at 0.3 THz was obtained; this represents an improvement of two orders of magnitude in comparison with the reported experimental results. In total, 17% of the input energy is coupled to the copper wire. Mode-overlap calculation and numerical simulation of coupling a propagating radially polarized mode of the THz beam to a metal wire were performed, and the calculated coupling efficiency matched well with the experimental data. It was shown via mode-overlap calculation that the magnitude and bandwidth of the in-coupled frequency could be greatly increased by optimizing the parameters of the focusing lens, where using smaller NA lens led to vastly broadened bandwidths. This coupling method is a promising technique for the development of new THz manipulation technologies, which is beneficial for the development of various THz applications [105, 134, 135].

## 6.4 Simulation Results of Several Structures Based on Metal Wire Waveguiding

Based on the efficient coupling to bare metal wire waveguides, a near-field probe is proposed to achieve sub-wavelength THz imaging. As reported in ref.[122] and ref.[105], based on bare metal wire THz waveguiding, splitters can be realized; while tips can be manufactured to achieve sub-wavelength near-field focusing. These results are also confirmed in our simulations using a commercially available program package (CST Micro Wave Studio), as shown in Fig.6.16 and Fig.6.17.

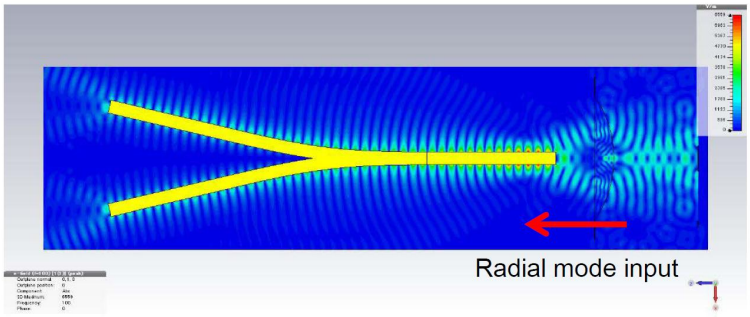


**Figure 6.16: Schema of THz splitter simulation** - the simulation is performed with CST Micro Wave Studio, in the simulation, a waveguide port is set to generate THz radial beam, the radial beam is focused to a copper wire (diameter 1 mm) connected to a splitter, the figure shows the field distribution at 0.1THz.

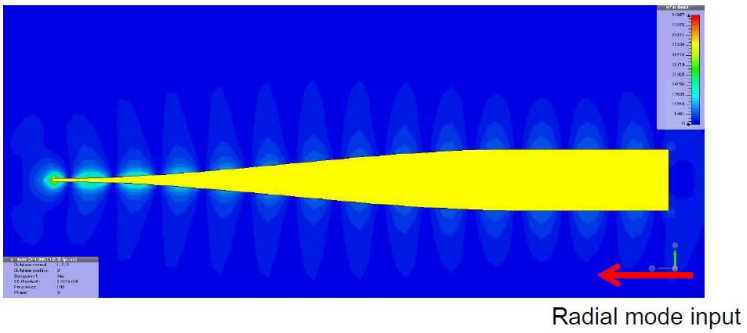


**Figure 6.17: Schema of tip focusing simulation** - the simulation is performed with CST Micro Wave Studio, in the simulation, a THz radial beam is focused to a tapered copper wire (diameter 1 mm), the diameter of the tip is 50 $\mu$m, the figure shows the field distribution at 0.1 THz.

We did a series of simulation to check the splitters, the setup is shown in Fig.6.18. In these simulations, the radius of the wire is 0.5 mm, the length of the bending arc (L) of the splitter is constantly 50 mm, and we adjust the radius of the bending arc (R) from 50 mm to 150 mm, the ratio between input amplitudes and output amplitudes at 0.1 THz ($E_{out}/E_{in}$) is shown in Fig.6.19, from the figure, we find when R is larger than 120 mm, the ratio is as high as 55%.

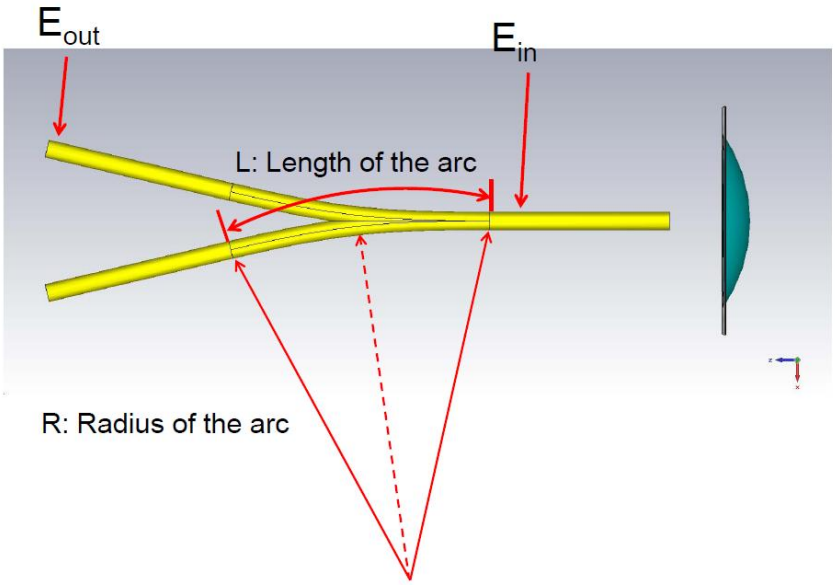


**Figure 6.18: The setup of parameters of the splitter** - L is constantly 50 mm, while R is from 50 mm to 150 mm.

And in the tip simulations, the radius of the wire is 0.5 mm, and the radius of the tip is 0.05 mm, the field is one order enhanced at the tip in comparison with on the wire; at the tip, both in-plane electric component ($E_\rho$) and longitudinal component ($E_z$) exist, as shown in Fig.6.20.

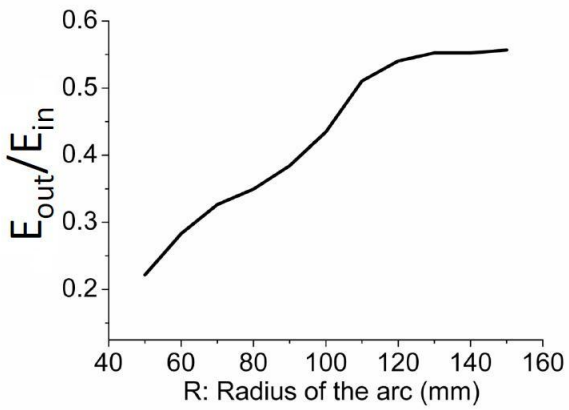


**Figure 6.19: the ratio between input amplitudes and output amplitudes at 0.1 THz ($E_{out}/E_{in}$)** - when R is larger than 120 mm, the ratio is as high as 55%.

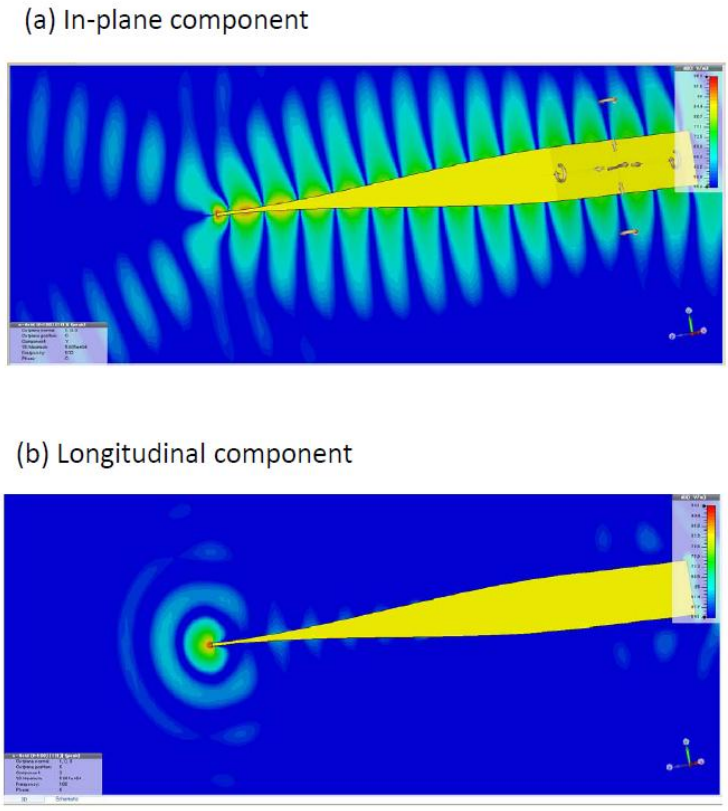


**Figure 6.20: Field enhancement and distribution at the tip** - (a) in-plane electric component ($E_\rho$); (b) longitudinal component ($E_z$).

Combining a splitter and a tip, a near-field probe is designed for THz sub-wavelength imaging. The setup is shown in Fig.6.21, THz radial beam inputs from one end of the splitter, and propagates to the tip end; our consideration is, if we set a metal sample with a rough surface (for example, a coin) near the tip, and if the amplitude of reflected THz signal detected from the other end of the splitter strongly depends on the roughness of the metal surface, then near-field imaging is possible through this probe. To confirm this, we performed simulations with a commercially available program package (CST Micro Wave Studio).

In the first step, we performed simulations to confirm when we use a golden mirror as the sample, and we change the distance from the tip to the golden mirror, how the reflection signal varies. As shown in Fig.6.21, in the simulations, the length of the bending arc is 50 mm, and the radius of the arc is 100 mm; we set two field probes at place *a* and *b* to monitor the input and reflected signals, and *D* is the distance from the tip to the golden mirror. In all the simulations below, the spectral range is set to be 0-0.2 THz.

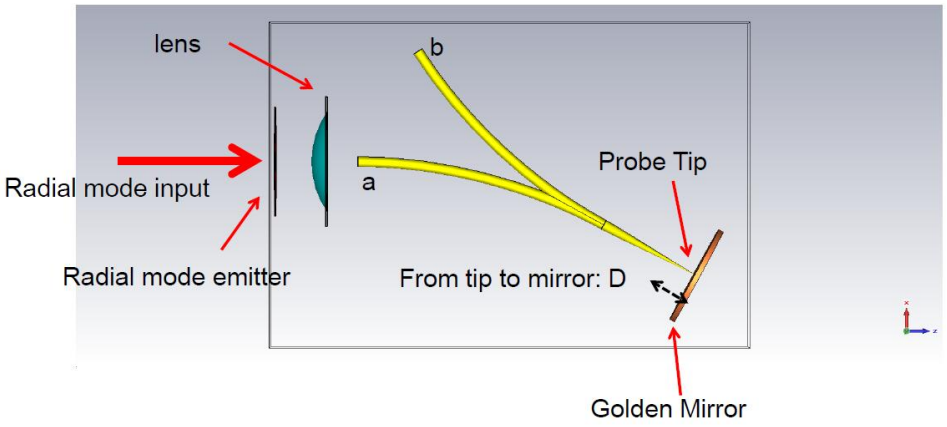


**Figure 6.21: Schematic of near-field probe simulations** - probes *a* and *b* are for monitoring the input and reflected signals, *D* is the distance from the tip to the golden mirror, the simulation spectral range is 0-0.2 THz.

The results of different *D* are shown in Fig.6.22, the waveforms at position *b* in Fig.6.21 are listed. From the simulation curves, we find the amplitude of the reflected THz signals suffers from a dramatical falloff when *D* becomes larger. Actually, when the tip is near to the golden mirror ($D$=10 $\mu$m), shown as the red line in Fig.6.22, the

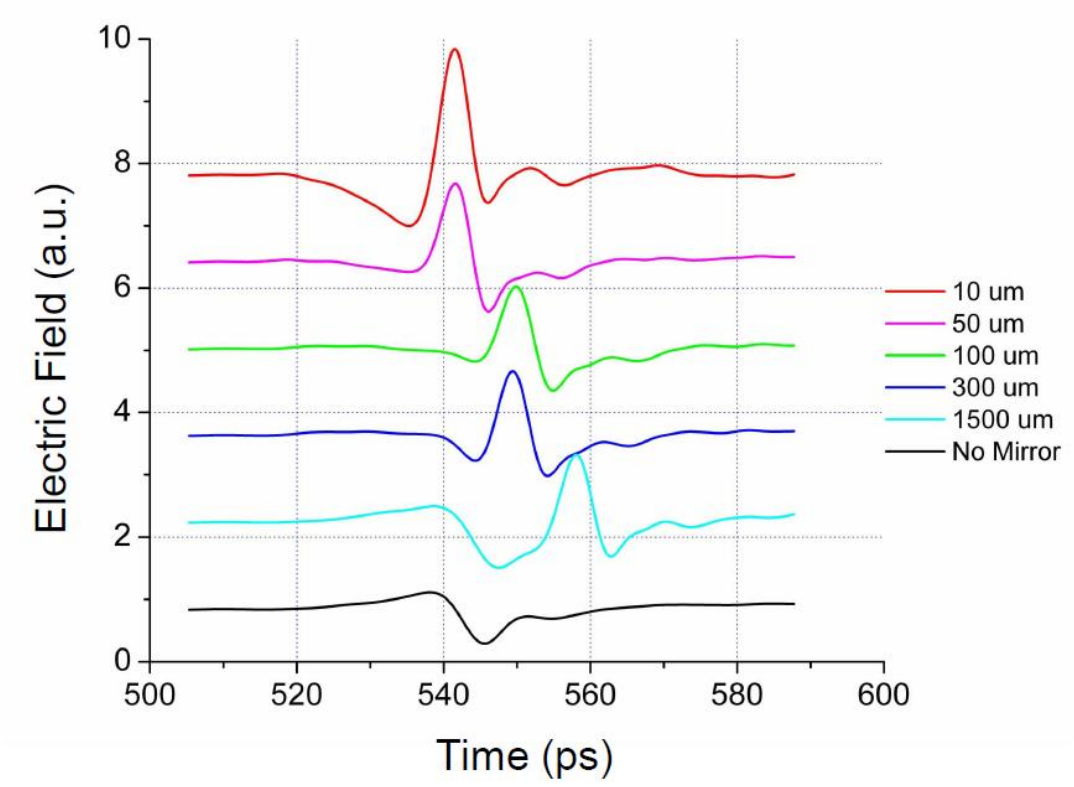


**Figure 6.22: Simulation results of different** $D$ - the reflected THz waveforms at position $b$ in Fig.6.21 are plotted, when $D$ is very small, i.e., the red line representing $D$=10 $\mu$m, the peak value of the waveform is about twice to signals of $D$ >100 $\mu$m.

peak of reflected signal is about twice larger than signals of $D$ >100 $\mu$m. If we remove the golden mirror in the setup, the reflected signal is shown as the black line in the figure.

From the results shown in Fig.6.22, we conclude that if we have a metal sample, on the surface of which there are sharp steps(height>~100 $\mu$m), it is possible to image this surface using our proposed THz probe. The advantage of this probe is benefitting from the near-field super focusing of the tip, the resolution of this probe is supposed to be sub-wavelength, this probe can be potentially used to detect metal samples in optically opaque media. Then in the second step, we performed simulations to confirm the resolution of this THz probe can achieve sub-wavelength scale. The setup is shown as Fig.6.23, a golden sample with a sharp step is used to test the probe, the sample moves in the direction indicated by the black dashed arrow. At the two side of the step, the distance from the tip to the metal surface is 10 $\mu$m and 200 $\mu$m, respectively, it also implies the height of the step is 190 $\mu$m.

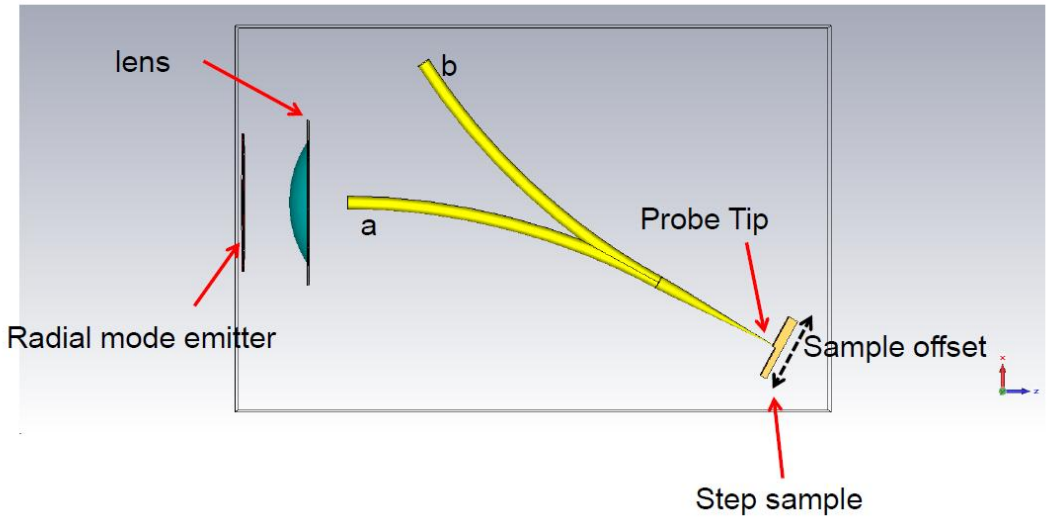


**Figure 6.23: Schematic of near-field probe simulations** - a step sample is used to check the resolution of the probe, the sample moves in the direction indicated by the black dashed arrow. At the two side of the step, the distance from the tip to the metal surface is 10$\mu$m and 200$\mu$m, respectively.

The simulations results are shown in Fig.6.24 and Fig.6.25. In Fig.6.24, the waveforms of 100 $\mu$m and -100 $\mu$m sample offsets from the step are shown, the contrast

is obvious, it straightforwardly confirms a 200 $\mu$m resolution of the near-field probe. And in Fig.6.25, similar results of 50 $\mu$m and -50 $\mu$m sample offsets are shown, the resolution as small as 100 $\mu$m is confirmed; and if we further decrease the number of sample offsets, the contrast of the waveforms will become ambiguous. Because in the simulation, the spectrum is set to be 0-0.2 THz, then the wavelength is ~3000 $\mu$m, so from the simulation results, the resolution is as small as $\lambda/30$, sub-wavelength imaging is confirmed.

Based on the simulation results, in the next step, the experiments reproducing the simulation setups are planned.

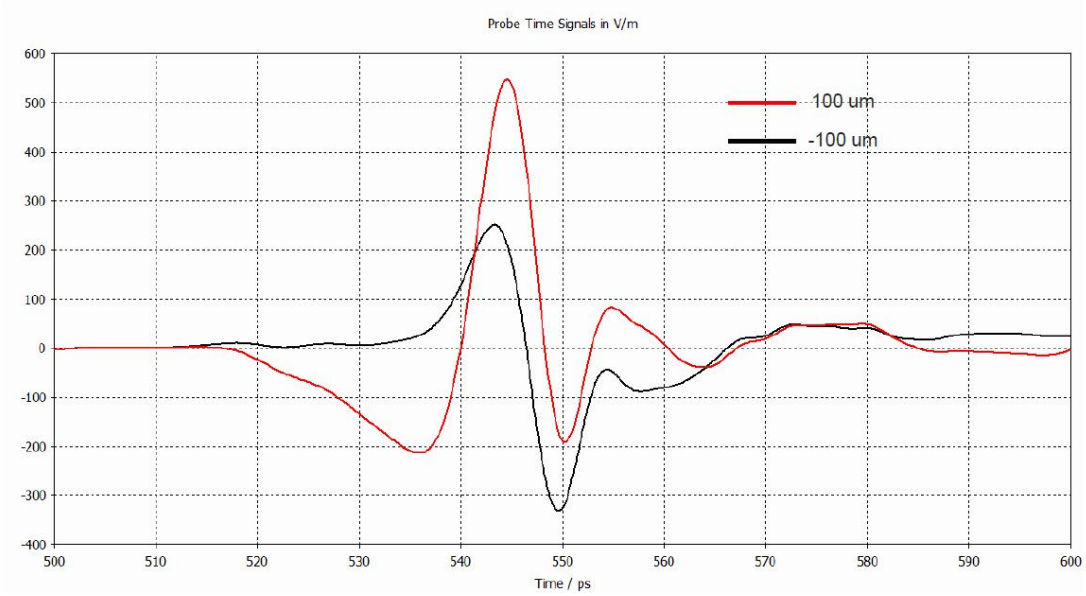


**Figure 6.24: Simulation results of 200 $\mu$m resolution** - the red line indicates the signal at *b* of sample offset 100 $\mu$m from the center; the black line indicates the signal at *b* of sample offset -100 $\mu$m from the center.

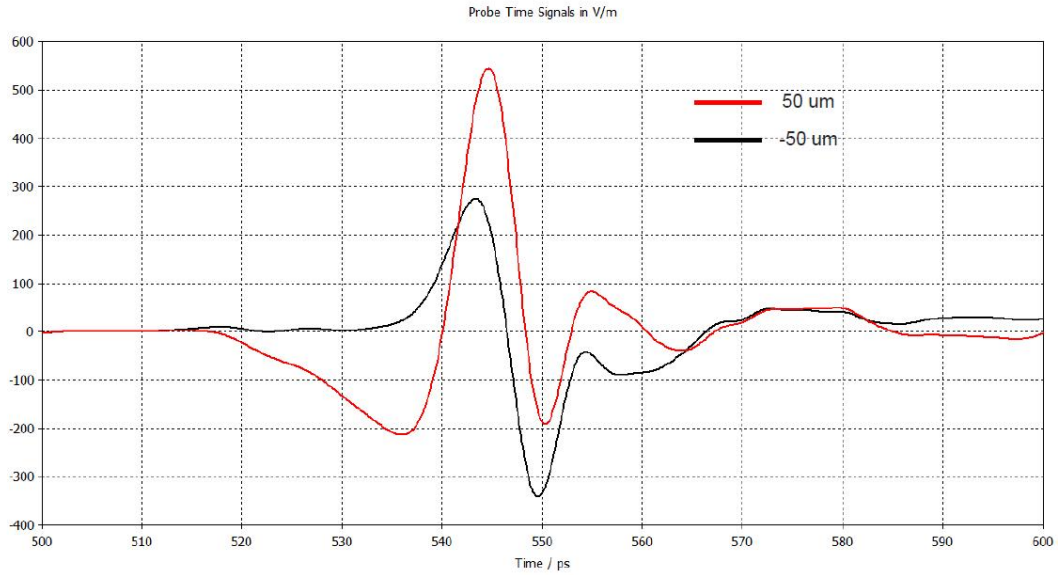


**Figure 6.25: Simulation results of 100 $\mu$m resolution** - the red line indicates the signal at $b$ of sample offset 50 $\mu$m from the center; the black line indicates the signal at $b$ of sample offset -50 $\mu$m from the center.

# Chapter 7

## Summarization and Prospects

Vector beams, due to their intriguing properties, are playing a vital role in modern optics. In this thesis, we introduced the concept of "vector beams" to the THz spectral range, we succeeded to generate and characterize THz vector beams, moreover, we applied THz radial beams in THz bare metal wire waveguides. In this last Chapter, a summarization of this thesis will be concluded.

In this thesis, we visited three topics: generation, characterization and application of THz vector beams.

**Generation of THz vector beams**

Employing nonlinear crystals possessing 3-fold rotational symmetry, an 8-piece segmented GaP(111) crystal and an 8-piece segmented half wave-plate(HWP) laser mode converter are designed and made to genearate radially and azimuthally polarized THz beams. In these two methods, eight-piece approximate devices are used, the generated THz vector beams are quasi-vector modes; however in the case of eight-piece elements are used, the mode overlap between an ideal vector beam and such quasi-vector beam was evaluated as large as 93%, such high number ensures the quality of the generated vector beams. Moreover, in comparison with reported generation methods of THz vector beams, the methods invented in this thesis hold the advantages that stable, broadband, simple in optical alignments and easy-switchable between the two fundamental vector modes (radially and azimuthally polarized THz beams).

**Characterization of THz vector beams**

In this thesis, THz camera and 2D THz-TDS measurements are implemented to analyze characteristics of the generated THz vector beams. In the measurements, we directly confirmed the focal features of in-plane and longitudinal electric components. The intensity distribution and local SoPs of the in-plane electric field were recorded, the donut shape and reversed waveforms strongly certificate the THz vector beams were successfully generated; the distribution of longitudinal electric field was obtained by building a 2D EO sampling setup, in which the detection crystal is ZnTe(100). Moreover, for the first time, the longitudinally polarized magnetic component in the focus of azimuthally polarized beams was experimentally characterized.

**Application of THz vector beams**

The generated THz radial beams are introduced to efficiently couple to bare metal wires, the experimentally determined data of energy coupling efficiency are shown for the first time, from the experimental data, the peak of energy coupling efficiency in our scheme is evaluated as 66%, which is two orders improved in comparison with the reported scattering in-coupling method. Moreover, from our experimental results, the advantages that low-attenuation and low-dispersion of bare metal wire waveguiding are proved to be available in a larger spectral range (up to 2 THz). This efficient coupling scheme is proposed to develop new THz elements and systems.

In the experiments of this thesis, three systems were employed to measure the THz field, they are THz camera, 2D PC antenna sampling setup, and 2D EO sampling setup. Here the advantages and limitations of these three systems are summarized as below:

- THz cameras are used to record the intensity distributions of THz electric field, real-time THz electric field profiles can be recorded in this case, however, for THz cameras, only intensity information can be obtained in the measurements, the waveforms (including amplitude, phase and spectrum information) can not be recorded.

- 2D PC antenna sampling setup is a time domain system, so the THz waveforms can be recorded in the measurements, but the measurements spend much more time than the THz cameras. In comparison with a 2D EO sampling setup, $E_z$ can not be detected with a 2D PC antenna sampling setup.

- 2D EO sampling setup is also a time domain system, so the THz waveforms can also be recorded in the measurements, in this system, ZnTe(100) can be used to detect $E_z$. However, because of the pump-probe geometry of this setup, 2D EO sampling line does not fit for characterizing the waveguiding modes, thus in the measurements of metal wire waveguiding, 2D PC antenna sampling setup was used.

# References


[1] R. Dorn, S. Quabis, and G. Leuchs. **Sharper Focus for a Radially Polarized Light Beam**. *Phys. Rev. Lett.*, **91**:233901, Dec 2003. 1, 8, 58, 59, 62, 86

[2] B. Jack, A. M. Yao, J. Leach, J. Romero, S. Franke-Arnold, D. G. Ireland, S. M. Barnett, and M. J. Padgett. **Entanglement of arbitrary superpositions of modes within two-dimensional orbital angular momentum state spaces**. *Phys. Rev. A*, **81**:043844, Apr 2010. 1

[3] Ebrahim Karimi, Jonathan Leach, Sergei Slussarenko, Bruno Piccirillo, Lorenzo Marrucci, Lixiang Chen, Weilong She, Sonja Franke-Arnold, Miles J. Padgett, and Enrico Santamato. **Spin-orbit hybrid entanglement of photons and quantum contextuality**. *Phys. Rev. A*, **82**:022115, Aug 2010. 1

[4] Qiwen Zhan. **Cylindrical vector beams: from mathematical concepts to applications**. *Adv. Opt. Photon.*, **1**(1):1–57, Jan 2009. 1, 6, 50

[5] Yun-Shik Lee. *Principles Of Terahertz Science And Technology*. Springer, 2009. 2, 3, 12, 14, 15, 23, 107, 108

[6] D. Dragoman and M. Dragoman. **Terahertz fields and applications**. *Progress in Quantum Electronics*, **28**(1):1 – 66, 2004. 17, 19

[7] Tonouchi Masayoshi. **Cutting-edge terahertz technology**. *Nat. Photon.*, **1**(1):97–105, Feb 2007.

[8] Ulbricht Ronald, Hendry Euan, Shan Jie, Heinz Tony F., and Bonn Mischa. **Carrier dynamics in semiconductors studied with time-resolved terahertz spectroscopy**. *Rev. Mod. Phys.*, **83**:543–586, Jun 2011. 3

[9] P.H. Siegel. **Terahertz technology**. *Microwave Theory and Techniques, IEEE Transactions on*, **50**(3):910–928, 2002. 3

[10] M. Nagel, P. Haring Bolivar, M. Brucherseifer, H. Kurz, A. Bosserhoff, and R. Buttner. **Integrated THz technology for label-free genetic diagnostics**. *Applied Physics Letters*, **80**(1):154–156, 2002. 3

[11] T. Kleine-Ostmann, K. Pierz, G. Hein, P. Dawson, and M. Koch. **Audio signal transmission over THz communication channel using semiconductor modulator**. *Electronics Letters*, **40**(2):124–126, 2004. 4

[12] Radoslaw Piesiewicz, Jaouhar Jemai, Martin Koch, and Thomas Kurner. **THz channel characterization for future wireless gigabit indoor communication systems**. pages 166–176, 2005. 4

[13] Naoki Oda. **Uncooled bolometer-type Terahertz focal plane array and camera for real-time imaging**. *Comptes Rendus Physique*, **11**:496 – 509, 2010. 4

[14] M. Bolduc, M. Terroux, L. Marchese, B. Tremblay, E. Savard, M. Doucet, H. Oulachgar, C. Alain, H. Jeronimek, and A. Bergeron. **THz imaging and radiometric measurements using a microbolometer-based camera**. In *Infrared, Millimeter and Terahertz Waves (IRMMW-THz), 2011 36th International Conference on*, pages 1–2, 2011. 4

[15] Robert Chau, Brian Doyle, Jack Kavalieros, Doug Barlage, Anand Murthy, Mark Doczy, Reza Arghavani, and Suman Datta. **Advanced depleted-substrate transistors: single-gate, double-gate and tri-gate**. *SOLID STATE DEVICES AND MATERIALS*, pages 68–69, 2002. 4

[16] D. H. Auston, K. P. Cheung, and P. R. Smith. **Picosecond photoconducting Hertzian dipoles**. *Applied Physics Letters*, **45**(3):284–286, 1984. 4, 11

[17] L. Xu, X.-C. Zhang, and D. H. Auston. **Terahertz beam generation by femtosecond optical pulses in electro-optic materials**. *Applied Physics Letters*, **61**(15):1784–1786, 1992. 4

[18] Dieter Pohl. **Operation of a Ruby Laser in the Purely Transverse Electric Mode $TE_{01}$**. *Applied Physics Letters*, **20**(7):266–267, 1972. 6, 7, 8, 47

[19] E. SNITZER. **Cylindrical Dielectric Waveguide Modes**. *J. Opt. Soc. Am.*, **51**(5):491–498, May 1961. 6

[20] Y. Mushiake, K. Matsumura, and N. Nakajima. **Generation of radially polarized optical beam mode by laser oscillation**. *Proceedings of the IEEE*, **60**(9):1107 – 1109, Sep 1972. 6, 8

[21] M. E. Marhic and E. Garmire. **Low-order $TE_{01}$ operation of a $CO_2$ laser for transmission through circular metallic waveguides**. *Applied Physics Letters*, **38**(10):743–745, 1981. 8

[22] Steve C. Tidwell, Dennis H. Ford, and Wayne D. Kimura. **Generating radially polarized beams interferometrically**. *Appl. Opt.*, **29**(15):2234–2239, May 1990.

[23] E.G. Churin, J. Hobfeld, and T. Tschudi. **Polarization configurations with singular point formed by computer generated holograms**. *Optics Communications*, **99**(1a2):13 – 17, 1993.

[24] Steve C. Tidwell, Gerald H. Kim, and Wayne D. Kimura. **Efficient radially polarized laser beam generation with a double interferometer**. *Appl. Opt.*, **32**(27):5222–5229, Sep 1993.

[25] M. Stalder and M. Schadt. **Linearly polarized light with axial symmetry generated by liquid-crystal polarization converters**. *Opt. Lett.*, **21**(23):1948–1950, Dec 1996. 8

[26] Rebecca H. Jordan and Dennis G. Hall. **Free-space azimuthal paraxial wave equation: the azimuthal Bessel-Gauss beam solution**. *Opt. Lett.*, **19**(7):427–429, Apr 1994. 8

[27] Dennis G. Hall. **Vector-beam solutions of Maxwell's wave equation**. *Opt. Lett.*, **21**(1):9–11, Jan 1996. 8

[28] Pamela L. Greene and Dennis G. Hall. **Diffraction characteristics of the azimuthal Bessel-Gauss beam**. *J. Opt. Soc. Am. A*, **13**(5):962–966, May 1996. 8

[29] Pamela Greene and Dennis Hall. **Focal shift in vector beams**. *Opt. Express*, **4**(10):411–419, May 1999. 8

[30] Kathleen Youngworth and Thomas Brown. **Focusing of high numerical aperture cylindrical-vector beams**. *Opt. Express*, **7**(2):77–87, Jul 2000. 8, 55, 58, 106

[31] B. Richards and E. Wolf. **Electromagnetic Diffraction in Optical Systems. II. Structure of the Image Field in an Aplanatic System**. *Proceedings of the Royal Society of London. Series A. Mathematical and Physical Sciences*, **253**(1274):358–379, 1959. 8, 51, 55

[32] Ching-Cherng Sun and Chin-Ku Liu. **Ultrasmall focusing spot with a long depth of focus based on polarization and phase modulation**. *Opt. Lett.*, **28**(2):99–101, Jan 2003. 8

[33] Haifeng Wang, Luping Shi, Boris Lukyanchuk, Colin Sheppard, and Chong Tow Chong. **Creation of a needle of longitudinally polarized light in vacuum using binary optics**. *Nat. Photon.*, **2**(8):501–505, Aug 2008. 59, 60

[34] Xiang Hao, Cuifang Kuang, Tingting Wang, and Xu Liu. **Phase encoding for sharper focus of the azimuthally polarized beam**. *Opt. Lett.*, **35**(23):3928–3930, Dec 2010. 8

[35] Cyril Hnatovsky, Vladlen Shvedov, Wieslaw Krolikowski, and Andrei Rode. **Revealing Local Field Structure of Focused Ultrashort Pulses**. *Phys. Rev. Lett.*, **106**:123901, Mar 2011. 8, 59

[36] L. Novotny, M. R. Beversluis, K. S. Youngworth, and T. G. Brown. **Longitudinal Field Modes Probed by Single Molecules**. *Phys. Rev. Lett.*, **86**:5251–5254, Jun 2001.

[37] A. Bouhelier, M. Beversluis, A. Hartschuh, and L. Novotny. **Near-Field Second-Harmonic Generation Induced by Local Field Enhancement**. *Phys. Rev. Lett.*, **90**:013903, Jan 2003.

[38] Alessandro Ciattoni, Bruno Crosignani, Paolo Di Porto, and Amnon Yariv. **Azimuthally Polarized Spatial Dark Solitons: Exact Solutions of Maxwell's Equations in a Kerr Medium**. *Phys. Rev. Lett.*, **94**:073902, Feb 2005.

[39] Qiwen Zhan. **Trapping metallic Rayleigh particles with radial polarization**. *Opt. Express*, **12**(15):3377–3382, Jul 2004.

[40] C. Gabriel, A. Aiello, W. Zhong, T. G. Euser, N. Y. Joly, P. Banzer, M. Förtsch, D. Elser, U. L. Andersen, Ch. Marquardt, P. St. J. Russell, and G. Leuchs. **Entangling Different Degrees of Freedom by Quadrature Squeezing Cylindrically Polarized Modes**. *Phys. Rev. Lett.*, **106**:060502, Feb 2011. 8

[41] S. Winnerl, B. Zimmermann, F. Peter, H. Schneider, and M. Helm. **Terahertz Bessel-Gauss beams of radial and azimuthal polarization from microstructured photoconductive antennas**. *Opt. Express*, **17**(3):1571–1576, Feb 2009. 9, 70, 79

[42] Jason A. Deibel, Kanglin Wang, Matthew D. Escarra, and Daniel Mittleman. **Enhanced coupling of terahertz radiation to cylindrical wire waveguides**. *Opt. Express*, **14**(1):279–290, Jan 2006. 96, 98, 106

[43] Tae-In Jeon, Jiangquan Zhang, and D. Grischkowsky. **THz Sommerfeld wave propagation on a single metal wire**. *Applied Physics Letters*, **86**(16):161904, 2005. 96, 101, 111

[44] Stephan Winnerl. **Scalable Microstructured Photoconductive Terahertz Emitters**. *Journal of Infrared, Millimeter, and Terahertz Waves*, **33**:431–454, 2012. 9, 14, 70, 79

[45] T. Grosjean, F. Baida, R. Adam, J.-P. Guillet, L. Billot, P. Nouvel, J. Torres, A. Penarier, D. Charraut, and L. Chusseau. **Linear to radial polarization conversion in the THz domain using a passivesystem**. *Opt. Express*, **16**(23):18895–18909, Nov 2008. 9, 68, 69, 96

[46] C. D'Amico, A. Houard, M. Franco, B. Prade, A. Mysyrowicz, A. Couairon, and V. T. Tikhonchuk. **Conical Forward THz Emission from Femtosecond-Laser-Beam Filamentation in Air**. *Phys. Rev. Lett.*, **98**:235002, Jun 2007. 9, 66, 67, 79

[47] Y. Zhang, Y. Chen, C. Marceau, W. Liu, Z.-D. Sun, S. Xu, F. Théberge, M. Châteauneuf, J. Dubois, and S. L. Chin. **Non-radially polarized THz pulse emitted from femtosecond laser filament in air**. *Opt. Express*, **16**(20):15483–15488, Sep 2008. 9, 67

[48] Yanping Chen, Claude Marceau, Weiwei Liu, Zhen-Dong Sun, Yizhu Zhang, Francis Theberge, Marc Chateauneuf, Jacques Dubois, and See Leang Chin. **Elliptically polarized terahertz emission in the forward direction of a femtosecond laser filament in air**. *Applied Physics Letters*, **93**(23):231116, 2008. 9, 67

[49] Guoqing Chang, Charles J. Divin, Chi-Hung Liu, Steven L. Williamson, Almantas Galvanauskas, and Theodore B. Norris. **Generation of radially polarized terahertz pulses via velocity-mismatched optical rectification**. *Opt. Lett.*, **32**(4):433–435, Feb 2007. 9, 66, 67, 79

[50] Wenqi Zhu, Amit Agrawal, Hua Cao, and Ajay Nahata. **Generation of broadband radially polarized terahertz radiation directly on a cylindrical metal wire**. *Opt. Express*, **16**(12):8433–8439, Jun 2008. 9, 79, 96

[51] Kanglin Wang and Daniel M. Mittleman. **Metal wires for terahertz wave guiding**. *Nature*, **432**(8):376–379, Dec 2004. 10, 65, 95, 96, 97, 101, 109, 111

[52] Bradley Bowden, James A. Harrington, and Oleg Mitrofanov. **Low-loss modes in hollow metallic terahertz waveguides with dielectric coatings**. *Applied Physics Letters*, **93**(18):181104, 2008. 10

[53] Ryo Imai, Natsuki Kanda, Takuya Higuchi, Zhu Zheng, Kuniaki Konishi, and Makoto Kuwata-Gonokami. **Terahertz vector beam generation using segmented nonlinear optical crystals with threefold rotational symmetry**. *Opt. Express*, **20**(20):21896–21904, Sep 2012. 10, 43, 74, 86

[54] D. H. Auston. **Picosecond optoelectronic switching and gating in silicon**. *Applied Physics Letters*, **26**(3):101–103, 1975. 11

[55] D. C. Look, D. C. Walters, G. D. Robinson, J. R. Sizelove, M. G. Mier, and C. E. Stutz. **Annealing dynamics of molecular-beam epitaxial GaAs grown at 200 °C**. *Journal of Applied Physics*, **74**(1):306–310, 1993. 13

[56] F. E. Doany, D. Grischkowsky, and C.-C. Chi. **Carrier lifetime versus ion-implantation dose in silicon on sapphire**. *Applied Physics Letters*, **50**(8):460–462, 1987.

[57] K. A. McIntosh, K. B. Nichols, S. Verghese, and E. R. Brown. **Investigation of ultrashort photocarrier relaxation times in low-temperature-grown GaAs**. *Applied Physics Letters*, **70**(3):354–356, 1997.

[58] S. Gupta, M. Y. Frankel, J. A. Valdmanis, J. F. Whitaker, G. A. Mourou, F. W. Smith, and A. R. Calawa. **Subpicosecond carrier lifetime in GaAs grown by molecular beam epitaxy at low temperatures**. *Applied Physics Letters*, **59**(25):3276–3278, 1991. 13

[59] S. Verghese, K.A. McIntosh, and E.R. Brown. **Highly tunable fiber-coupled photomixers with coherent terahertz output power**. *Microwave Theory and Techniques, IEEE Transactions on*, **45**(8):1301–1309, Aug 1997. 13

[60] L. Duvillaret, F. Garet, J-F Roux, and J.-L. Coutaz. **Analytical modeling and optimization of terahertz time-domain spectroscopy experiments, using photoswitches as antennas**. *Selected Topics in Quantum Electronics, IEEE Journal of*, **7**(4):615–623, Jul/Aug. 15

[61] P. Uhd Jepsen, R. H. Jacobsen, and S. R. Keiding. **Generation and detection of terahertz pulses from biased semiconductor antennas**. *J. Opt. Soc. Am. B*, **13**(11):2424–2436, Nov 1996. 15

[62] Masahiko Tani, Shuji Matsuura, Kiyomi Sakai, and Shin ichi Nakashima. **Emission characteristics of photoconductive antennas based on low-temperature-grown GaAs and semi-insulating GaAs**. *Appl. Opt.*, **36**(30):7853–7859, Oct 1997. 16

[63] Sang-Gyu Park, M. R. Melloch, and A. M. Weiner. **Comparison of terahertz waveforms measured by electro-optic and photoconductive sampling**. *Applied Physics Letters*, **73**(22):3184–3186, 1998. 17

[64] Qi Wu and Xi-Cheng Zhang. **Design and characterization of traveling-wave electrooptic terahertz sensors**. *Selected Topics in Quantum Electronics, IEEE Journal of*, **2**(3):693–700, Sep. 19

[65] F. Blanchard, Gargi Sharma, L. Razzari, X. Ropagnol, H-C Bandulet, F. Vidal, Roberto Morandotti, J. Kieffer, Tsuneyuki Ozaki, H. Tiedje, H. Haugen, M. Reid, and F. Hegmann. **Generation of Intense Terahertz Radiation via Optical Methods**. *Selected Topics in Quantum Electronics, IEEE Journal of*, **17**(1):5–16, 2011. 19, 22

[66] Ajay Nahata. **Nonlinear optical generation and detection of ultrashort electrical pulses in transmission lines**. *Opt. Lett.*, **26**(6):385–387, Mar 2001. 19

[67] A. Bonvalet, M. Joffre, J. L. Martin, and A. Migus. **Generation of ultrabroadband femtosecond pulses in the mid-infrared by optical rectification of 15 fs light pulses at 100 MHz repetition rate**. *Applied Physics Letters*, **67**(20):2907–2909, 1995. 19

[68] A. Rice, Y. Jin, X. F. Ma, X.-C. Zhang, D. Bliss, J. Larkin, and M. Alexander. **Terahertz optical rectification from** < 110 > **zinc-blende crystals**. *Applied Physics Letters*, **64**(11):1324–1326, 1994. 19

[69] C. Winnewisser, P. Uhd Jepsen, M. Schall, V. Schyja, and H. Helm. **Electro-optic detection of THz radiation in** $LiTaO_3$**,** $LiNbO_3$ **and ZnTe**. *Applied Physics Letters*, **70**(23):3069–3071, 1997. 20

[70] P. Y. Han and X.-C. Zhang. **Coherent, broadband midinfrared terahertz beam sensors**. *Applied Physics Letters*, **73**(21):3049–3051, 1998. 20

[71] *User's Nanual Verdi(Coherent Inc.)*. 32

[72] *Operator's manual The Coherent Mira model 900 laser/RegA model 9000 laser(Coherent Inc.)*. 32

[73] *User's Manual Hurricane (Spectra Physics Inc.)*. 32

[74] *User's Manual Legend Elite (Coherent Inc.)*. 33

[75] Natsuki Kanda. *Doctoral Thesis*. Jun. 2012. 34

[76] *Manual PCA-40-05-10-800*. 34, 35, 36, 37, 38

[77] Martin Van Exter and D. Grischkowsky. **Characterization of an optoelectronic terahertz beam system**. *Microwave Theory and Techniques, IEEE Transactions on*, **38**(11):1684–1691, 1990. 38

[78] Zhu Zheng, Natsuki Kanda, Kuniaki Konishi, and Makoto Kuwata-Gonokami. **Efficient coupling of propagating broadband terahertz radial beams to metal wires**. *Opt. Express*, **21**(9):10642–10650, May 2013. 44, 77, 100, 101, 102, 103, 106, 110

[79] Ryo Imai. *Master Thesis*. Jun. 2012. 44, 80

[80] Dennis G. Hall. **Vector-beam solutions of Maxwell's wave equation**. *Opt. Lett.*, **21**(1):9–11, Jan 1996. 47

[81] John David Jackson. *Classical Electrodynamics*. Aug. 1998. 47

[82] Les Allen, MW Beijersbergen, RJC Spreeuw, JP Woerdman, et al. **Orbital angular momentum of light and the transformation of Laguerre-Gaussian laser modes**. *Physical Review A*, **45**(11):8185–8189, 1992. 48

[83] F. Gori, G. Guattari, and C. Padovani. **Bessel-Gauss beams**. *Optics Communications*, **64**(6):491 – 495, 1987. 49

[84] Marcel Leutenegger, Ramachandra Rao, Rainer A. Leitgeb, and Theo Lasser. **Fast focus field calculations**. *Opt. Express*, **14**(23):11277–11291, Nov 2006. 51, 52

[85] Max Born and Emil Wolf. *Principles of Optics*. 2001. 53

[86] Baohua Jia, Xiaosong Gan, and Min Gu. **Direct measurement of a radially polarized focused evanescent field facilitated by a single LCD**. *Opt. Express*, **13**(18):6821–6827, Sep 2005. 58, 59

[87] Xiangping Li, Tzu-Hsiang Lan, Chung-Hao Tien, and Min Gu. **Three-dimensional orientation-unlimited polarization encryption by a single optically configured vectorial beam**. *Nat. Photon.*, **3**(998), Aug 2012. 59, 60

[88] Yiqiong Zhao, Qiwen Zhan, Yanli Zhang, and Yong-Ping Li. **Creation of a three-dimensional optical chain for controllable particle delivery**. *Opt. Lett.*, **30**(8):848–850, Apr 2005. 59

[89] Nándor Bokor and Nir Davidson. **Generation of a hollow dark spherical spot by 4pi focusing of a radially polarized Laguerre-Gaussian beam**. *Opt. Lett.*, **31**(2):149–151, Jan 2006. 59

[90] Weibin Chen and Qiwen Zhan. **Three-dimensional focus shaping with cylindrical vector beams**. *Optics Communications*, **265**(2):411 – 417, 2006. 59

[91] Ayman F. Abouraddy and Kimani C. Toussaint. **Three-Dimensional Polarization Control in Microscopy**. *Phys. Rev. Lett.*, **96**:153901, Apr 2006.

[92] Jiming Wang, Weibin Chen, and Qiwen Zhan. **Engineering of high purity ultra-long optical needle field through reversing the electric dipole array radiation**. *Opt. Express*, **18**(21):21965–21972, Oct 2010. 59

[93] Xi-Lin Wang, Jing Chen, Yongnan Li, Jianping Ding, Cheng-Shan Guo, and Hui-Tian Wang. **Optical orbital angular momentum from the curl of polarization**. *Phys. Rev. Lett.*, **105**:253602, Dec 2010. 59

[94] P. Török and P. Munro. **The use of Gauss-Laguerre vector beams in STED microscopy**. *Opt. Express*, **12**(15):3605–3617, Jul 2004. 59

[95] Weibin Chen and Qiwen Zhan. **Numerical study of an apertureless near field scanning optical microscope probe under radial polarization illumination**. *Opt. Express*, **15**(7):4106–4111, Apr 2007. 59

[96] Weibin Chen and Qiwen Zhan. **Realization of an evanescent Bessel beam via surface plasmon interference excited by a radially polarized beam**. *Opt. Lett.*, **34**(6):722–724, Mar 2009.

[97] Weibin Chen, Don C. Abeysinghe, Robert L. Nelson, and Qiwen Zhan. **Plasmonic Lens Made of Multiple Concentric Metallic Rings under Radially Polarized Illumination**. *Nano Letters*, **9**(12):4320–4325, 2009. PMID: 19877687. 59

[98] Yuichi Kozawa and Shunichi Sato. **Generation of a radially polarized laser beam by use of a conical Brewster prism**. *Opt. Lett.*, **30**(22):3063–3065, Nov 2005. 61, 62

[99] G. Machavariani, Y. Lumer, I. Moshe, A. Meir, and S. Jackel. **Spatially-variable retardation plate for efficient generation of radially- and azimuthally-polarized beams**. *Optics Communications*, **281**(4):732 – 738, 2008. 62, 63

[100] Ze'ev Bomzon, Gabriel Biener, Vladimir Kleiner, and Erez Hasman. **Radially and azimuthally polarized beams generated by space-variant dielectric subwavelength gratings**. *Opt. Lett.*, **27**(5):285–287, Mar 2002. 63, 64

[101] Xi-Lin Wang, Jianping Ding, Wei-Jiang Ni, Cheng-Shan Guo, and Hui-Tian Wang. **Generation of arbitrary vector beams with a spatial light modulator and a common path interferometric arrangement**. *Opt. Lett.*, **32**(24):3549–3551, Dec 2007. 63, 64

[102] Oleg Mitrofanov and James A. Harrington. **Dielectric-lined cylindrical metallic THz waveguides: mode structure and dispersion**. *Opt. Express*, **18**(3):1898–1903, Feb 2010. 65

[103] Raimund Mueckstein, Chris Graham, CyrilC. Renaud, AlwynJ. Seeds, JamesA. Harrington, and Oleg Mitrofanov. **Imaging and Analysis of THz Surface Plasmon Polariton Waves with the Integrated Sub-wavelength Aperture Probe**. *Journal of Infrared, Millimeter, and Terahertz Waves*, **32**(8-9):1031–1042, 2011. 65

[104] Raimund Mueckstein and Oleg Mitrofanov. **Imaging of terahertz surface plasmon waves excited on a gold surface by a focused beam**. *Opt. Express*, **19**(4):3212–3217, Feb 2011. 65

[105] Stefan A. Maier, Steve R. Andrews, L. Martín-Moreno, and F. J. García-Vidal. **Terahertz Surface Plasmon-Polariton Propagation and Focusing on Periodically Corrugated Metal Wires**. *Phys. Rev. Lett.*, **97**:176805, Oct 2006. 65, 111, 112

[106] Young Bin Ji, Eui Su Lee, Jin Seok Jang, and Tae In Jeon. **Enhancement of the detection of THz Sommerfeld wave using a conical wire waveguide**. *Opt. Express*, **16**(1):271–278, Jan 2008. 65

[107] Hao Chen, Qiwen Zhan, Yanli Zhang, and Yong-Ping Li. **The Gouy phase shift of the highly focused radially polarized beam**. *Physics Letters A*, **371**(3):259 – 261, 2007. 65

[108] Takuya Higuchi, Natsuki Kanda, Hiroharu Tamaru, and Makoto Kuwata-Gonokami. **Selection Rules for Light-Induced Magnetization of a Crystal with Threefold Symmetry: The Case of Antiferromagnetic NiO**. *Phys. Rev. Lett.*, **106**:047401, Jan 2011. 71

[109] Q. Chen, M. Tani, Zhiping Jiang, and X.-C. Zhang. **Electro-optic transceivers for terahertz-wave applications**. *J. Opt. Soc. Am. B*, **18**(6):823–831, Jun 2001. 71, 74, 86

[110] G. Machavariani, Y. Lumer, I. Moshe, A. Meir, and S. Jackel. **Efficient extracavity generation of radially and azimuthally polarized beams**. *Opt. Lett.*, **32**(11):1468–1470, Jun 2007. 79

[111] N. Nemoto, N. Kanda, K. Konishi, S. Kurashina, T. Sasaki, N. Oda, and M. Kuwata-Gonokami. **Development and evaluation of high-sensitivity terahertz camera**. In *CLEO 2013*, 2013. 80

[112] L. D. Landau and E. M. Lifshitz. *Electrodynamics of Continuous Media*. Oxford, Pergamon, 1960. 89

[113] R. Mendis and D. Grischkowsky. **Plastic ribbon THz waveguides**. *Journal of Applied Physics*, **88**(7):4449–4451, 2000. 96

[114] Li-Jin Chen, Hung-Wen Chen, Tzeng-Fu Kao, Ja-Yu Lu, and Chi-Kuang Sun. **Low-loss subwavelength plastic fiber for terahertz waveguiding**. *Opt. Lett.*, **31**(3):308–310, Feb 2006. 96

[115] Daru Chen and Haibin Chen. **A novel low-loss Terahertz waveguide: Polymer tube**. *Opt. Express*, **18**(4):3762–3767, Feb 2010. 96

[116] D. Grischkowsky. **Optoelectronic characterization of transmission lines and waveguides by terahertz time-domain spectroscopy**. *Selected Topics in Quantum Electronics, IEEE Journal of*, **6**(6):1122–1135, 2000. 96

[117] Markus Wachter, Michael Nagel, and Heinrich Kurz. **Low-loss terahertz transmission through curved metallic slit waveguides fabricated by spark erosion**. *Applied Physics Letters*, **92**(16):161102, 2008. 96

[118] Sang-Hoon Kim, Eui Su Lee, Young Bin Ji, and Tae-In Jeon. **Improvement of THz coupling using a tapered parallel-plate waveguide**. *Opt. Express*, **18**(2):1289–1295, Jan 2010. 96

[119] G. Gallot, S. P. Jamison, R. W. McGowan, and D. Grischkowsky. **Terahertz waveguides**. *J. Opt. Soc. Am. B*, **17**(5):851–863, May 2000. 96

[120] R. Mendis and D. Grischkowsky. **Undistorted guided-wave propagation of subpicosecond terahertz pulses**. *Opt. Lett.*, **26**(11):846–848, Jun 2001. 96

[121] Georg Goubau. **Surface Waves and Their Application to Transmission Lines**. *Journal of Applied Physics*, **21**(11):1119–1128, 1950. 96

[122] Kanglin Wang and Daniel M. Mittleman. **Guided propagation of terahertz pulses on metal wires**. *J. Opt. Soc. Am. B*, **22**(9):2001–2008, Sep 2005. 96, 101, 105, 106, 107, 108, 109, 111, 112

[123] Laurent Chusseau and Jean-Paul Guillet. **Coupling and Propagation of Sommerfeld Waves at 100and 300GHz**. *Journal of Infrared, Millimeter, and Terahertz Waves*, **33**(2):174–182, 2012. 96, 101, 111

[124] Hua Cao and Ajay Nahata. **Coupling of terahertz pulses onto a single metal wire waveguide using milled grooves**. *Opt. Express*, **13**(18):7028–7034, Sep 2005. 96

[125] Amit Agrawal and Ajay Nahata. **Coupling terahertz radiation onto a metal wire using a subwavelength coaxial aperture**. *Opt. Express*, **15**(14):9022–9028, Jul 2007. 96

[126] Kanglin Wang and Daniel M. Mittleman. **Dispersion of Surface Plasmon Polaritons on Metal Wires in the Terahertz Frequency Range**. *Phys. Rev. Lett.*, **96**:157401, Apr 2006. 101, 111

[127] S Quabis, R Dorn, M Eberler, O Glckl, and G Leuchs. **Focusing light to a tighter spot**. *Optics Communications*, **179**(16):1 – 7, 2000. 106

[128] Qing Cao and Jürgen Jahns. **Azimuthally polarized surface plasmons as effective terahertz waveguides**. *Opt. Express*, **13**(2):511–518, Jan 2005. 107

[129] M. Fadhali, Saktioto, J. Zainal, Y. Munajat, J. Ali, and R. Abdul Rahman. **Mode matching for efficient laser diode to single mode fiber coupling**. pages 67930G–67930G–8, 2008. 109

[130] Somenath Sarkar, K. Thyagarajan, and Arun Kumar. **Gaussian approximation of the fundamental mode in single mode elliptic core fibers**. *Optics Communications*, **49**(3):178 – 183, 1984. 109

[131] David Crawley, Christopher Longbottom, Vincent P. Wallace, Bryan Cole, Don Arnone, and Michael Pepper. **Three-dimensional terahertz pulse imaging of dental tissue**. *Journal of Biomedical Optics*, **8**(2):303–307, 2003. 110

[132] R.M. Woodward, V.P. Wallace, D.D. Arnone, E.H. Linfield, and M. Pepper. **Terahertz Pulsed Imaging of Skin Cancer in the Time and Frequency Domain**. *Journal of Biological Physics*, **29**(2-3):257–259, 2003. 110

[133] S Wang and X-C Zhang. **Pulsed terahertz tomography**. *Journal of Physics D: Applied Physics*, **37**(4):R1, 2004. 110

[134] A.I. Fernandez-Dominguez, L. Martin-Moreno, F.J. Garcia-Vidal, S.R. Andrews, and S.A. Maier. **Spoof Surface Plasmon Polariton Modes Propagating Along Periodically Corrugated Wires**. *Selected Topics in Quantum Electronics, IEEE Journal of*, **14**(6):1515–1521, 2008. 111

[135] A. I. Fernandez-Dominguez, C. R. Williams, F. J. Garcia-Vidal, L. Martin-Moreno, S. R. Andrews, and S. A. Maier. **Terahertz surface plasmon polaritons on a helically grooved wire**. *Applied Physics Letters*, **93**(14):141109, 2008. 111